MICRO- AND NANO-MECHANICS OF NATURAL AND BIOINSPIRED MATERIALS

JIMIN FU

PhD

The Hong Kong Polytechnic University

2019

The Hong Kong Polytechnic University

Department of Mechanical Engineering

Micro- and Nano-mechanics of Natural and Bioinspired Materials

Jimin FU

A thesis submitted in partial fulfilment of the requirements for the degree of

Doctor of Philosophy

December 2018

CERTIFICATE OF ORIGINALITY

I hereby declare that this thesis is my own work and that, to the best of my knowledge and belief, it reproduces no material previously published or written, nor material that has been accepted for the award of any other degree or diploma, except where due acknowledgement has been made in the text.

_____(Singed)

Jimin FU_____(Name of student)

Lovingly dedicated to my parents and family who always support me.

Abstract

As a stealth hand, ecological systems have shaped all lives in the earth to achieve extreme performance in adapting to the severe environment. How nature can build a variety of materials with such novel structures and unique functions, and what are the relationships between these structures and functions? Experimental characterization and theoretical modeling expose that the unique properties of these natural materials rely on the complex structures ranging from macro- to nano-scales. In addition to the efforts devoted to understanding the mechanisms behind these fancy structures and functions, a growing effort were devoted to developing and fabricating materials with the novel properties by mimicking those found in nature. These bioinspired materials commonly include organic and inorganic components that need perfect assembly from macro- to nano-scales. In the thesis, the attentions are focused on abundant mechanical phenomena existing in biological and bioinspired systems, especially, tribological (wear, adhesion and contact) behaviors and fracture behaviors under impact loading. The objectives are to explicate the mechanisms behind the abundant mechanical phenomena. Although the investigations are found in the specific biological and bioinspired systems, the mechanical principles to be revealed can be broadly used as the guidelines of related engineering applications.

Chapter 1 is about the fundamental knowledge concerning the mechanical phenomena in natural and bioinspired materials, and then a literature review on the related field in recent years to reveal and apply some mechanical, especially, tribological mechanisms and fracture-modes-controlled mechanisms in biological systems is presented in Chapter 2. In Chapter 3, the experimental methods including characterization and synthesis methods adopted in the studies are discussed, followed by brief introduction of molecular dynamic (MD) simulation method.

Subsequently, prominent wear resistance of the teeth of black carp is studied in Chapter 4. In this chapter, the mechanism of the high wear resistance of the black carp teeth occlusal surface (OS) is found. Nano-scratching test and comparative X-ray diffraction analysis on the enameloid, the outermost layer of the teeth, indicate that hydroxyapatite (HAp) crystallites show *c*-axis preferential orientation in the vicinity of OS. The prominent wear resistance of the teeth is attributed to the *c*-axis preferential orientation of HAp near the OS since the (001) surface of HAp crystal, which is perpendicular to the *c*-axis, exhibits much better wear resistance compared to the other surfaces as demonstrated by the MD simulation. The following theoretical modeling indicates that scratching on the (001) surface of HAp tends to cause ‘rubbing mode’ failure rather than ‘cutting mode’ failure. The finding shows great promise of utilizing preferential orientation of crystals to increase the wear resistance of materials.

In Chapter 5, the excellent anti-fouling performance of the *Sonneratia apetala* leaves is demonstrated to be attributed to their ridge-like surface morphology. Inspired by the superior antifouling performance of the leaves of mangrove tree *S. apetala*, to combat biofouling by using surface with ridge-like morphology is proposed. Settlement tests with tubeworm larvae on polymeric replicas of *S. apetala* leaves confirm that the ridge-like surface morphology can effectively prevent biofouling. A contact mechanics-based model is then established to quantify the dependence of tubeworm settlement on the structural features of the ridge-like morphology, giving rise to theoretical guidelines to optimize the morphology for better antifouling performance. By following the obtained guidelines, a synthetic surface with ridge-like morphology is developed, exhibiting antifouling performance comparable to that of the *S. apetala* replica. The following theoretical modeling indicates that shape ridge can reduce the fouler attachment probability and then show good anti-fouling performance.

In Chapter 6, inspired by toughening mechanisms adopted by various natural materials such as nacre, bones, and teeth, consisting of brittle mineral platelets embedded in a soft, ductile organic matrix, the fracture behavior of bio-inspired graphene-based structure under hypervelocity impact is studied through MD simulation. By optimizing the geometrical structures of the inclusions in the graphene membrane, the controlled fracture behavior can be achieved. Results show that the inclusions embedded in the graphene-based material can change crack path. Based on the simulation results,

several means are proposed to improve anti-crack performance by using the shielding effect of the inclusions in the graphene-based material: (1) choosing a harder inclusion, (2) increasing the radius of inclusion, R_I.

Through the comprehensive studies on the novel mechanical properties of the typical natural materials, the relationships between their structures and functions are analyzed. The theoretical guidelines should be beneficial for the development of the corresponding bioinspired materials. In summary, the investigations present in this thesis not only decode the mechanical mechanisms accounting for the fancy mechanical properties of these natural material but also provide practical strategies and guidelines for the design of bioinspired materials and structures with better performance.

Publications

1. **Jimin Fu**, Chong He, Biao Xia, Yan Li, Qiong Feng, Qifang Yin, Xinghua Shi, Xue Feng, Hongtao Wang and Haimin Yao, 2016, *c*-axis preferential orientation of hydroxyapatite accounts for the high wear resistance of the teeth of black carp (*Mylopharyngodon piceus*), *Scientific Report* 6, 23509.

2. **Jimin Fu**, Hua Zhang, Zhenbin Guo, Dan-Qing Feng, Vengatesen Thiyagarajan, Haimin Yao, Combat biofouling with microscopic ridge-like surface morphology: a bioinspired study, *Journal of The Royal Society Interface* 15, 20170823.

Conference presentations

1. **Jimin Fu**, Chong He and Haimin Yao. *c*-axis preferential orientation of hydroxyapatite accounts for the high wear resistance of the black carp (*Mylopharyngodon piceus*) teeth, 19th HKSTAM Annual Conference 2015.

2. **Jimin Fu**, Chong He and Haimin Yao. *c*-axis preferential orientation of hydroxyapatite accounts for the high wear resistance of the black carp (*Mylopharyngodon piceus*) teeth, ICMAT2015 & IUMRS-ICA2015.

3. **Jimin Fu**, Zhenbin Guo and Haimin Yao. Microscopic ridge-like surface morphology: An anti-fouling strategy learn from nature, 22nd HKSTAM Annual Conference 2018.

Acknowledgments

The five-year doctoral experience is fleeting, but the memories of the research, the struggle and the people in the five years are eternal.

Firstly, I would like to express my heartfelt appreciation to my chief supervisor, Prof. Haimin Yao, for his endless encouragement and precious advice during my doctoral period. Prof. Yao's shining creativity in scientific research inspired me, and his assiduous attitude towards science encouraged me. Whenever I got lost in the research, he could always direct me to the right path. His methodology about study and scientific research will be beneficial to my future life, even beyond the field of scientific research.

Secondly, I would like to express my sincere appreciation to Prof. San-Qiang Shi, my co-supervisor. He is a genial and patient supervisor. As one of the most excellent scientists in his field, he has given me a lot of insightful suggestions and guidance, which help me tackle the difficulties in the research process more easily.

I also convey my gratitude to all the previous and current members of our group, Dr. Chong He, Dr. Weiqun Li, Dr. Qifang Yin, Dr. Long Li, Dr. Ji Lin, Mr. Hua Zhang, Mr. Yan Zhou, Mr. Zhaoqiang Song, Ms. Yanwei Xue, Mr. Zhenbin Guo, Mr. Juntan Yang, Ms. Yang Gao and Mr. André Eccel Vellwock. I enjoy your kind company.

It was an unforgettable experience to explore the mysterious world with the preeminent collaborators. I will not be able to successfully complete my work without the help from these collaborators: Prof. Rajan, Dr. Yuan Meng, Dr. Chaoyi Li and Dr. Camilla Campanati from HKU, Prof. Danqing Feng from XMU, Prof. Hongtao Wang and Dr. Qiong Feng from ZJU, Prof. Xue Feng, Dr. Biao Xia and Mr Yan Li from THU, Prof. Xinghua Shi from CAS. I appreciate every brainstorm and every help and enlightenment from them.

My appreciation goes to the technical staff, such as Dr. Curtis Ng, Mr. Benny Leung and Mr. Ka-on YUEN, and the administrative staff such as Ms. Lily Tam, Ms. Celia Wong, Ms. Joanne Cheng and Mrs. Michelle Lai. I would also express my appreciation to the colleagues in the Department of Mechanical Engineering who helped me throughout the whole research period.

I acknowledge the financial support from the Research Grants Council of the Hong Kong Special Administration Region and the Hong Kong Polytechnic University.

Last but not the least, I would like to give my sincere gratitude to my beloved family members, especially my parents. It is their love, support and understanding that soothed me, pushed me forward and let me overcome all these difficulties during my five-year doctoral period.

Table of contents

Abstract ..... **I**

Publications ..... **V**

Conference presentations ..... **VI**

Acknowledgments ..... **VII**

Table of contents ..... **IX**

List of Figures ..... **XIII**

List of Tables ..... **XXIII**

Chapter 1. Introduction **1**

1.1 Basics of natural and bioinspired materials 2

1.2 Mechanics in natural and bioinspired systems 6

1.3 Objectives and outline of this thesis 9

Chapter 2. Research background and literature review **11**

2.1 Anti-wear natural and bioinspired materials 11

2.1.1 Anti-wear performance of natural materials 12

2.1.2 Anti-wear mechanism of the natural materials 14

2.1.3 Bioinspired materials with anti-wear performance 17

2.2 Anti-fouling natural and bioinspired materials 20

2.2.1 Anti-fouling performance of natural materials 20

2.2.2 Bioinspired materials with anti-fouling performance 24

2.3 Fracture modes controlled natural and bioinspired materials 28

2.3.1 Anti-crack performance of natural materials 29

2.3.2 Anti-crack mechanism of the natural materials..... 34

2.3.3 Bioinspired materials with controlled fracture..... 36

Chapter 3. Research methods.....40

3.1 Experimental methods..... 40

3.1.1 Wear resistance evaluation 40

3.1.2 Materials characterization 41

3.1.3 Materials synthesis and samples preparation 43

3.1.4 Anti-fouling performance evaluation 45

3.2 Computational methods..... 47

3.2.1 Mathematical manipulations of molecular dynamics simulations 47

3.2.2 Software for molecular dynamics simulations 49

3.2.3 Atomic molecular dynamics simulations 50

3.2.4 Coarse-grained molecular dynamics simulations..... 52

Chapter 4. High wear resistance of the teeth of black carp 54

4.1 The superior wear resistance of the occlusal surface of the teeth 55

4.2 *c*-axis preferential orientation of hydroxyapatite near the occlusal surface 60

4.3 The wear resistance of the single crystal hydroxyapatite..... 62

4.4 The mechanism of the superior wear resistance of the teeth occlusal surface 65

4.5 Summary 73

Chapter 5. Superior anti-fouling performance of the morphology of mangrove leaves 75

5.1 Superior anti-fouling performance of *Sonneratia apetala* leaves 77

5.2 Theoretical modeling of anti-fouling mechanism 80

5.3 Bioinspired synthetic anti-fouling surface 92

5.4 Summary 93

Chapter 6. Bioinspired graphene-based structures with controlled fracture 95

6.1 Mode-I fracture in graphene-based material with inclusion 96

6.2 Dynamical impact fracture in graphene 100

6.3 Dynamical impact fracture in graphene with inclusions..... 102

6.4 Summary 105

Chapter 7. Conclusions and future work 106

7.1 Conclusions 106

7.2 Outlook to the future research 108

7.2.1 Wear behavior and dynamical impact fracture in multi-layer graphene-

based structures 109

7.2.2 Design anti-fouling coating for the application in the field 110

References 111

List of Figures

Figure 1.1. Hierarchical structure of Abalone nacre (adapted from [19]). 4

Figure 1.2. Tension-shear chain model of the natural composites (adapted from [30]). 5

Figure 1.3. The structure of a gecko foot from macro- to nanoscale. (a) Gecko; (b) seta array; (c) single seta; (d) spatulae on tip of seta (adapted from [20]). 7

Figure 1.4. From snakeskin to snake-inspired micro-structured polymer surfaces (SIMPS). (a) Photograph of *Lampropeltis californiae*; (b) SEM image of *L. californiae* snake skin; (c) SEM image of SIMPS. 3D image of (d) *L. californiae* snake skin and (e) SIMPS based on AFM data (adapted from [33]). 7

Figure 2.1. Typical examples of biological materials with high wear tolerance. Three typical types (a) protective structures (conch shell), (b) supporting skeleton (*Sponge spicule*) and (c) predation bio-tool (*Chiton radula*) (adapted from [36]). 14

Figure 2.2. Schematic of tooth strucuture, illustrating enamel, dentin, and dentin-enamel-junction (adapted from [38]). 15

Figure 2.3. Images of hierarchical structure of a tooth from nano- to micro-scale

(adapted from [39]). 17

Figure 2.4. SEM image of polymer-infiltrated-ceramic-network structure (adapted from [47]). 18

Figure 2.5. (a) SEM image of rat tooth tip. (b) Schematic of rat tooth-mimicking cutting tool (adapted from [50]). 19

Figure 2.6. SEM image of the riblet structures of the shark skin surface (adapted from [59]). 22

Figure 2.7. SEM images at various magnification scales of (a–c) *M. galloprovincialis*, (d–f) *P. imbricate* (adapted from [62]). 23

Figure 2.8. Hierarchically wrinkled coatings for marine anti-fouling (adapted from [66]). 25

Figure 2.9. (a) Image of the pilot whale. (b-e) SEM images of the skin of the pilot whale (adapted from [69]). 27

Figure 2.10. The hierarchical structure of nacre from macro to nanoscale (adapted from [76]). 31

Figure 2.11. (a) Stress-strain curve of nacre under tensile loading. (b) The schematic of the failure of the hydrated nacre (adapted from [77]). 32

Figure 2.12. Schematic of the hierarchical structure of spider silk. (a) The web. (b) Silk

fiber (c) Filaments (d) β-crystal peptide strands (adapted from [78]).... 33

Figure 2.13. Stress-strain curve of *N. clavipes* spider silk compared to artificial fibers under tensile loading (adapted from[79]).... 34

Figure 2.14. Toughening mechanism of nacre from macro- to nano-scale. (a) Toughening mechanism at the micrometer scale. (b) Intra-platelet toughening mechanism at the tens nanometer scale. (c) Toughening mechanism at molecular scale (adapted from [80]). 35

Figure 2.15. Structure and mechanical properties of nacre-like material. (a) SEM image of the layered structure; (b) SEM image of Al_2O_3 monolayer onto GO-PVA layer; (c) Schematic of nacre-like material, and (d) Comparison of mechanical properties of nacre-like and with those of layered GO/PVA and Al_2O_3/PVA (adapted from [80]).... 37

Figure 2.16. (a) Bioinspired carbon nanotube fiber. (b) Schematics of hydrogen-bond structure in the fiber.(c) Stress-strain curves of DWNT-PVA fibers with 0 and 9 wt% PVA (adapted from[82]).... 39

Figure 3.1. SEM image of scratch grooves on human teeth enamel by nano-scratching (adapted from [85]). 41

Figure 3.2. SEM image of *S. apetala* leaves. 42

Figure 3.3. Schematic of the molding process for preparing PDMS replica of *S. apetala* leaves. 43

Figure 3.4. (a) Adult tubeworms *Hydroides elegans* attached on a plastic plate. (b) Adult tubeworm removed from the calcified tubular shell. (c) Larval tubeworm swimming in the seawater to detect the target surface for attachment. 46

Figure 3.5. Schematics of a unit cell of HAp crystal adopted in the MD simulation. 50

Figure 3.6. Schematic of the graphene-based structure impact simulation. 51

Figure 3.7. Schematics of the CGMD simulation model. 53

Figure 4.1. Image of *pharyngeal* teeth of black carp with inset showing a tooth embedded in epoxy from the longitudinal section (LS). 55

Figure 4.2. AFM images of grooves scratched by 90°conical tip with a radius of 20 μm and the cross-section profiles of the grooves. AFM images of scratches on the (a) OS; (b) LS with scratching direction normal to the OS; (c) LS with scratching direction parallel to the OS. (d) The cross-section profiles of the grooves at the position of dotted lines in (a), (b) and (c). 56

Figure 4.3. Scratch depth of nano-scratching tests on the OS and LS of teeth. OS: Occlusal Surface; LS: Longitudinal Section. 57

Figure 4.4. SEM images of the scratches on (a) OS and (b) LS; (c-d) close-ups of the regions A and B on OS; (e-f) close-ups of the regions C and D on LS.. 59

Figure 4.5. (a-c) Schematics of the configurations of three XRD tests on bulk enameloid sample: (a) $\varphi_{\text{ini}} = 0.5^\circ$, $2\theta_{\text{ini}} = 10^\circ$; (b) $\varphi_{\text{ini}} = 10^\circ$, $2\theta_{\text{ini}} = 20^\circ$; (c) $\varphi_{\text{ini}} = 19.5^\circ$, $2\theta_{\text{ini}} = 20^\circ$. (d) Diffraction patterns of three XRD tests on bulk sample in comparison with that obtained from powder sample..... 60

Figure 4.6. (a) Schematics of the MD simulation model and unit cell of HAp crystal. The nano-scratching simulation is implemented through four steps: (1) the rigid probe engages with the surface by penetrating to depth D_p; (2) the probe holds still for 20 ps for relaxation; (3) the probe is displaced horizontally to scratch the surface by 8 nm with D_p kept constant, and (4) the probe is withdrawn from the surface. (b-c) Snapshots of scratching on (001) and (010) surfaces at the end of step (3) with corresponding attack angle α being 20° and 54.8° respectively. Here only the Ca atoms in HAp are shown for a clearer visualization. (d) Variations of the amount of debris characterized by the number of Ca atoms scratched away from the bulk HAp as a function of attack angle α. 63

Figure 4.7. (a) 3D view of schematics of theoretical model. (b) Cross section of 'rubbing mode' and (c) 'cutting mode'. 65

Figure 4.8. Simple shear simulations. (a) Schematics of the simulations model for shear tests. (b-e) Stress–strain curves of the shear tests. 69

Figure 4.9. Nanoindentation simulations used to predict the mechanical properties of HAp on different orientations. (a) Schematics of the simulations model for indentation tests which are implemented through two consecutive steps: (1) the rigid probe engages with the HAp single crystal with indentation depth h =1.5 nm; (2) the probe is withdrawn from the HAp sample. (b-e) Load-depth curves of the indentation simulation obtained on different surfaces, from which the mechanical properties of the related surface can be deduced. 70

Figure 4.10. Schematics of the simulations model for determination of surface energy. 71

Figure 4.11. Dependence of α_c on H/τ_y for given $\gamma_s/\tau_y D_p$. 72

Figure 5.1. The anti-fouling leaves of *S. apetala* and bio-fouler tubeworm *H. elegans*. (a) *S. apetala* living in intertidal zone. (b) a leaf of *S. apetala*. (c) adult tubeworms *H. elegans* accumulated on a plastic bucket. (d) a larva of *H. elegans* with calcareous shell attached on a glass slide. 76

Figure 5.2. (a) The molding process for preparing PDMS replica of *S. apetala* leaves. (b-d) SEM images of a leaf surface of *S. apetala* morphology compared

to (e-g) those of its replica morphology. 78

Figure 5.3. Anti-fouling performance evaluation. (a) Attachment of tubeworm larvae on glass slide, flat PDMS surface and PDMS replica of a *S. apetala* leaf after 0 h, 24 h and 48 h immersion. (b) Means ±SE (n = 6) of total counts of tubeworms attached on these surfaces after 24 h and 48 h. 79

Figure 5.4. Schematics of three possible attachment configurations of a tubeworm attached on substrate with wavy profile: (a) single-point attachment, (b) double-point attachment and (c) multi-point attachment. 80

Figure 5.5. (a) Schematic of single-point attachment configuration. (b) Variation of the pull-off force with λ/R_T for single-point attachment configuration with various A/λ 82

Figure 5.6. (a) Contact between two solids with profile functions $f_1(x)$ and $f_2(x)$. (b) Contact between a solid with profile function $f_2(x)-f_1(x)$ and a flat substrate. (c) Contact between a solid a solid with flat profile and a flat substrate..... 84

Figure 5.7. (a) Schematic of double-point attachment configuration. (b) Variation of the pull-off force with λ/R_T for double-point attachment configuration with various A/λ 85

Figure 5.8. Schematic of multi-point attachment configuration. 87

Figure 5.9. (a) The calculated dependence of the adhesion force on the displacement of the cylinder. (b) Calculated evolution of the normalized pull-off force with ln (R_T/λ). Here A/λ is taken as 0.5. (c) Comparison of calculated normalized pull-off force as a function λ/R_T with the theoretical prediction given by Eq. (5.18). 89

Figure 5.10. (a) Variation of the normalized pull-off force with λ/R_T for $A/\lambda = 0.5$ for three possible configurations of an elastic cylinder in adhesive contact with a wavy substrate.. (b) Effect of A/λ on pull-off force for $A/\lambda = 0.125$-2..... 91

Figure 5.11. (a) Schematic of the synthesis process of anti-fouling surface. (b) SEM images of a synthetic surface with ridge-like morphology. Scale bar in the figure and inset are 10 and 2 μm respectively (c) Means ±SE (n = 6) of the total counts of tubeworms attached on the synthetic surfaces with ridge-like morphology. 93

Figure 6.1. MD simulation models: Samples of graphene containing a preexisting crack and a circular inclusion. (a) and (b) show the models with armchair and zigzag crack-tips, respectively. The loading direction is indicated as the violet arrows. 98

Figure 6.2. Uniaxial tension stress-strain of graphene-based with inclusion materials

when loaded along zigzag and armchair directions. 99

Figure 6.3. The volumetric strain contour of the zigzag crack-tip cases at strain ε_{xx} of 10% in the presence of one inclusion (a) with $E_I = 0.5E_G$ and (b) $E_I = 2E_G$, respectively. 100

Figure 6.4. Schematic view of the impact simulation on the monolayer graphene. Graphene is fixed in the lateral directions at the edges, colored in red. The projectile impacts on the center of the graphene sample. 101

Figure 6.5. Atomic configurations of the graphene membrane showing the final failure shape induced by the projectile. 101

Figure 6.6. Schematic view of the impact simulation on the monolayer graphene-based material. A graphene-based material is fixed in the lateral directions at the corners, colored in red. The projectile is placed in the center of the graphene-based sample. 102

Figure 6.7. Inclusion pattern of the graphene-based material. Inclusions are in the hexagon pattern, colored in yellow. The distance between the adjacent inclusions is 10 nm, the diameter of the inclusion is in the range from 4 nm to 8 nm. 103

Figure 6.8. Number of breaking bonds in the membrane as a function of time for different samples. The radius of graphene-like inclusions R_I is, (a) 2 nm,

(b) 3nm, (c) 4nm..... 104

Figure 6.9. Number of breaking bonds in the membrane as a function of time for different samples. The elastic modulus of graphene-like inclusions E_I is, (a) 0.5 E_G, (b) 2 E_G. 104

List of Tables

Table 1.1. Tribological properties and potential application of biological systems. 8

Table 2.1. List of hard tissues with high anti-wear performance, and their degrees of mineralization and functions. 13

Table 4.1. The mechanical properties of HAp calculated from (001), (010), (110), and (110) planes in comparison with the values reported in literature. 72

Table 4.2. The values of H/τ_y and $\gamma_s/\tau_y D_p$ calculated from the (001), (010), (110), and (110) planes of single crystal HAp. D_p is taken as 2 nm. 73

Chapter 1. Introduction

Through billions of years of evolution, Mother Nature has endowed all lives essential skills and abilities to adapt to the severe environment. There are a lot of natural materials with various functions, and these natural materials have drawn much attention due to their interesting properties, *e.g.* light-weight, high-strength, high-toughness, large stretch [1], flexible-switch between attaching and detaching [2], and self-cleaning properties [3, 4]. Then, some questions arise: how Mother Nature can build a variety of materials with such unique structures and properties, and what is the mechanisms behind the structures and properties? A lot of researches reveal the unique properties of these biological materials, and they find that those unique properties rely on the complex structures ranging from macro- to nano-scales, such as, the hierarchical structures on the surfaces of lotus leaves resulting in unique self-cleaning property [5, 6], the hierarchical structures on gecko foot transforming weak van der Waals interactions at nanoscale into huge adhesion forces at macroscale [7] and ceramic platelets aligned with organic layers at nanoscale in nacre and bone utilizing several toughening mechanisms. In addition to the efforts devoted to revealing the relationships between these unique structures and novel properties of natural materials, there is a growing effort devoted to developing and fabricating bioinspired materials by using those mechanisms observed in nature to achieve the novel properties. Most

of them with organic and inorganic components are built in perfect assembly from the micro- to nano-scales. Various synthetic methods have been used to fabricate bioinspired materials that resemble biological materials' structure and function, such as self-assembly [8-11], lithography [12-14], and so on. In the thesis, the attentions are focused on mechanical phenomena existing in natural materials, especially, unique tribological behaviors (anti-wear and anti-fouling), and fracture-modes-controlled behaviors. The objectives are to explicate the mechanism behind these unique behaviors from the viewpoint of mechanics. In spite of the investigations that are focused on the specific biological systems, the mechanical mechanisms to be revealed can be extensively used as the general guidelines for related bioinspired applications.

1.1 Basics of natural and bioinspired materials

In the early of 1950s, most natural materials were studied only by biologists. However, natural materials have drawn much attention from material scientists due to the fancy materials properties since 1950s. For instance, from the point of view of material science, bone exhibits many novel properties, *e.g.* low-density, high-strength, high-toughness, mechanical-efficiency [1, 15], which has two weak major constituents: biopolymer and biomineral. So, a question arises: How nature can fabricate the material with such high strength and toughness by using such weak constituents? With the above doubt, material scientists devoted themselves to dig the mechanisms out and

find a way to fabricate the bioinspired materials. In this respect, some researchers provided a guideline containing 3 steps to realize the process [16-18]: (1) Explicating the relationships between structure and function of natural materials; (2) Distilling the physical and mechanical mechanisms of the relationships; (3) Developing fabrication protocols to obtain bioinspired materials. An enormous amount of experimental characterization and theoretical analysis on various biological materials are done, such as recent researches on nacre shell [19], gecko foot [20, 21] and *Nepenthes* [22], which show that hierarchical structures ranging from macro- to nanoscale give rise to the fancy functions of natural materials, and the complex structures are optimized by nature.

Among numerous natural materials, nacre, as a common material with the brick-mortar structure found in many shells, is often used as a model to explore how the natural composites achieve such fancy properties. Nacre shell (Figure 1.1) is comprised of aragonite platelets and organic matrices [19]. The platelets can increase the structural stiffness, whereas the organic matrices between platelet layers can control the nucleation and growth of the mineral crystal in the biomineralization procedure [23, 24].

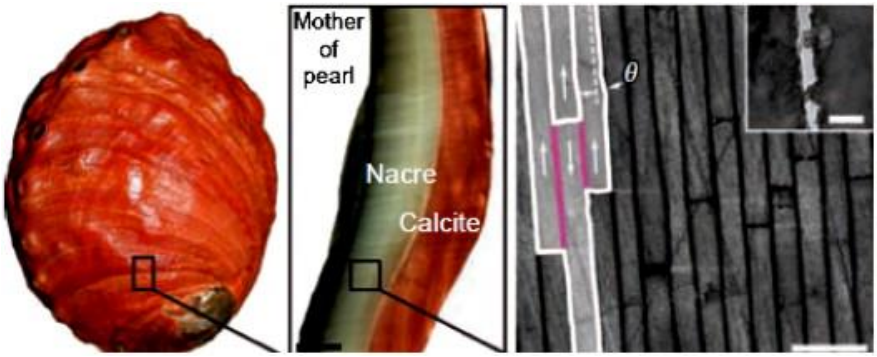

Figure 1.1. Hierarchical structure of Abalone nacre (adapted from [19]).

The key mechanism for the high toughness is due to the refined interfacial architecture and achieved by the sliding between platelets, which can dissipate an amount of energy. Basing on the mechanisms, theoretical models extracting the structure-function relationship have been built for bioinspired material design. Jackson *et al.* built a theoretical model for nacre-like composites, in which elastic modulus can be calculated by the shear-lag models, and the tensile strength can be described by pull-out failure mode. However, the model cannot predict the fracture toughness [25]. Tang *et al.* built an elasto-visco-plastic interface model to explain the strengthening mechanism, and the corresponding simulations indicated a hardening mechanism, which was consistent with the finding from the experiments [26]. Jäger *et al.* presented Jäger–Fratzl model considering the mineralized fibrils, in which the mineral platelets were arranged in careen pattern [27]. Based on Jäger–Fratzl model, Gao *et al.* found that the strength and toughness of these biological materials are insensitive to flaws at nanoscale, also called flaw-tolerance principle, which is important in regulating the high strength and toughness of nacre-like materials [28]. Ji *et al.* incorporated the

tension-shear chain into the Dugdale model [29] to estimate the fracture energy (Figure 1.2) [30]. From experimental characterizations and theoretical analyses, it is found that the platelet and organic interface contribute to the strength and toughness of the nacre-like structures, and these studies represent principles to design strong bioinspired structural materials.

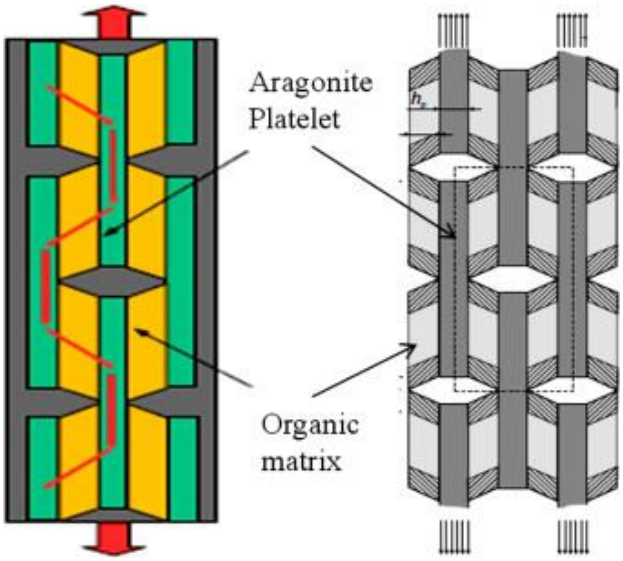

Figure 1.2. Tension-shear chain model of the natural composites (adapted from [30]).

In addition to the nacre, there are enormous mechanical mechanisms provided by nature, which are more complex than those existing in engineering materials. So study the mechanisms from natural materials is an important and facile way to create engineering materials with fancy properties. In line with the aforementioned three steps, firstly, we need to do experimental characterization of natural materials, which can bring us a direct observation of structure; then, we can extract the quantitative relationships between structures and functions and mechanism behind the phenomena based on the experimental data; finally, we can design and fabricate the new

bioinspired materials by following the theoretical guidance.

1.2 Mechanics in natural and bioinspired systems

The mechanical behaviors of natural and bioinspired materials are important for their proper function. Not only for the natural materials whose main function are structural such as skeletal and protective tissues, but also for other tissues and biomaterials. Moreover, there are relationships between mechanical and biological functions at various spatial and temporal scales. It is therefore necessary to study the mechanical behaviors and properties of natural materials.

As an important branch of mechanics, the study of friction, wear, and lubrication, termed tribology, has received increasing attention as the function of various mechanical and biological systems depend on the appropriate tribological properties. As a relatively new field, tribology has also found numerous research objects from nature *e.g.*, crawling of gecko, crawling of insects, wear of joints, adhesion of cells. The morphology, mechanical properties of surface materials and the contact mechanics in biological systems have been studied and investigated by various researchers. As an important component of tribology, friction and adhesion play vital roles in daily life. Various organisms, like geckos (Figure 1.3) and insects use friction force to climb and crawl. The adhesive force is important, and it depends on the micro- and nanostructure on the pad of the apparatuses [2, 20, 21, 31, 32].

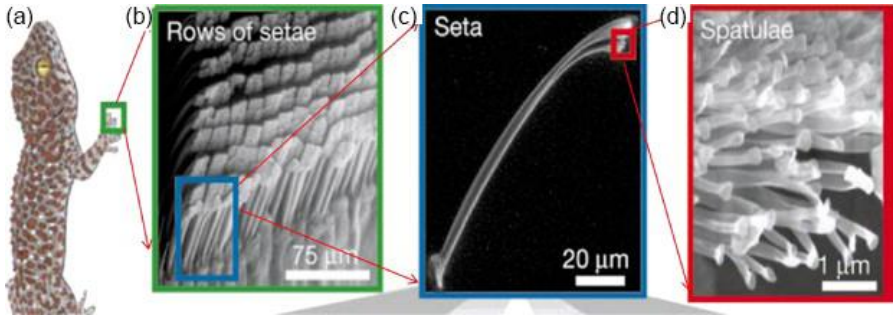

Figure 1.3. The structure of a gecko foot from macro- to nanoscale. (a) Gecko; (b) seta array; (c) single seta; (d) spatulae on tip of seta (adapted from [20]).

Inspired by snakeskin (Figure 1.4) wherein the skin with anisotropic frictional properties, a bioinspired polymer surface was developed. The frictional coefficients of surfaces with various morphologies were measured. It is found that the stick and slip behavior due to the texture influences the surface abrasion [33].

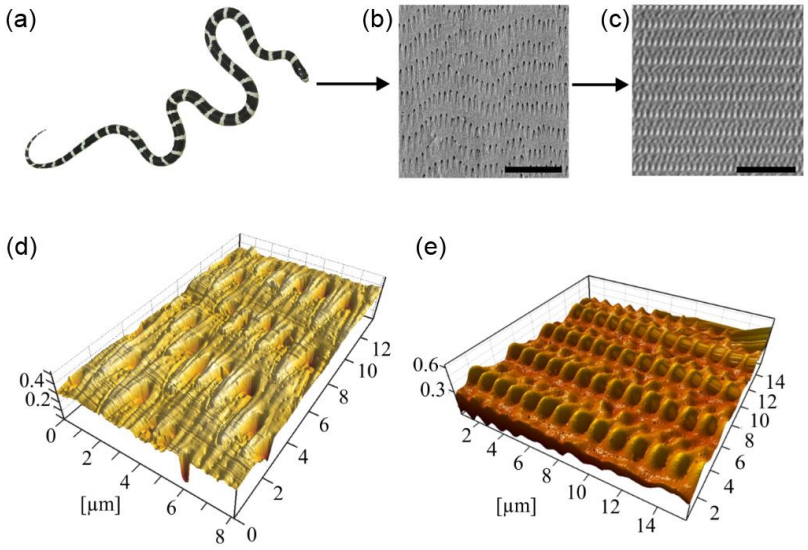

Figure 1.4. From snakeskin to snake-inspired micro-structured polymer surfaces (SIMPS). (a) Photograph of *Lampropeltis californiae*; (b) SEM image of *L. californiae* snake skin; (c) SEM image of SIMPS. 3D image of (d) *L. californiae* snake skin and (e) SIMPS based on AFM data (adapted from [33]).

Similar to friction, lubrication is another important field of tribology. Lubrication plays an important role in anti-wear and controlling contamination. Recent advancements in the nanoscale lubrication have reformed the concept of traditional lubricants, for example, a bioinspired lubricant based on the anti-wear mechanism of cartilage [34].

Table 1.1. Tribological properties and potential application of biological systems.

Biological system	Tribological property	Potential application
Teeth	Anti-wear	Composite materials with anti-wear properties
Octopus	Enhanced adhesion	Robots holding devices
Lotus leaf surface	Self-cleaning	Surface modification for anti-fouling
Gecko feet	Adhesiveness and grip	Adhesive textures in robotic manipulators

Natural systems provide a lot of inspirations for the research in the field of Tribology. Nevertheless, numerous efforts are still to be made. Following are various areas (Table 1.1 provides a list of biological systems) which can serve as potential,

1. Research on the anti-wear mechanism of the hard tissue and development of bioinspired composite materials based on these mechanisms for better anti-wear and anti-friction properties;

2. Research on the anti-fouling mechanism of some typical marine organism surfaces and development of coating and paint based up these surfaces for better anti-fouling performance;

3. Research on extreme pressure lubricants and armor structural materials in biological systems and development of lubricants and protecting coating for sliding and impacting contacts under high loading conditions.

In addition to tribology, fracture mechanics are applied to gain understanding of strengthening and toughening mechanisms of natural materials. At the most elementary level of the structural hierarchy, bone-like and nacre-like materials exhibit a generic structure consisting of hard mineral platelets with the parallel pattern arranged in soft organic layers on the nanometer scale. These mechanisms can help us to develop the bioinspired materials with novel anti-crack (high-toughness) properties.

1.3 Objectives and outline of this thesis

The focus of this thesis is to study some typical mechanical behaviors in biological materials and related bioinspired materials. In Chapter 2, I firstly review recent studies on the mechanical behaviors of natural materials and related bioinspired applications, including the anti-wear natural materials, the anti-fouling natural materials, the fracture modes controlled natural materials and the related bioinspired applications. Then in Chapter 3, the experimental methods including the characterization methods of the biological materials and the synthesis methods of the bioinspired materials are presented, followed by a fundamental introduction molecular dynamic (MD)

simulations method. Subsequently, the high wear resistance of the teeth of black carp is studied in Chapter 4. The mechanism of the superior wear resistance of the black carp teeth occlusal surface (OS) is found. In Chapter 5, I demonstrate that the excellent anti-fouling performance of the *Sonneratia apetala* leaves can be attributed to their ridge-like surface morphology, and following theoretical modeling indicates that shape ridge would reduce the attachment probability. Then in Chapter 6, the fracture behavior of bio-inspired graphene-based structure under impact is studied through MD simulations. By optimizing the geometrical structures of the inclusions in the graphene membrane, the controlled fracture behavior can be achieved. Finally, the results of this thesis are summarized and discussed, followed by the outlook to the future work in Chapter 7.

Chapter 2. Research background and literature review

Biomechanics deals with mechanics concerned with biological systems. As one of the most rapidly growing field of mechanics, it can help us understand how the biological systems work as well as how bioinspired material and structures should be manufactured. Mechanical studies on some typical biological systems are reviewed in this chapter. A brief introduction of the development, as well as current focuses on biomechanical research, is stated according to symbolic journal papers in this area. Progress in anti-wear, anti-fouling and anti-crack (fracture modes controlled) biological and bioinspired systems is presented.

2.1 Anti-wear natural and bioinspired materials

The organisms experiencing billion years of evolution are usually granted with several fancy capabilities to adapt to the severe environment. A typical example is the surface of the body (protective armors) and the invasive apparatus, which show exceptional surface mechanical properties ascribed to the specific surface morphology and structure, such as low frictional coefficient and anti-wear performance. The studies on anti-wear mechanism in nature would contribute to the development of bioinspired anti-wear materials.

2.1.1 Anti-wear performance of natural materials

Surface contacts are common in the daily lives and play important roles in machines and tools with moving parts. The removal of material in sliding contact surfaces results in wear. Wear may result in damage to surfaces and failure of structures. Currently, in addition to the conventional lubrication method, a lot of advanced technologies have been developed to minimize wear in industry, including film and composite-materials coating on contact surfaces. Because the loss caused by wear in the industry is huge (estimated to be 1–2% of GDP), better solutions of anti-wear are needed in materials science and engineering [35]. Biological systems also involve wearing. To protect the body against wear and attack, many organisms have evolved novel materials to curtail the wear of their armors or predation tools. From the Material Science and Engineering perspective, mimicking the structure of these hard tissues with such high anti-wear performance can bring a lot of help to the development of novel bioinspired materials with superior anti-wear performance.

Here, these numerous hard tissues can be classified into two kinds according to the mineral content: (i) tissue with high mineral; (ii) tissues with medium to low mineral; or unmineralized. This classification is justified from mechanical properties perspective (*e.g.* hardness or modulus) by the clear contrast in of the minerals compared to the unmineralized components. The high mineralized is defined as the

mineral phase above 75 vol.%. Three functions of these hard tissues are classified: (i) protective armor (*e.g.* mollusk shells), (ii) supporting skeleton (*e.g.* bone and coral), and (iii) predation bio-tool (*e.g.* teeth and horse hoof). Table 2.1 provides a list of hard tissues that may have a high anti-wear performance, and typical examples of the hard tissues are displayed in Figure 2.1.

Table 2.1. List of hard tissues with high anti-wear performance, and their degrees of mineralization and functions.

Biological materials	Degree of mineralization	Function
Nacre	High	Protective armor
Conch	High	Protective armor
Chiton teeth	High	Predation tool
Sea urchin teeth	High	Predation tool
Bone	High	Supporting skeleton
Fish armor	High	Protective armor
Human teeth dentin	Medium	Predation tool
Turtle shell	Medium	Protective armor
Horse hoof	Low	Predation tool

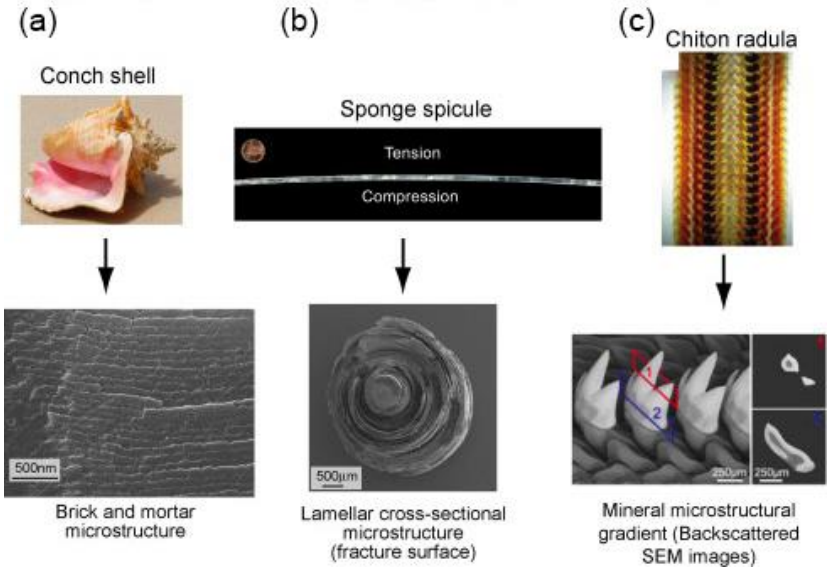

Figure 2.1. Typical examples of biological materials with high wear tolerance. Three typical types (a) protective structures (conch shell), (b) supporting skeleton (*Sponge spicule*) and (c) predation bio-tool (*Chiton radula*) (adapted from [36]).

2.1.2 Anti-wear mechanism of the natural materials

Wearing has a complicated process comprising chipping, cutting or rubbing. Surface morphology contact stress and the presence of lubricant all influence the wear performance of the systems [36]. The importance of above factors in the wear process is diverse. From the mechanical perspective, the wear hinges on a combination of mechanical properties, such as hardness, strength and fracture toughness. In fact, predicting the anti-wear performance remains rather slippery, and the intuitive experience that the harder the better anti-wear performance is not always right in reality.

Among numerous hard tissues, teeth are the most distinctive structures. Their functions are not the only mastication of food, but also include attacking prey and defense. Thus,

anti-wear performance is critical for teeth. In the following discussion, the mechanisms of mammal species especially the human teeth are chosen as the emphasis.

The human teeth have a hierarchical structure. There are two main components, enamel and dentin. Enamel, as shown in Figure 2.2, is the outer layer, which need to bear wear during eating for the whole life. As shown in Figure 2.2, the highly mineral enamel layer is at the uppermost of the tooth crown. And the detin is underneath the enamel. The constitution of dentin is different from that of enamel. In macroscale, there is a transition layer between enamel and dentin. Enamel is the hardest parts of the body, while dentin is softer than enamel like the bone. The dentin-enamel-junction (DEJ) transition region serves as a part playing a toughening role. These parts combine perfectly through fancy micro- and nanostructures to give rise to novel anti-wear property.

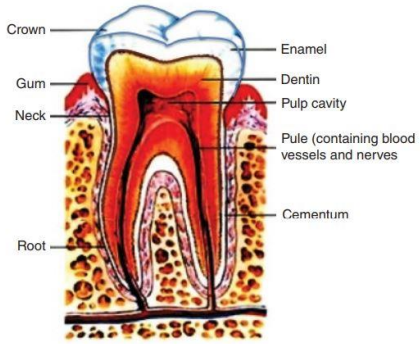

Figure 2.2. Schematic of tooth strucuture, illustrating enamel, dentin, and dentin-enamel-junction (adapted from [38]).

The composition of enamel is bio-ceramics, secreted by *ameloblasts* cells. The

hierarchy of enamel is attained through the accurate biomineralization procedure. Overall, enamel composes of 92–96 wt.% hard mineralized phase, 1–2 wt.% soft organic phase, and 3–4 wt.% water [37, 38]. As shown in Figure 2.3, the hierarchical structure can be classified into various level with length scales ranging from nanometer to micrometer: hydroxyapatite (HAp) nanocrystals, protein nanofibrils array, fiber bundles, microscale prisms, keyhole-shaped structures, and prism bands [39, 40]. The elementary units are HAp crystallites (shown in Figure 2.3a) with needle-like shape. One single HAp crystalline has a width around 68 nm and a thickness around 26 nm. These needle-like crystallites are combined with enamelin to form nanofibrils (Figure 2.3b). The nanofibrils form larger-scale enamel rods (Figure 2.3c). Depending on the location in the rods, the orientation of the HAp crystallites varies. In the core part, the crystallite are parallel to the rod axis while those in the edge part array with an angle of around 45° to the rod axis [41]. The upper level of the enamel is the arrange pattern of the rods. The rods with 5 μm diameter are covered by thin protein-rich layer. The rods are organized along the direction perpendicular to the DEJ layer (Figure 2.3d). The mechanical properties of these rod are different depending on the orientation of HAp crystals [42]. The hardness of the thin protein-rich layer is 74% lower, while the elastic modulus is 53% lower of that of the rods [42]. With such novel mechanical properties, the protein-rich layer may introduce unique toughening mechanisms. The enamel with such high toughness and good anti-wear performance is constituted

hierarchically by these elementally units.

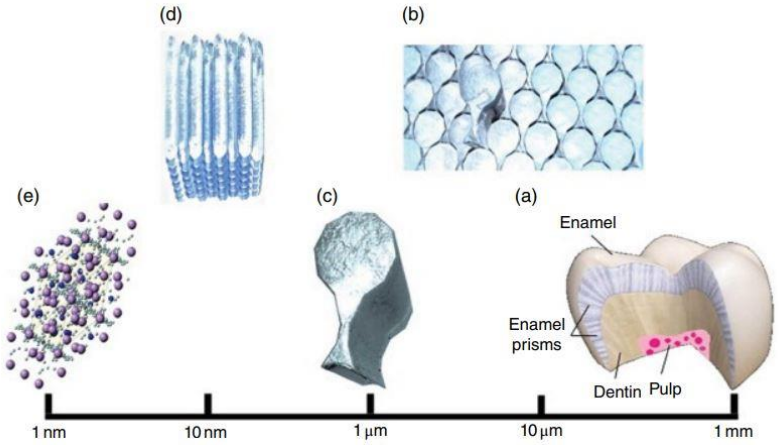

Figure 2.3. Images of hierarchical structure of a tooth from nano- to micro-scale (adapted from [39]).

As discussed in the review of the teeth enamel, one design principle contributing to the anti-wear performance of the enamel is its hierarchical structure. Different from conventional ceramics, enamel with hierarchical structure has organic components in nanoscale. The second design guideline that gives rise to the anti-wear performance of the enamel is the layered structure in which a hard coating (the enamel) deposits on a soft substrate (the dentin) [43, 44].

2.1.3 Bioinspired materials with anti-wear performance

Biological materials have various structures and work in different wear conditions. These environmental factors can influence on the material structures, so what can we learn from nature and what principal factors give rise to the novel anti-wear performance?

In regenerative medicine field, wear is a main cause for implants failing [45], for example, elastic incompatibilities of the alloys at joints, leading to wear and fast failure of the prostheses [36]. Therefore, the elastic modulus and hardness of dental materials should approach those of dentin, so the wear of the material could be minimized. To fulfill the requirements, a synthetic material for artificial enamel, polymer-infiltrated-ceramic-network (PICN) (shown in Figure 2.4), was developed [46]. This material has a hybrid structure with ceramic and polymer networks, mimicking the interlocking structure of the natural teeth. Because of the similar interlocking structure of the natural teeth, this material has an approximate strength, elasticity and tribological properties to dentin, and the wear is comparable to the conventional dental ceramic. The Weibull modulus, used to measure the reliability of a material, is quite high. The indentation test on hybrid ceramic showed that the crack path could be stopped by the interpenetrating polymer. This gives an explanation to the good anti-wear performance of PICN [47].

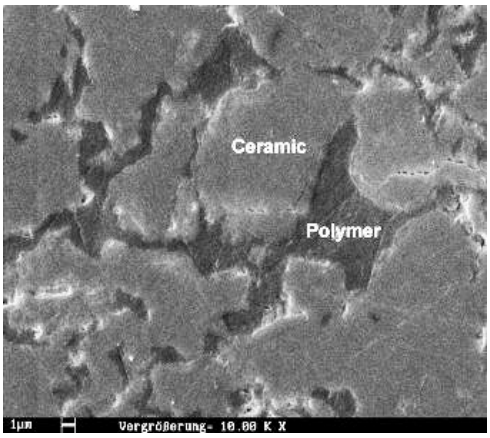

Figure 2.4. SEM image of polymer-infiltrated-ceramic-network structure (adapted from [47]).

Some biological material, for example, rat teeth utilize abrasive wear to form sharp cutting edges then to reduce the wear of the whole teeth. This strategy is different from the tools in conventional industry. The horseshoes-shaped outer zone of the teeth has an extremely anti-wear material, while the cutting face has softer bonelike dentine. An interlocking structure connects the two parts. The inner hard enamel at the cutting edge is exposed as the dentine wears, then the tooth is sharpened (shown in Figure 2.5).

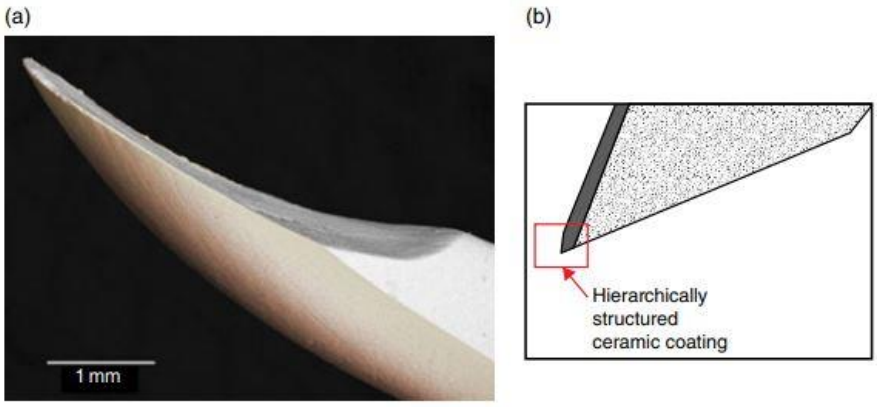

Figure 2.5. (a) SEM image of rat tooth tip. (b) Schematic of rat tooth-mimicking cutting tool (adapted from [50]).

Inspired by such novel structure and anti-wear mechanism of the teeth, cutting tools with good anti-wear performance were developed [48]. The core part of bioinspired tool was made up of chisel tool steel with high toughness, like dentin part of the teeth. To mimic the enamel, the flank surface of the cutting edge is deposited with a ceramic layer with enough hardness, which has high wear resistance. Bioinspired strategy learned from the rat teeth's hierarchic structure is combining brittle and ductile phases at the nanoscale with specific microstructure. Different from the cutting edge of the

conventional cutting tools, which has obvious wear damage after long-time use, the bioinspired blade shows a near-none wear rate. The novel anti-wear performance can be attributed to the self-sharpening effect.

2.2 Anti-fouling natural and bioinspired materials

Marine biofouling refers to the unfavorable settlement and growth of marine sessile organisms (*e.g.*, barnacles, mussels, and tubeworms) on the surfaces immerged in the ocean. However, bio-fouler also have their rivals. Through billion years of evolution, many organisms have effective defensive strategies against the fouling organisms. The mechanisms behind these strategies provide us numerous environment-friendly approaches to traditional biocidal anti-fouling (anti-fouling) paints.

2.2.1 Anti-fouling performance of natural materials

Anti-fouling mechanisms of organisms have been developed with several model organisms across marine animals and plants for twenty years. The model organisms include gorgonian corals, whale skin, the dogfish egg case, red algae, shark skin and mollusks [49-53].

As one of the first bioinspired models, gorgonian coral, *Pseudopterogorgia acerose*,

was studied due to its novel anti-fouling performance. *P. acerose* shows multiple anti-fouling strategies and is rarely fouled in the marine environment [54]. There are spiculas with a mean roughness of 2-4 μm on the surface of the gorgonian. The surface energy equals to 20-30 mN/m, which can achieve minimal bio-adhesiveness. Such cooperative mechanisms result in a surface against settlement of diatoms, while no resistance against bacteria [54]. As with many other model anti-fouling organisms, the gorgonian surface quickly fouls after dead, which means that the surface propeties are not the whole anti-fouling mechanism.

Another model for bioinspired anti-fouling technologies development is the egg-case of the dogfish, *Scyliorhinus canicular*. Unlike other anti-fouling natural surfaces, its surface energy is similar to glass which is easily fouled. However, similar to most natural anti-fouling models, the microtextured surface of the dogfish egg case has a mean roughness of 3.7 μm [55].

Sharkskin, having been studied initially due to the drag-force reduction property in the water [56, 57], is another recent focus for bioinspired anti-fouling model. It has been analyzed that a lot of shark skins show micro-morphological ridges, but the length of the micro-ridges and spacing between the micro-ridges varies slightly from 30 to 300 μm [58]. However, the patterns are the same across species with the riblet shape (shown in Figure 2.6).

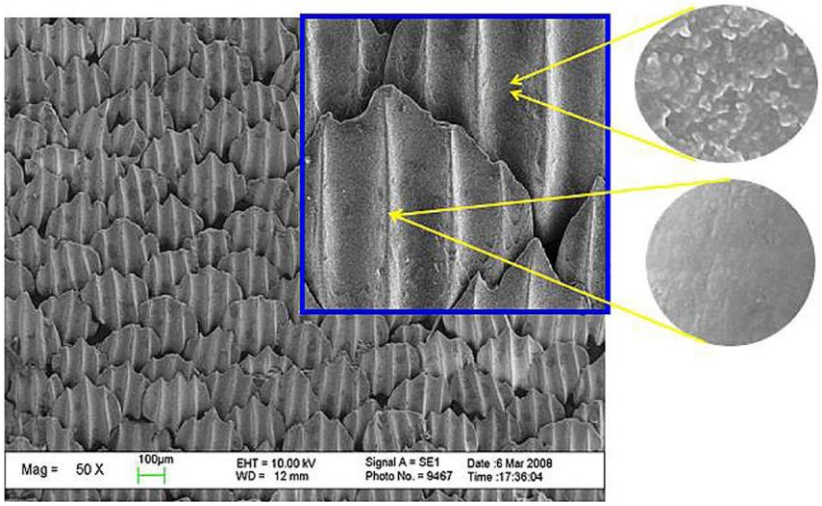

Figure 2.6. SEM image of the riblet structures of the shark skin surface (adapted from [59]).

Similar with gorgonian coral, the egg-cases of the dogfish and shark skin, various marine mollusk species, show good anti-fouling performance. The surface morphologies of the shells are due to the outermost proteinaceous layer, which is fouling deterrent and prevents fouling organisms boring [59, 60]. In a study of the pearl oyster *Pinctada margaritifera* (shown in Figure 2.7), the presence of proteinaceous layer correlated with the absence of fouling organisms. Similarly, *Pinctada fucata*, shows fouling with age increasing due to the loss of proteinaceous layer [61]. And if the proteinaceous layer was physically removed from the shells, the degree of fouling increased [59].

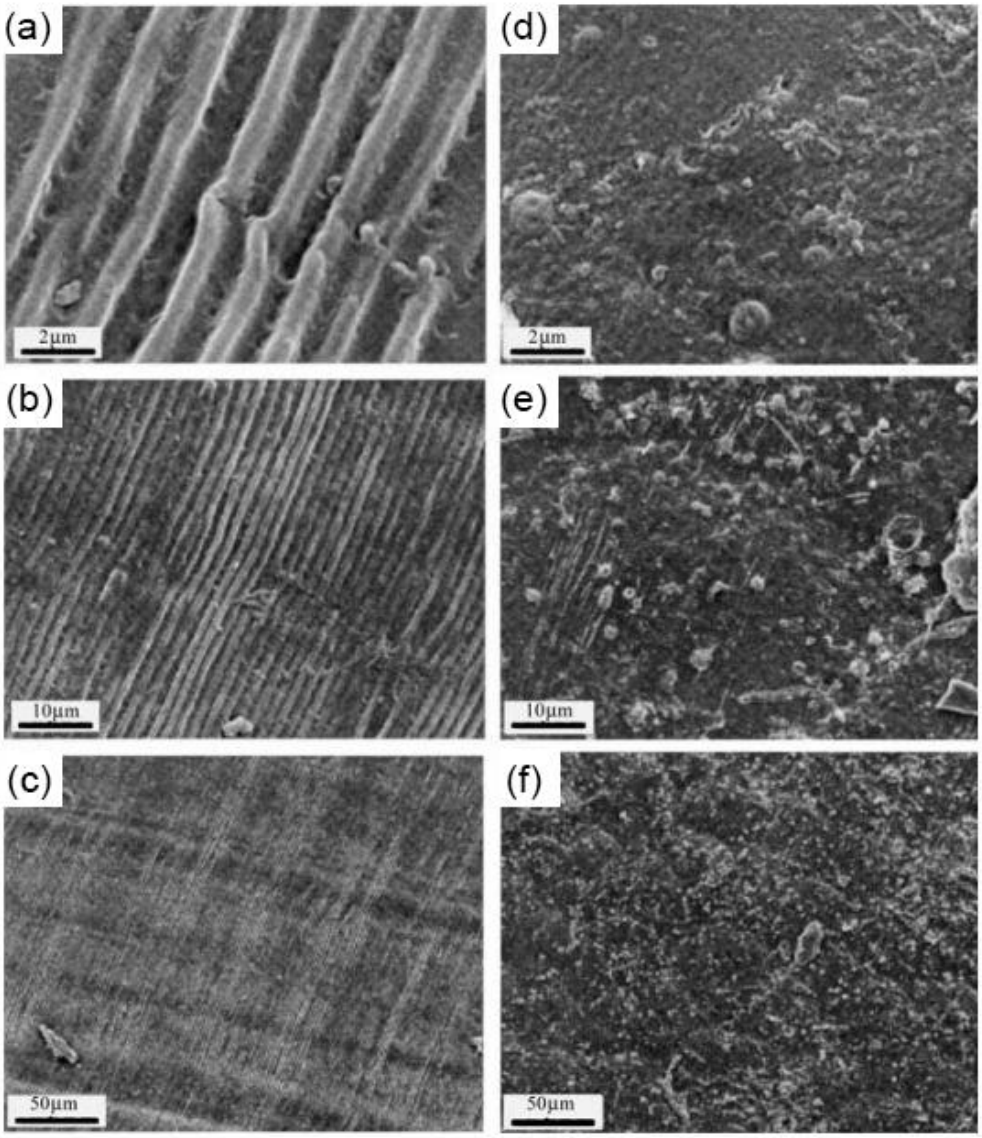

Figure 2.7. SEM images at various magnification scales of (a–c) *M. galloprovincialis*, (d–f) *P. imbricate* (adapted from [62]).

2.2.2 Bioinspired materials with anti-fouling performance

Now, there are many opportunities for the development of bioinspired anti-fouling materials, and there are several natural anti-fouling models that require in-depth investigation. In addition to the organism that discussed above, the other aquatic organism *e.g.* fish, crustaceans, elasmobranchs, sponges and cetaceans all offer chances to gain more understanding of natural anti-fouling mechanisms. Such anti-fouling mechanisms will bring a lot of inspiration to new anti-fouling materials design. Among numerous anti-fouling mechanisms, combining nano- and micro-morphology and surface properties is becoming a hot spot for anti-fouling coating development [62].

Among numerous new developments in anti-fouling materials, the main theme for bioinspired anti-fouling materials is micro-morphological surfaces ranging from 1 to 300 μm. This is due to numerous evidence from natural anti-fouling surfaces that micro-morphology smaller than the settling fouler reduce settlement probability and attachment strength. The structures in the range of 50 to 90% of the characteristic length of a settling larva show best anti-fouling effectiveness [63]. Natural anti-fouling surfaces have multiple-scale morphologies and the design of multiple scales of morphology is a key step in bioinspired anti-fouling materials development. The anti-fouling surfaces with multiple-scale morphology can be realized by the production of

hierarchically-wrinkled surfaces. The length scales of hierarchically-wrinkled morphologies are in the range from nanometers to millimeters [64]. After treating in ultraviolet light and releasing the uniaxial strain, the PDMS materials with wrinkled morphology can be fabricated, which shows five different periodicities (shown in Figure 2.8). By stretching the PDMS over a hemispherical substrate and releasing the biaxial strain, wrinkled morphology with three orders of periodicity can also bee prepared [64]. These surfaces process novel anti-fouling performance in field tests. However, when the surfaces with hierarchically-wrinkled morphologies are exposed to spores of *Ulva* in bioassays, the morphology shows less effectiveness in reducing spore settlement than the surface chemistry. Thus, combining surface morphology and chemistry is treated as a direction where the most potential advances of anti-fouling materials can be achieved.

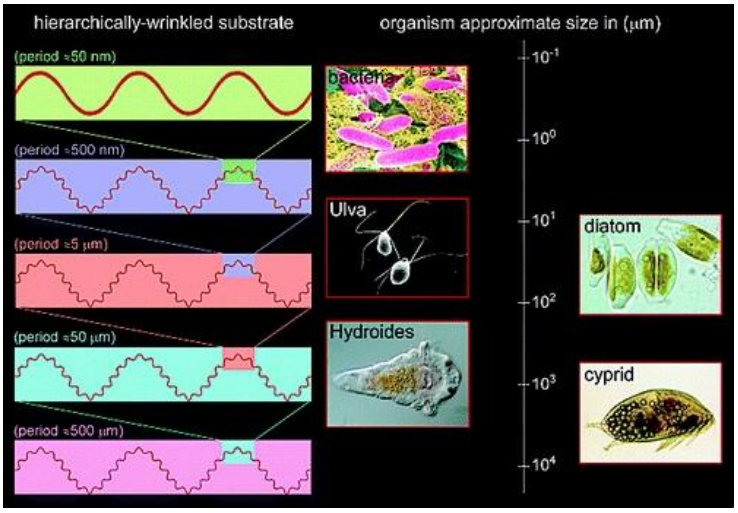

Figure 2.8. Hierarchically wrinkled coatings for marine anti-fouling (adapted from [66]).

In addition to surface morphology, another factor affecting the anti-fouling performance is surface wettability. The development of surface modification technologies facilitates the manufacture of surfaces with controlled surface properties, from super-hydrophilic to super-hydrophobic [53, 62, 65, 66]. At a molecular level, researchers have gained a lot of knowledge on the effects of surface properties on cellular adhesion and anti-fouling, especially for biomedical applications [67]. Although the anti-fouling performance of numerous superhydrophobic surfaces have been studied in the lab [53, 66], little is still known about the effectiveness in the field. In the marine environment, no matter the surfaces are hydrophobic or hydrophilic, they show a species-specific anti-fouling performance [63], the effectiveness of the extreme surface properties cannot be proved. Some bioinspired superhydrophobic surfaces lose anti-fouling efficacy after immersion and the fouling rapidly initiates once the superhydrophobic property is lost [68]. Some researchers think that the most useful factor associated with superhydrophobic surfaces may not be decreasing the adhesive force, but rather the scale of roughness [63, 68-72]. Inspired by the skin of the pilot whale, researchers developed a bioinspired surface that can facilitate nano-scale air incursions on the surface [69] (shown in Figure 2.9). In the study examining fouler settlement on the bioinspired surface, this superhydrophobic coating with nano-scale morphology averts the settlement of all model fouler. The researchers stated that the coating with nano-scale air incursions had a larger unwetted area to prevent settlement

and it can trap air at the solid-liquid interface, and it may be a key factor to be considered in the development of anti-fouling coating. However, most surfaces, regardless of superhydrophobic or superhydrophilic show a species-specific anti-fouling performance, more factors should be taken into consideration in real-world usage.

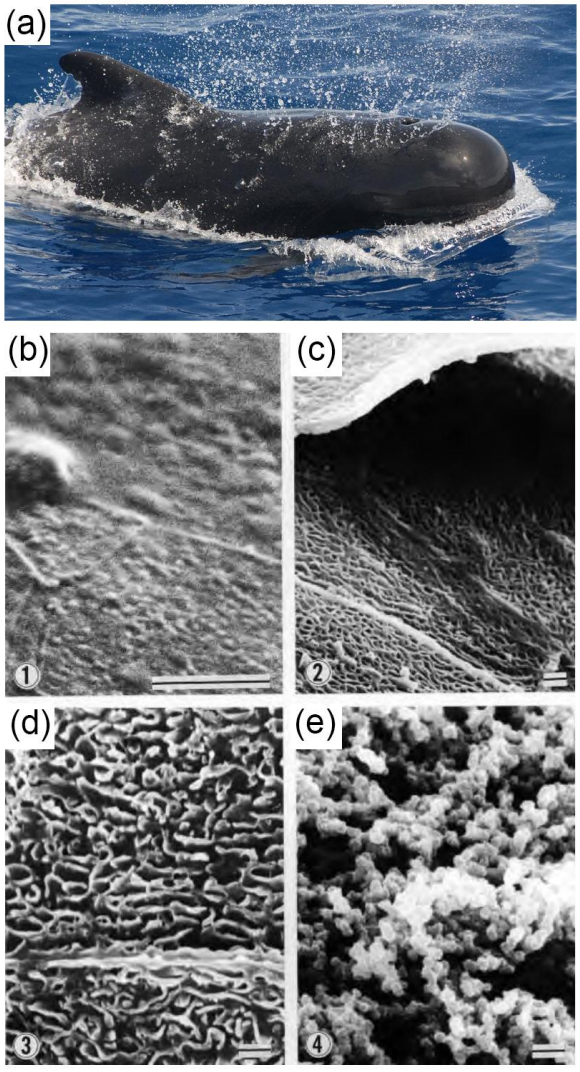

Figure 2.9. (a) Image of the pilot whale. (b-e) SEM images of the skin of the pilot whale (adapted from [69]).

Multiple anti-fouling strategies are present in marine organisms where chemical, physical and mechanical anti-fouling mechanisms are combined to stop the attachment of various fouler. Thus, a consistent topic in bioinspired anti-fouling system development is multiple anti-fouling strategies, which combine physical, mechanical and chemical defenses. The realization of bioinspired multiple anti-fouling strategies is one of most common methods to fabricate anti-fouling surfaces. Due to the low surface energy of polydimethylsiloxane (PDMS), combining PDMS with modified morphologies, which is slightly below the scale length of the fouler larva, could effectively deter attachment [73]. The other factor in pursuing bioinspired anti-fouling technologies is evaluating the target surface in field and in-situ, where the effectiveness of the surface in the real world can be assessed [53, 60, 63, 66, 74, 75].

2.3 Fracture modes controlled natural and bioinspired materials

Nature utilizes innovative approaches to activate strengthening and toughening mechanisms hierarchically, thereby gaining high strength and toughness simultaneously. Natural materials can have novel combinations of high stiffness, giant strength, immense toughness and low density, which are better than artificial synthetic materials. Nature can fabricate composites several orders of magnitude stronger and tougher than the component that they are made from, *e.g.*, abalone shell and spider silk. Although the mechanical properties of bio-composites cannot surpass those of

engineering materials, what attract our attention is how they organize the week building blocks and achieve heighten properties. Thus, scientists are turning to nature for the inspiration and design principle on strengthening and toughening mechanisms.

2.3.1 Anti-crack performance of natural materials

Natural materials are quite diverse. Based on the components, they can be into three broad groups: (a) mineralized materials, consist of hierarchical composites of minerals, such as hydroxyapatite (HAp), amorphous silica and calcium carbonate; (b) polymeric materials, which composed of organic constituents, such as collagen, chitin, lignin, and other biopolymers; (c) mixture materials with hierarchical structure and various constitutions. Among these natural materials, teeth, bone and nacre are known for the most impressive property, the fracture toughness, which is around thousand times higher than the mineral component. These natural ceramics are highly mineralized, so high toughness is critical, which mean that the cracks arising from original defects in the tissues can be deterred, then making the structure damage tolerant. In addition to the hard tissues mentioned above, some polymeric materials have drawn attention from Material Science and Engineering because of their superior properties compared to existing fiber. Among these polymeric materials, spider silk displays a toughness that is around three times that of artificial fibers such as Kevlar, while having extreme strength comparable to steel.

As one of the most attractive bio-composite in biomimicry, nacre exists in the inner layer of the mollusk shells against attack and impact from predators. It has novel mechanical properties, especially toughness. The characteristic structure of nacre is "brick and mortar" at the microscale (Figure 2.10), which consists of 95% aragonite form calcium carbonate ($CaCO_3$) and 5% organic matrix located at the interface between $CaCO_3$ platelets. The mineral brick is a polygonal microscale platelet with diameter of 5-15 μm and thickness of 0.5-1 μm. The organic mortar shows a laminar structure consisting of chitin, silk-like proteins, and polysaccharides. Although occupying only 5% of the total volume, the organic mortar plays a critical role in enhancing strength and toughness by providing the strong adhesion between the platelets. In addition to the basic mineral platelet and thin polymer layer structures, there are other features at the interface between the mineral platelet and thin polymer layer. One is the nano-asperities on the platelet surfaces, which can deter the sliding of the platelets. Another is the mineral bridges, which can reinforce the platelets across the interfaces. All the features, combined with the "brick and mortar" structure, give rise to the novel strength and toughness.

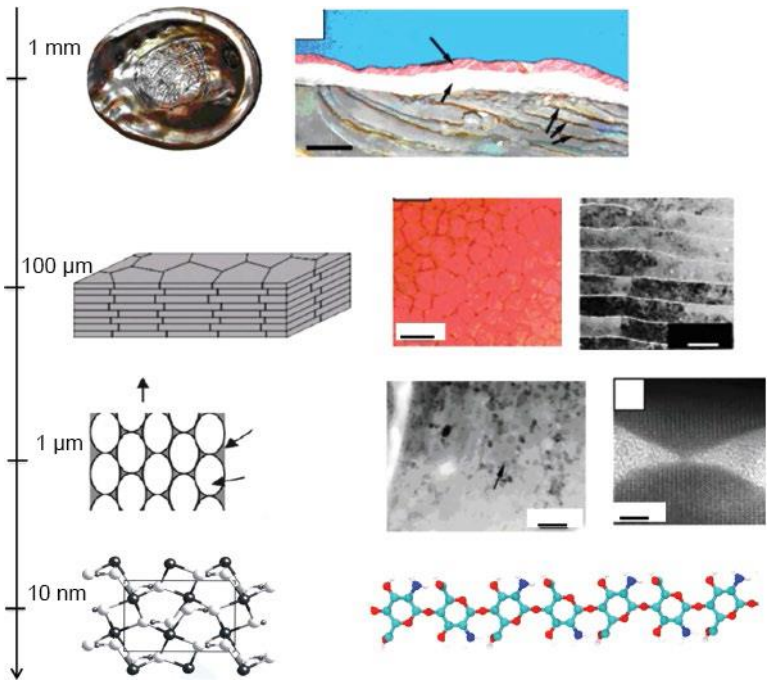

Figure 2.10. The hierarchical structure of nacre from macro to nanoscale (adapted from [76]).

Depending on the hydration condition, nacre shows different responses to loading. Hydrated nacre can sustain non-elastic deformation and relatively large strains, whereas dry nacre shows a common brittle behavior, which is like bulk aragonite, as shown in Figure 2.11. Yielding stresses is around 60-70 MPa, and failure strain is around 1% with failure strength of around 100 MPa. For hydrated nacre, the tensile load is spread through the structure by shear stresses at the interfaces and the tensile stress in the platelets. Although the strain at failure is much lower than many engineering materials such as alloys, it is ten times the failure strain of pure aragonite, which makes a significant difference in the toughness. Overall, nacre achieves a good balance between the toughness and strength.

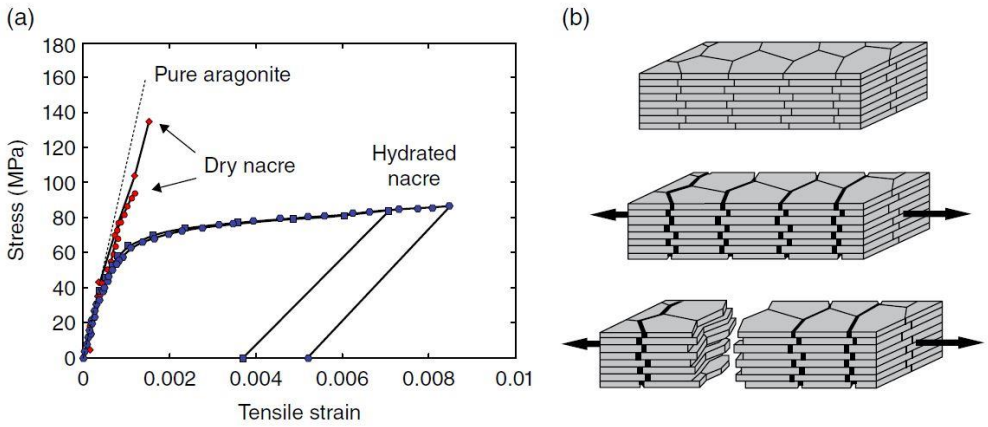

Figure 2.11. (a) Stress-strain curve of nacre under tensile loading. (b) The schematic of the failure of the hydrated nacre (adapted from [77]).

As one of the most amazing natural fibers, spider silk stands out due to the higher tensile strength and toughness, as well as better stability in harsh environments. It can be extended to 2-4 times its original length without failure. Like other polymeric bio-composites, spider silk, has hierarchical structure, as shown in Figure 2.12. Spider silk has a “skin and core” structure at the macroscale. These circular core filaments are aligned parallel to the axis and cemented together (Figure 2.12b). Each filament consists of hard crystals and soft chains at the nanoscale. The hard crystals occupy around 10% of the volume with the length/width ratio being around 5, as shown in Figure 2.12c. The protein chains with an amorphous structure occupy the remainder volume. The crystals serve as reinforcing parts to strengthen the silk, while form the intermolecular network between the protein molecules. The length of the amorphous chains are around 16-20 amino acid residues, and the large-scale extension of the amorphous chains in the hydrated silk results in the rubber-like elasticity. At the

molecular level, the peptide strands crystals bond together by hydrogen bonds (Figure 2.12d), which is individually weak, but collectively strong. The crystalline regions are super-hydrophobic, which results in the insolubility of silk: water molecules cannot penetrate the hydrogen-bonded structures.

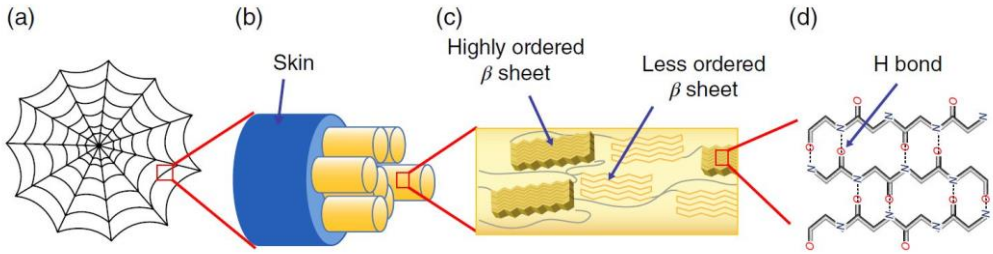

Figure 2.12. Schematic of the hierarchical structure of spider silk. (a) The web. (b) Silk fiber (c) Filaments (d) β-crystal peptide strands (adapted from [78]).

Spider silk shows novel mechanical properties, such as high strength, toughness and great extensibility. Among all synthetic and natural fibers, spider silk shows best ability to absorb energy, and unit weight spider silk can absorb three times energy than, Kevlar, the strongest synthetic fiber, as shown in Figure 2.13. Synthetic fibers with a rigid molecular structure exclude the potential of large deformation. Thus, the high strength is achieved at the expense of extensibility. In contrast, spider silk displays a good balance between the high strength and great extensibility.

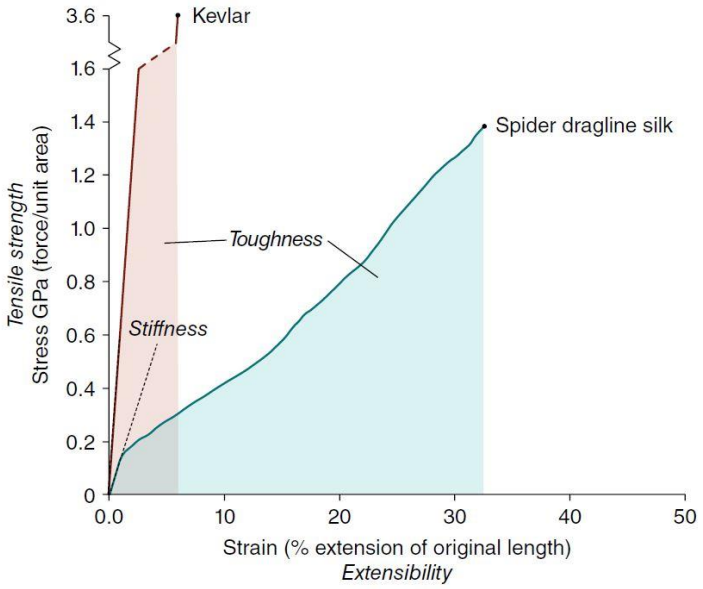

Figure 2.13. Stress-strain curve of *N. clavipes* spider silk compared to artificial fibers under tensile loading (adapted from[79]).

2.3.2 Anti-crack mechanism of the natural materials

As stated above, the function of the hard mollusk shells is to protect the soft body against attack and impact from predators. The bending loading on the exterior of the shell loaded will translate to the inner nacreous layer as tension loading, which may cause the failure of the brittle inner layer. When platelets in nacre are subjected to tensile stress, pre-existing flaws can cause stress concentration in the platelets, which result in the crack propagation and the catastrophic failure of the shell. According to fracture mechanics, the maximum stress σ_{max} that a structure with a crack can sustain is obtained by the Griffith equation:

$$\sigma_{\max} = \sqrt{\frac{2\gamma_s E}{\pi a}} \tag{2.1}$$

where a is the crack length, E is elastic modulus, γ_s is the surface energy. The Griffith fracture criterion Eq. (2.1) can be used to predict the theoretical strength. For specific materials, the strength scales inversely with the size of the crack a: *smaller the crack stronger the structure*.

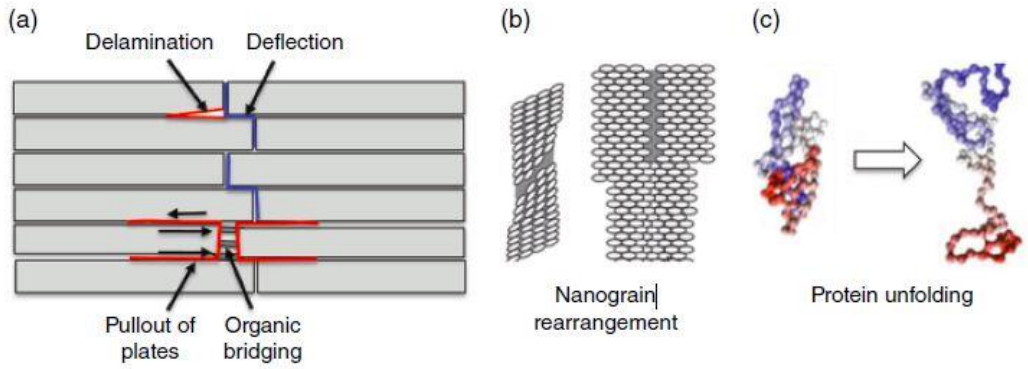

Figure 2.14. Toughening mechanism of nacre from macro- to nano-scale. (a) Toughening mechanism at the micrometer scale. (b) Intra-platelet toughening mechanism at the tens nanometer scale. (c) Toughening mechanism at molecular scale (adapted from [80]).

In the natural composite material, crack deflection around reinforcements is one of the most common toughening mechanism. The unbroken reinforcements restrain crack propagation. The number of toughening mechanisms of nacre is at least ten [81]. These toughening mechanisms can be classified into three divisions based on the architectures: (1) nano- to micrometer interactions between laminates (*e.g.*, crack deflection, interfacial delamination, and platelets interlocking), (2) nano-structural

toughening (*e.g.*, bridging and sliding of nanograins) and (3) energy dissipation induced by the softer protein layers (*e.g.*, polymeric layers bridging between plates, chain folding and unfolding, and crumbling of cross-links), as shown in Figure 2.14.

The novel mechanical properties of spider silk emanate from its hierarchical structure, which range from molecular to macro-scale (as shown in Figure 2.12). Each level contributes to the incredible property of the fiber. As shown in Section 2.3.1, the crystalline-amorphous domains respond to external loading in a complicated pattern [78]. The amorphous part can deform, contributing to the extensibility under tensile loading, while the harder nanocrystals play the strengthening role. Such a structure provides enough toughness and strength.

2.3.3 Bioinspired materials with controlled fracture

By applying the design principle of layered composites, a nacre - like platelet - reinforced composite with incredible mechanical properties has been developed. One guideline of nacre being strong and tough simultaneously is to make the thickness of the platelets in nanoscale range. The other is to ensure the aspect ratio of the platelets smaller than the critical value S_c. The critical value Sc can be obtained from the value of the fracture strength of the platelet divided by the shear yield strength of the polymer matrix. By following these guidelines, alumina platelets with σ_f of 2 GPa and a polymer with τ_y of 40 MPa were used to fabricate of the nacre-like composite. As shown in

Figure 2.15a–c, in the Al_2O_3/GO-PVA artificial nacre, Al_2O_3 and GO-PVA act as "brick" and "mortar", respectively. The artificial nacre shows high strength (143 ± 13 MPa) and toughness (9.2 ± 2.7 MJ/m^3) (shown in Figure 2.15d), which are better than those of nacre (80–135 MPa, 1.8 MJ/m^3) [10]. These results indicate that the GO-Al_2O_3 composite with hierarchical structure can deal with the conflict between strength and toughness. These results prove the validity of the biomimetic design principle learned from the natural materials with excellent strength and toughness.

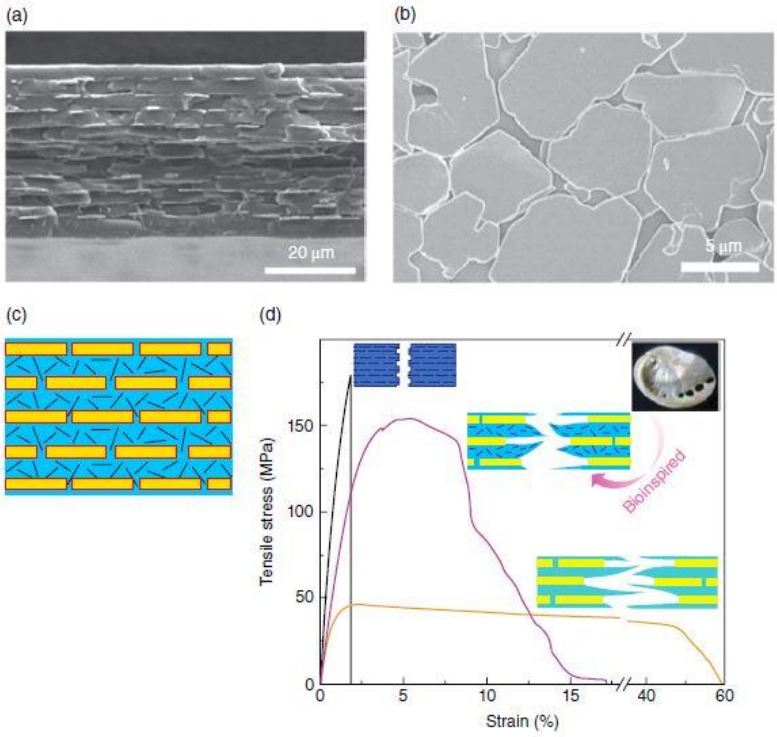

Figure 2.15. Structure and mechanical properties of nacre-like material. (a) SEM image of the layered structure; (b) SEM image of Al_2O_3 monolayer onto GO-PVA layer; (c) Schematic of nacre-like material, and (d) Comparison of mechanical properties of nacre-like and with those of layered GO/PVA and Al_2O_3/PVA (adapted from [80]).

Spider silk is a good prototype for the bioinspired fiber with ultra-tough and ultra-strong properties. Considering the novel mechanical properties, spider silk can be widely used in various scenarios. One strategy for producing the spider silk is to obtain protein recombinant from the genetically modified organisms. However, this strategy has been limited due to the lack of full gene sequences for spider silk proteins. Alternatively, based on the theoretical modeling, synthetic materials can be used to fabricate bioinspired fibers, as shown in Figure 2.16. Carbon nanotubes (CNTs) with extreme strength, high stiffness, low density, and stability, are ideal building blocks acting as “nanocrystalline” in silk. The nanotubes were integrated into macroscopic composites with a high degree of alignment to mimic the microstructure of spider silk. The poly(vinyl alcohol) (PVA) were used to reproduce load transfer mechanisms in natural silk. The soft mediates optimize the interactions between neighboring nanotubes to achieve hydrogen-bond breaking and reforming under the loading. Between the CNT bundles, there is dense network of hydrogen bonds, which work cooperatively to transfer loading under large deformation, thus providing a toughening mechanism [82], as shown in Figure 2.16c.

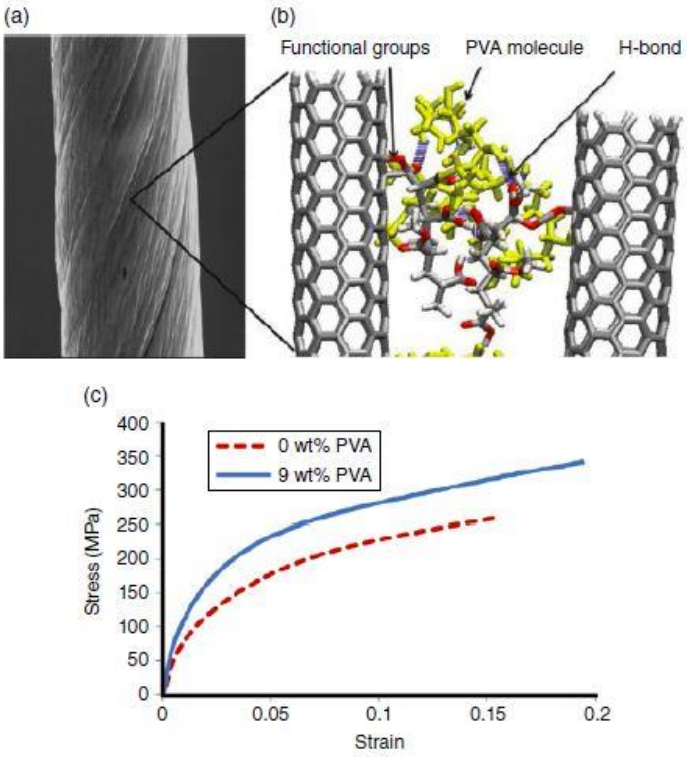

Figure 2.16. (a) Bioinspired carbon nanotube fiber. (b) Schematics of hydrogen-bond structure in the fiber.(c) Stress-strain curves of DWNT-PVA fibers with 0 and 9 wt% PVA (adapted from[82]).

Chapter 3. Research methods

In this chapter, I firstly introduce the techniques and experimental protocols used in this thesis for material properties characterization, materials synthesis and samples preparation. Then, the fundamental of molecular dynamic (MD) simulation method and the force field adopt in the study were introduced.

3.1 Experimental methods

3.1.1 Wear resistance evaluation

In tribology, no single and general unit exists for the evaluation of wear resistance compared to other mechanical properties (*e.g. E*, the elastic modulus is a capacity of the resistance to being deformed elastically and toughness is the ability of a material to absorb energy before fracturing.). The wear behavior depends on other elementary mechanical properties, such as the elastic modulus, the hardness, the fracture toughness of the surface materials and the wear conditions (lubrication, wear particles, *etc*.). With comparable variables, nano-scratching test can be used in characterizing the wear resistance of materials at the nano-scale. Besides, this technology has been employed to evaluate the tribological behavior of human enamel [83-85].

Nano-scratching tests

The instrumented nanoscratch by Hysitron is an adaptable tool for various materials analysis. In the nano-scratching test, a normal load in a controlled setting is applied to the probe on a test surface whereas the force for moving the tip laterally is measured. By setting an appropriate normal load function and scratching path, various types of tests can be conducted. The damage and wear are then observed by using SEM and AFM. Figure 3.1 shows the SEM image of typical scratch grooves on human teeth enamel by nano-scratching.

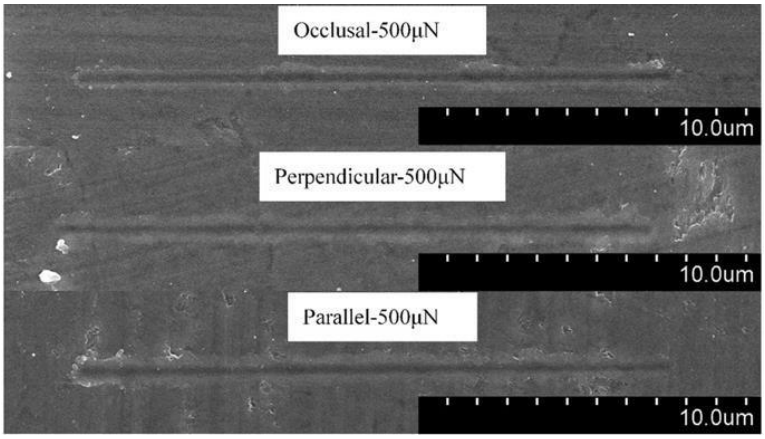

Figure 3.1. SEM image of scratch grooves on human teeth enamel by nano-scratching (adapted from [85]).

3.1.2 Materials characterization

SEM images of the scratches

Scratched samples were sputtered with gold in the vacuum and FESEM (S-4800, Hitachi) imaging was conducted with accelerating voltage of 5 kV.

Comparative XRD analysis of enameloid

To reveal the crystallographic structure in enameloid, comparative X-ray diffraction (XRD) analysis was carried out, in which X-ray diffraction was conducted on enameloid specimens in both powder and bulk forms. The powder specimen was obtained by grinding the bulk enameloid. All the diffraction patterns obtained were compared with the standard pattern (International Centre of Diffraction Data, Powder Diffraction File).

Surface morphology characterization of Sonneratia apetala leaves and the PDMS replica

Freeze-drying *S. apetala* leaves and the PDMS replica were sputtered with gold in the vacuum and SEM (VEGA3, Tescan) imaging was conducted with accelerating voltage of 20 kV. Figure 3.2 shows the SEM image of *S. apetala* leaves.

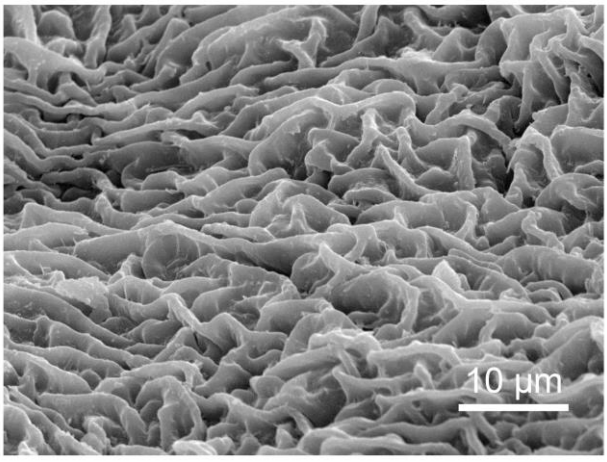

Figure 3.2. SEM image of *S. apetala* leaves.

3.1.3 Materials synthesis and samples preparation

Preparation of PDMS replicas of Sonneratia apetala leaves

To evaluate the anti-fouling performance of the surface morphology of *S. apetala* leaves and mask other possible factors such as bioactive compounds, PDMS replicas of *S. apetala* leaves are prepared by a molding process (as shown in Figure 3.3).

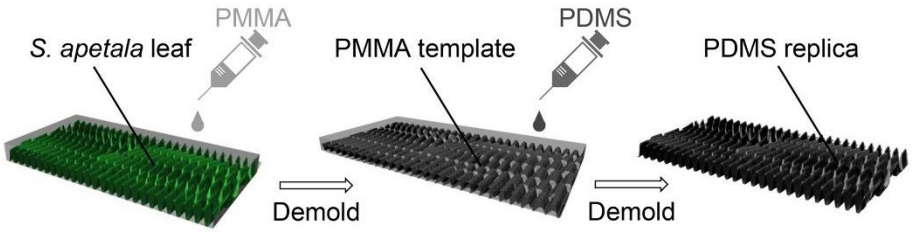

Figure 3.3. Schematic of the molding process for preparing PDMS replica of *S. apetala* leaves.

Firstly, the *S. apetala* leaves were cleaned by using acetone and dried in ambient temperature. Then, the polymethyl methacrylate (PMMA) solution (acetone as solvent) was poured onto the treated leaf's surface. After curing of the PMMA, the leaf was removed from the PMMA, giving rise to a negative PMMA mold duplicating the morphology of the leaf. Then, the PDMS mixture (base and crosslinker were mixed in a volume ratio of 10:1), was poured onto the negative PMMA mold. The whole set was placed in a low-pressure desiccator for degassing for 1 hour. After curing at room temperature for 48 h, the PDMS replica was obtained after demolding by using acetone to dissolve the PMMA mold.

Synthesis of biomimetic anti-fouling surface

To further verify the finding from the theoretical modeling and overcome the size limitation of replica of *S. apetala* surfaces, a synthetic surface with ridge-like morphology is prepared by water bath method with graphite paper in a aqueous solution containing Nickel and Cobalt nitrates.

Firstly, a piece of graphite paper (GP) was rinsed with acetone and distilled (DI) water, and then dried in the vacuum oven for 12 h at 80 °C. Then, the treated GP was immersed into a solution made by dissolving 0.5 mmol $Ni(NO_3)_2 \cdot 6H_2O$, 1 mmol $Co(NO_3)_2 \cdot 6H_2O$ and 2.2 mmol hexamethylenetetramine into 20 mL DI water and 10 mL ethanol. The GP together with the solution was transferred to a Teflon-lined stainless-steel autoclave and kept at 90 °C water bath for 6 h. Subsequently, the GP covered with $NiCo_2O_4$ nanoflakes was obtained after cooling down at room temperature. Finally, after thorough rinsing with DI water and ethanol followed by drying at 60 °C for 12 h, the $NiCo_2O_4$ nanoflakes with GP substrate was ready for anti-fouling performance evaluation.

3.1.4 Anti-fouling performance evaluation

To examine the anti-fouling performance of the target surfaces (PDMS replicas of *Sonneratia apetala* leaves and synthetic $NiCo_2O_4$ surfaces with ridge-like morphology), settlement tests of tubeworms are carried out with flat PDMS samples and glass slides used as the controls.

The Culture of the tubeworm larvae for settlement tests

In the culture process, adult tubeworms *H. elegans* (Figure 3.4a) were collected from a bay near Yung Shue O, Hong Kong. Eggs and sperms (Figure 3.4b) were released by breaking the tubular shells of the tubeworm adults with tweezers, then were collected by using a pipette. Fertilization was carried out by mixing the eggs and sperms for 30 min in filtered seawater (with 0.22 μm mesh sized filter) with these environment conditions: ambient temperature (25 °C), normal pH value (~8.1) and salinity (34 psu). Subsequently, the embryos were raised at the density of 5 ml^{-1} in the culture tanks for 5-7 days. During this period, the seawater was refreshed every other day and the larvae were fed with algae *Isochrysis galbana* (about 105 cells ml^{-1}). The larvae aged 5-7 days (see Figure 3.4c) were ready for settlement tests.

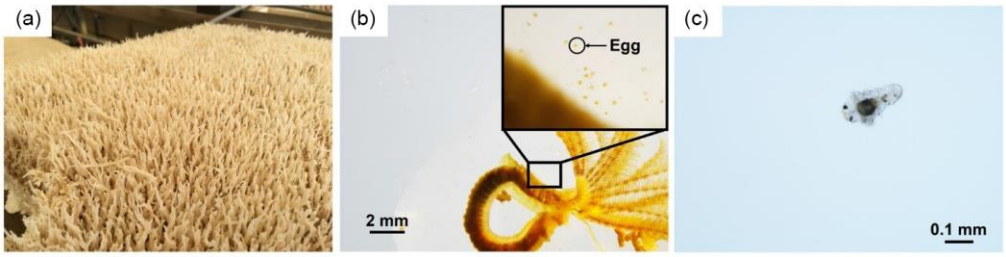

Figure 3.4. (a) Adult tubeworms *Hydroides elegans* attached on a plastic plate. (b) Adult tubeworm removed from the calcified tubular shell. (c) Larval tubeworm swimming in the seawater to detect the target surface for attachment.

Settlement test with tubeworm larvae

Prior to the test, all samples were immersed into sterile deionized water for sufficient wetting. The wetted samples were placed into a petri dish, which contains 20 ml seawater and ~100 tubeworm larvae (~100 μm in width, ~300 μm in length, as shown in Figure 3.4c). To facilitate the settlement on biofilm-free surfaces like the samples, artificial settlement stimuli (CsCl, 5 mmol/L) was applied. To ensure the repeatability of the settlement results, six replicas were tested in parallel. All the samples were kept in an ambient environment for 48 h in a 12:12 h light-dark cycle. During the test process, the number of settled tubeworms were obtained by using an optical microscope at 24 h and 48 h. Before counting, all the samples are rinsed for three times in filtered seawater to remove any unsettled tubeworms.

3.2 Computational methods

Molecular dynamics (MD) simulation is a valuable approach to predict the nanostructure stability and material properties under the framework of Newton's laws of motion. Physical parameters, such as atomic-stress and atomic-strain can be calculated based on the positions and velocities, with the laws of thermodynamics. In the simulation, atoms and molecules are treated as particles; interactions between these particles are described by empirical force-field or ab-initial potential functions. It is a powerful tool to analyze the material behaviors from atomistic scale to mesoscopic scale, such as trajectories of atoms, the field of atomic-strain, or propagation of cracks tip, which are difficult to observe by experiments at present. MD simulation has been widely applied to explain atomistic phenomena or predict material properties of new material in various fields. In the following part, mathematical manipulations and parameters setting of MD simulations in the thesis are briefly introduced.

3.2.1 Mathematical manipulations of molecular dynamics simulations

From the mathematical perspective, MD simulation is to solve partial derivative equation (PDE) of motion, by finite difference methods. With initial and boundary conditions, the positions and velocities of the particles can be solved by the PDE.

Considering a system with n particles, the i-th particle has m_i as the mass, q_i as the charge, $\mathbf{r}_i$ as the current position, $\mathbf{v}_i$ as the current velocity, and A_i as any other certain

attributes. The total potential energy of the system, E, can be written as the function of the attributes of all particles,

$$E = E(\mathbf{r}_1, \mathbf{r}_2, \ldots, \mathbf{r}_n, q_1, q_2, \ldots, q_n, A_1, A_2, \ldots, A_n) . \tag{3.1}$$

The total energy of the system can be expressed as

$$U = E + W . \tag{3.2}$$

where W is the work done from the exterior environment to the system.

Based on the Newton's second law of motion, the force experienced by each particle, $\mathbf{F}_i$, can be given as

$$\mathbf{F}_i = m_i \frac{d^2 \mathbf{r}_i}{dt^2} . \tag{3.3}$$

At the same time, according to the relationship between force and potential energy

$$\mathbf{F}_i = -\nabla U . \tag{3.4}$$

By combining Eq. (3.3) and (3.4), the PDE can be obtained

$$m_i \frac{d^2 \mathbf{r}_i}{dt^2} = -\nabla U . \tag{3.5}$$

The solution of Eq. (3.5) is the positions of the particles at any time during the interaction process. To solve the PDE by finite difference methods, a commonly used algorithm proposed by Verlet [86] can be expressed as follows:

$$\mathbf{v}_i(t+\frac{1}{2}\Delta t) = \mathbf{v}_i(t) + \frac{1}{2}\frac{\mathbf{F}_i(t)}{m_i}\Delta t \,. \tag{3.6}$$

$$\mathbf{r}_i(t+\Delta t) = \mathbf{r}_i(t) + \mathbf{v}_i(t+\frac{1}{2}\Delta t)\Delta t \,. \tag{3.7}$$

$$\mathbf{v}_i(t+\Delta t) = \mathbf{v}_i(t+\frac{1}{2}\Delta t) + \frac{1}{2}\frac{\mathbf{F}_i(t+\Delta t)}{m_i}\Delta t \,. \tag{3.8}$$

where Δt is the timestep, which is usually 1 femtosecond (fs, 10^{-15} s).

The key to solving Eq. (3.5) is to know the expression of the potential function described by Eq. (3.1), which is later denoted as the force field or potential.

3.2.2 Software for molecular dynamics simulations

In this thesis, all MD simulations are performed by Large-scale Atomic/Molecular Massively Parallel Simulator (LAMMPS) [87], which is developed and distributed by Sandia National Laboratories. Pre- and post-processes the simulation results are realized by visualization program Visual Molecular Dynamics (VMD)[88] and the Open Visualization Tool (OVITO) [89].

3.2.3 Atomic molecular dynamics simulations

MD simulations of HAp

The MD simulations of HAp single crystal (as shown in Figure 3.5) were performed with the LAMMPS.

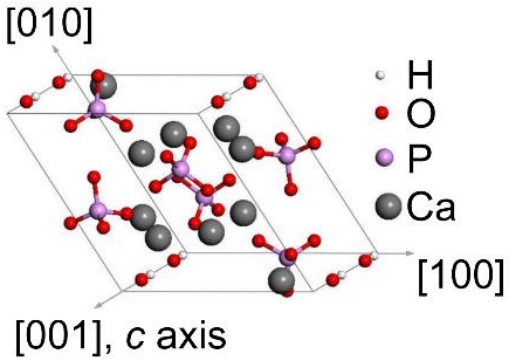

Figure 3.5. Schematics of a unit cell of HAp crystal adopted in the MD simulation.

The extended CHARMM (Chemistry at Harvard Macromolecular Mechanics) force field was used to describe the interactions between atoms in the HAp crystals [90, 91]. The CHARMM force field was used to compute the interatomic Lennard-Jones and Coulombic interactions with an additional switching function that ramps the energy and force smoothly to zero between inner and outer cutoffs [87, 92]. In the simulations, the inner and outer cutoffs were chosen as 6 Å and 10 Å, respectively, so that all atoms inside a HAp unit cell could interact with each other. Each sample was initially relaxed using the canonical ensemble (NVT) for 200 ps. The time step of the simulations was taken as 1 fs and temperature was controlled at 300 K with the Langevin thermostat.

In the nano-scratching and indentation simulation cases, the pyramidal probe (cube-corner) was defined as rigid, consisting of close-packed atoms. Any substantial atom contacting with the probe surface would experience a repulsive force obeying the Lennard-Jones potential $U_{\mathrm{LJ}}(r)=4\varepsilon\left[\left(\frac{\sigma}{r}\right)^{12}-\left(\frac{\sigma}{r}\right)^{6}\right]$ with a cutoff being 2.2 nm, where ε was taken as 0.01 kcal/mole, σ was taken as 2.0 nm and r was the distance from the substantial atom to atom of the probe.

MD simulations of graphene-based structures

The fracture behavior of monolayer graphene-based structure under impact of a projectile with hypervelocity is obtained by conducting a series of atomic MD simulations with LAMMPS. In the simulation, a spherical rigid projectile impacts the graphene-based structure, as shown in Figure 3.6.

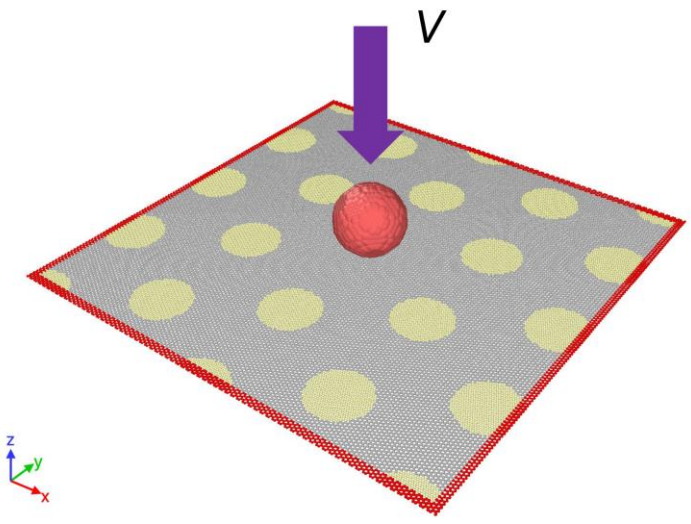

Figure 3.6. Schematic of the graphene-based structure impact simulation.

The adaptive intermolecular reactive empirical bond order (AIREBO) potential was used to describe the C-C bond of the graphene-based membrane [93-97]. The cut-off distance of the C-C bond was set as 2.0 Å to simulate the C-C bond breaking process. The interactions between atoms in projectile and graphene-based membrane were described by Morse potential [98]. Firstly, The graphene-based structure was relaxed to state with a minimum energy by using the conjugate gradient algorithm. Then, the NVT ensemble was used to equilibrate the simulation box at 1 K for 2 ps. Time step of 0.5 fs (10^{-3} ps) was set for all cases.

3.2.4 Coarse-grained molecular dynamics simulations

To shed light on the coupling effect of adjacent adhesion points, coarse grain molecular dynamics (CGMD) simulations were carried out with LAMMPS package. Figure 3.7 shows the simulation model, in which an elastic cylinder is spontaneously attached onto a sinusoidal substrate and then is pulled off from it at a constant speed. Lennard-Jones (L-J) force field $U_{\mathrm{LJ}}(r) = 4\varepsilon[(\sigma/r)^{12} - (\sigma/r)^{6}]$ was applied to describe the interactions between the atoms in the system, including the cohesion inside the cylinder and interfacial adhesion between the cylinder and the substrate. For the substrate, in addition to the flat benchmark, three sinusoidal profiles with λ/R_{T} equal to 0.02, 0.025 and 0.05 were considered with A/λ being taken as 0.5 always. The substrate was assumed rigid by fixing the displacements of its atoms in all dimensions. In each simulation case, the system was initially relaxed using the canonical ensemble

(NVT) for 200 ps. The time step of the simulations was taken as 1 fs and temperature was controlled at 300 K with the Langevin thermostat. Visualization program OVITO was used to visualize and output the simulations results.

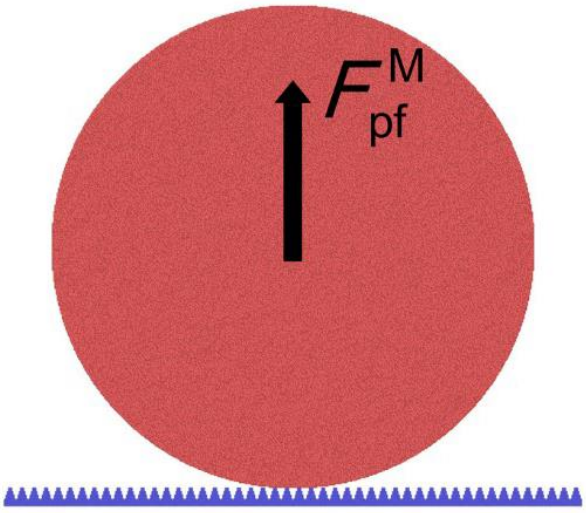

Figure 3.7. Schematics of the CGMD simulation model.

Chapter 4. High wear resistance of the teeth of black carp

Through millions of years, organisms have evolved numerous protective or invasive apparatuses to enhance their survival chance in severe environment. For example, the hard shells of mollusks provide sufficient protection to the vulnerable bodies, while the teeth of vertebrates promote their predatory activities [99, 100]. A lot of effort has been invested in the studies on the protective biomaterials such as mollusk shells [101, 102] and fish scales [103, 104], facilitating the developments of bioinspired materials [105-107]. In contrast, less attention has been paid to the bio-tools of the predators [100, 108], which has comparable value to the development of bioinspired materials. In this study, the pharyngeal teeth of *Mylopharyngodon piceus* (also called black carp) attract my attention due to the unique functionality. Different from the herbivorous fresh-water fishes, black carp mainly feeds on mollusks with hard shells by crushing the shells with its formidable pharyngeal teeth, as shown in Figure 4.1. In view of the fact that black carp teeth can function well upon frequent mechanical interactions (*e.g.* squeezing and grinding) with the hard mollusk shells, the study is focused on the wear resistance of the teeth in this chapter.

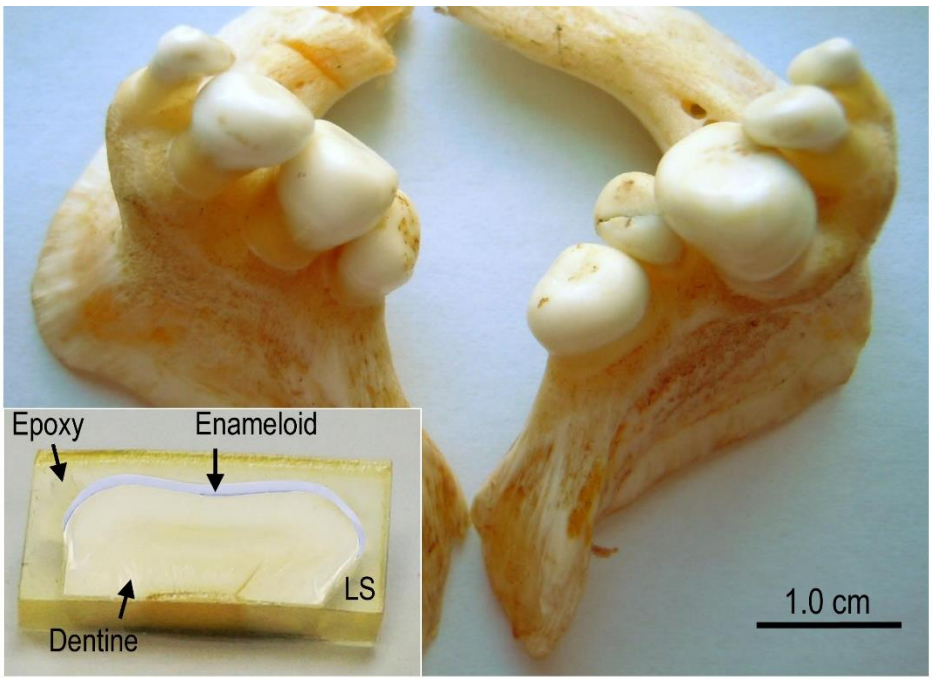

Figure 4.1. Image of *pharyngeal* teeth of black carp with inset showing a tooth embedded in epoxy from the longitudinal section (LS).

4.1 The superior wear resistance of the occlusal surface of the teeth

Different from the human teeth, the outermost layer of black carp teeth does not have the characteristic rod structure observed in the enamel. Therefore, it was called enameloid (i.e., resembling enamel) [109]. In the study, nano-scratching tests were conducted on the occlusal surface (OS) and longitudinal section (LS) of enameloid, which was perpendicular to the occlusal surface (OS) to quantify and compare the wear resistance of black carp teeth. In LS sample preparation process, fresh black carp teeth were incised with diamond saw (Minitom, Struers) along longitudinal section (LS). In prior to the scratching tests, all the surfaces have been well polished to fulfill the surface roughness requirement of the nano-scratching test. Samples were polished by

using 2000 and 4000 grit sand papers (Silicon Carbide Waterproof Paper, PROFIT) for 5 min with lubrication of DI water firstly, then lapped with cloth pad (Micropad Extra, Pace Technologies) in combination with 0.6 μm silica colloid solution (Pace Technologies). Finally, samples were rinsed with DI water and dried in air. Prior to the scratching tests, AFM scanning is conducted to ensure the surface roughness. As shown by Figure 4.2, the roughness of the polished surfaces is around a few nanometers.

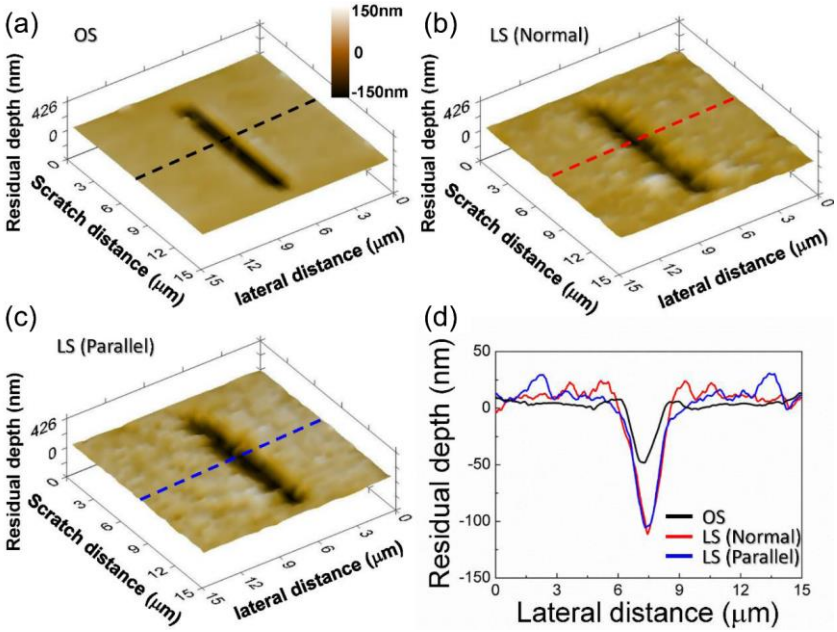

Figure 4.2. AFM images of grooves scratched by 90°conical tip with a radius of 20 μm and the cross-section profiles of the grooves. AFM images of scratches on the (a) OS; (b) LS with scratching direction normal to the OS; (c) LS with scratching direction parallel to the OS. (d) The cross-section profiles of the grooves at the position of dotted lines in (a), (b) and (c).

In the research, nano-scratching tests were conducted on both OS and LS of enameloid by using Triboindenter 950 with diamond Berkovich probe (TI-0039, tip radius = 100

nm) and 90°conical probe (TI-0041, tip radius = 20 μm), respectively. Scratching tests on the LS were conducted along two directions: parallel to the OS and outwards normal to the OS. To exclude the gradient effect of the mechanical properties, all the tests on the LS were conducted within the area less than 50 μm away from the OS, where the variation of the mechanical properties including moduli and hardness can be neglected. In the tests on the OS, scratching was not conducted in a particular direction. Scratching tests were repeated three times for a specific direction to ensure the repeatability of the results. The inter-scratch spacing was taken as 10 μm (around 4 times of the largest scratch width) to avoid the interference between adjacent scratches. The normal load was taken as 2 mN constantly for all the tests with Berkovich probe, while it was taken as 10 mN for all the tests with a conical probe. The scratching distance and scratching time were taken as 10 μm and 20 s, respectively.

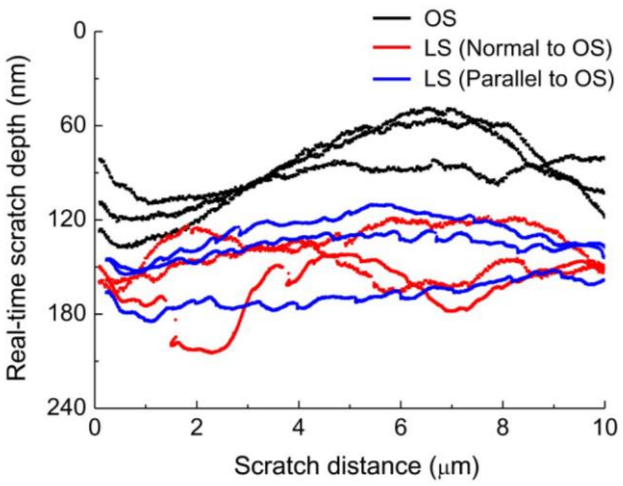

Figure 4.3. Scratch depth of nano-scratching tests on the OS and LS of teeth. OS: Occlusal Surface; LS: Longitudinal Section.

The real-time depths of the scratches are shown in Figure 4.3. It can be found that the mean depth of the scratch grooves on OS is around 80 nm while that on LS is 2 times as that on OS. Field Emission Scanning Electron Microscopy (FESEM) images of the scratch grooves indicates that the response of the OS to scratching differs from that of the LS not only in the width of the residual scratch but also in the failure mode (see Figure 4.4a and b). The mean width of the scratch grooves on the OS is around 0.2 μm, while that on the LS reaches up to 1.1 μm. Scratching on the OS only causes local plastic deformation (see Figure 4.4c and d), while scratching on the LS produces obvious 'pile-up' and debris (see Figure 4.4e and f). The former failure mode is called 'rubbing' mode and the latter one is called 'cutting' mode. Moreover, before scratching the LS exhibits elongated prismatic texture with longitudinal axis perpendicular to the OS (Figure 4.4e and f) [109]. After scratching, this prismatic texture is crushed into granules with diameter around tens of nanometers, as shown in Figure 4.4e and f. In contrast, the 'granular' texture on the OS sustains very well after scratching, as shown in Figure 4.4c and d. Such different responses of OS and LS to scratching indicate that the OS of the black carp teeth has much higher wear resistance compared to the LS.

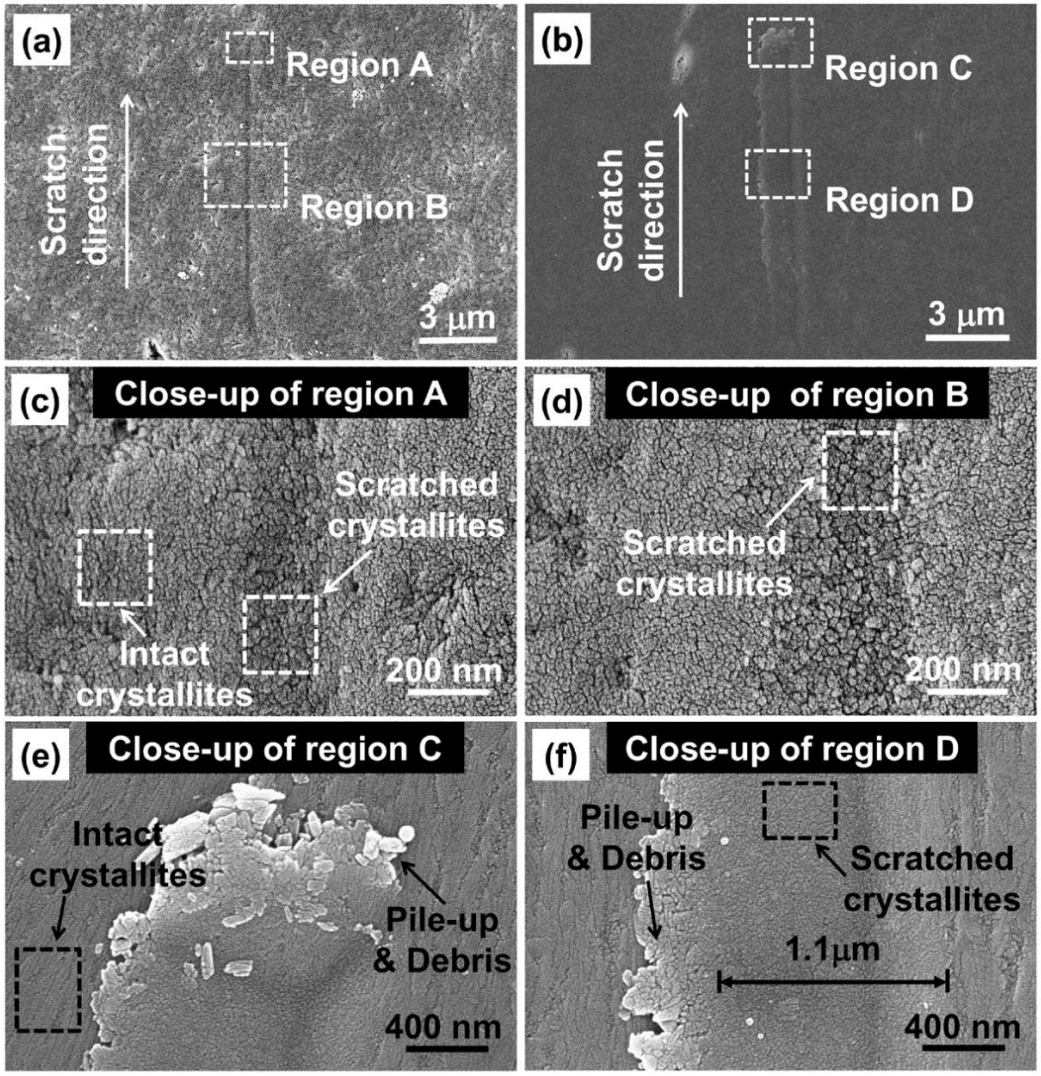

Figure 4.4. SEM images of the scratches on (a) OS and (b) LS; (c-d) close-ups of the regions A and B on OS; (e-f) close-ups of the regions C and D on LS.

4.2 *c*-axis preferential orientation of hydroxyapatite near the occlusal surface

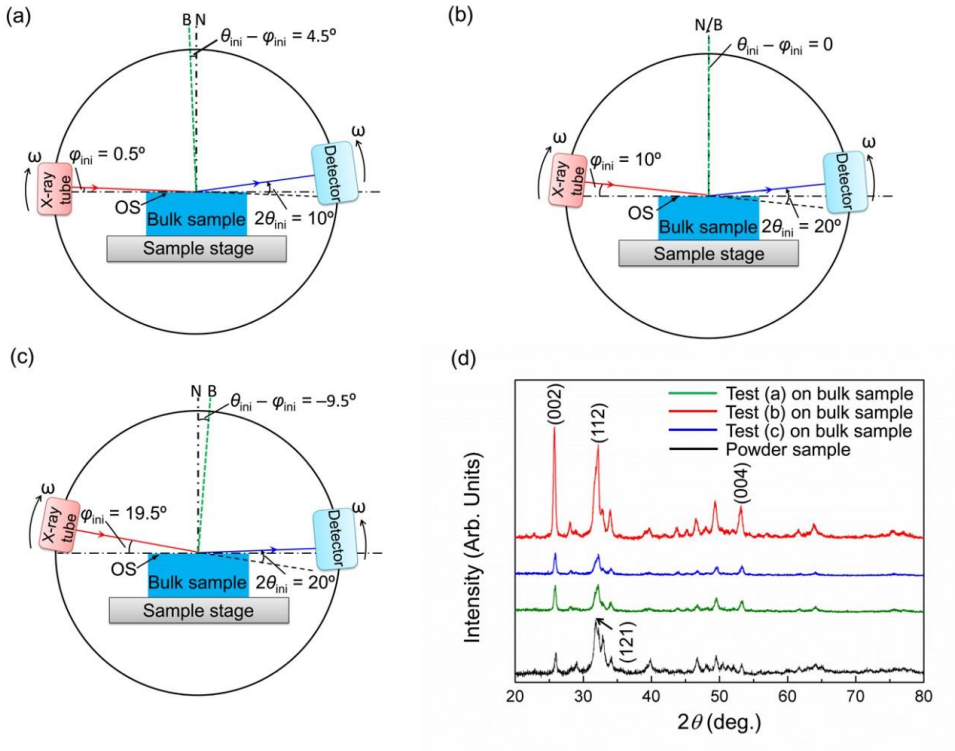

Figure 4.5. (a-c) Schematics of the configurations of three XRD tests on bulk enameloid sample: (a) $\varphi_{ini} = 0.5^{\circ}$, $2\theta_{ini} = 10^{\circ}$; (b) $\varphi_{ini} = 10^{\circ}$, $2\theta_{ini} = 20^{\circ}$; (c) $\varphi_{ini} = 19.5^{\circ}$, $2\theta_{ini} = 20^{\circ}$. (d) Diffraction patterns of three XRD tests on bulk sample in comparison with that obtained from powder sample.

To reveal the possible origin accounting for the prominent wear resistance of OS as shown above, comparative X-ray diffraction (XRD) analysis was carried out on the OS. Traditional XRD analysis usually uses powder sample, so that diffraction beams reflected from various crystallographic planes can be detected due to the random orientation of crystal grains in powder sample. For a bulk material, in which the crystallites are not as random as in powder sample, is used directly as the XRD sample,

the diffraction spectrum may deviate from that of its powder sample. Explicitly, the signal intensity diffracted by the crystallographic planes with preferential orientation would be enhanced to the greatest extent when the diffraction vector coincides with the normal of these planes. Inspired by this guess, the comparative XRD analysis on bulk and powder specimens of the enameloid were conducted to verify the existence of preferential orientation. The powder specimen was obtained by grinding the bulk enameloid. For the bulk specimen, the comparative XRD tests were conducted on the OS by taking the initial incident angle $\varphi_{ini} = 0.5^{o}, 10^{o}, 19.5^{o}$ and initial diffraction angle $2\theta_{ini} = 10^{o}, 20^{o}, 20^{o}$ respectively, as schematically stated by Figure 4.5a-c.

All the diffraction patterns of the enameloid were compared with the standard pattern of HAp (International Centre of Diffraction Data, Powder Diffraction File, No: 84-1998). Figure 4.5d shows the diffraction patterns of three XRD tests on a bulk enameloid sample compared to that of the powder sample obtained from the bulk enameloid by grinding. As expected, all patterns show the characteristic XRD spectrum of hydroxyapatite (HAp), assuring that HAp is the major composition of enameloid. However, the relative intensities of the spectrum differ among the patterns. In view of the hexagonal close packed (HCP) crystallographic structure of HAp in which *c*-axis is perpendicular to the (002) planes, the XRD results indicate that a significant portion of HAp crystallites near the OS have *c*-axises normal to the OS. The *c*-axis preferential orientation of the HAp near the enameloid surface is thus

proved.

4.3 The wear resistance of the single crystal hydroxyapatite

After knowing the superior wear resistance of the OS of black carp teeth as well as the *c*-axis preferential orientation of the HAp crystallites near the OS, seeking the possible correlation between them becomes the objective. To achieve the purpose, molecular dynamics (MD) simulation was used to investigate the response of single crystal HAp to scratching at atomic length scale (see Chapter 3. Research methods for details of the force field setting). Figure 4.6a shows the MD simulation model, in which a rigid pyramidal probe is initially compressed on a single crystal HAp to depth D_p = 2 nm and then displaced horizontally at a constant speed and constant attack angle α (angle between the scratching surface of the probe and the horizontal plane). To quantify the extent of wear, the amount of debris was computed by counting the number of Ca atoms scratched away from the scratch surface [110-117]. A Ca atom is counted as debris if its displacement exceeds a critical value of 1.0 nm, which is roughly the HAp lattice constant or the cutoff distance of the force field [110-114]. The scratching simulation were conducted on four representative surfaces of a single crystal HAp respectively including (001), (010), (110), and $(1\bar{1}0)$ surfaces with attack angle α varying from 15º to 55º. The (001) surface is parallel to the OS, the other three surfaces are of interest because these surfaces are perpendicular to (001) and thus may be assumed as the LS. Due to the structural symmetry of HAp crystal, the (100) surface

is the same as the (010) surface and therefore is not considered individually [90, 91, 118]. For each surface, scratching probe moved along three typical directions.

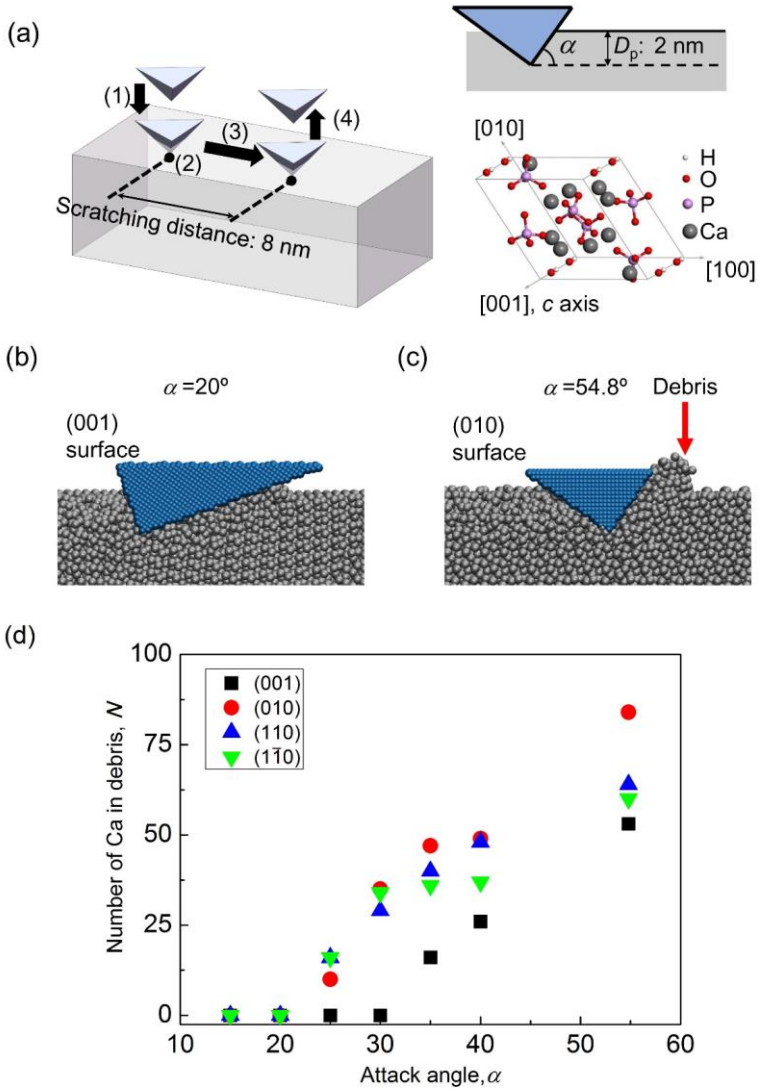

Figure 4.6. (a) Schematics of the MD simulation model and unit cell of HAp crystal. The nano-scratching simulation is implemented through four steps: (1) the rigid probe engages with the surface by penetrating to depth D_p; (2) the probe holds still for 20 ps for relaxation; (3) the probe is displaced horizontally to scratch the surface by 8 nm with D_p kept constant, and (4) the probe is withdrawn from the surface. (b-c) Snapshots of scratching on (001) and (010) surfaces at the end of step (3) with corresponding attack angle α being 20° and 54.8° respectively. Here only the Ca atoms in HAp are shown for a clearer visualization. (d) Variations of the amount of debris characterized by the number of Ca atoms scratched away from the bulk HAp as a function of attack angle α.

The simulation results showed that the failure behavior of HAp single crystal under scratching depends on the attack angle α. Surfaces under scratching exhibit 'rubbing mode' failure (Figure 4.6b) at smaller attack angle, while 'cutting mode' failure occurs (Figure 4.6c) at lager attack angle. There exists a critical attack angle, α_c, above which debris is produced or 'cutting mode' dominates. Figure 4.6d shows the variation of the amount of debris as a function of attack angle. It can be found that α_c is around 30º for the (001) surface, while for the other three surfaces it is around 20º. Considering the fact that the black carp teeth in service may experience wear caused by particles with different angles, larger α_c of the (001) surface implies that the (001) surface has a higher probability to give rise to 'rubbing mode' failure under wear with random attack angles. This may also explain why in the above scratching experiments shown in Figure 4.4 'rubbing' mode was observed on the OS while 'cutting' mode on LS. On the other hand, from the perspective of wear, 'cutting mode' failure is more destructive than the 'rubbing mode' one as it includes the removal of material in addition to the plastic deformation. It can be observed from Figure 4.6d that the amount of debris produced on (001) surface of HAp is always less than those on the other surfaces at the same attack angle, implying the higher wear resistance of the (001) surface. Recalling the *c*-axis preferential orientation of the HAp crystallites near the OS as observed above, the superior wear resistance of the teeth can be attributed to the *c*-axis preferential orientation of the HAp crystallites near the OS.

4.4 The mechanism of the superior wear resistance of the teeth occlusal surface

To gain a deeper understanding of the wear behavior of the surface under scratching, theoretical analysis was carried out. From the consumed energy perspective, material under scratching tends to assume failure mode requiring less energy. To predict the failure mode of surface under scratching, the laterally pushing force F for 'rubbing mode' and 'cutting mode' should be compared. Actually, related results have been obtained especially for scratching with pyramidal probe [119-127]. In the following theoretical analysis, 'pile-up' or 'sink-in' phenomenon on the surface is neglected, and interaction between probe and scratched material is assumed frictionless and non-adhesive. So that the contact area between probe and scratched material the can be determined from the penetration depth D_p and the attack angle α.

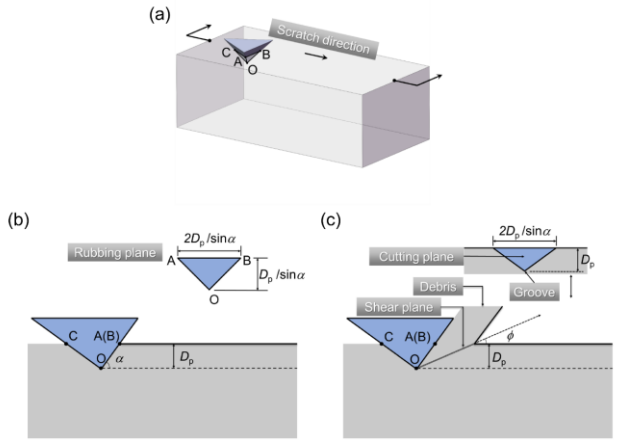

Figure 4.7. (a) 3D view of schematics of theoretical model. (b) Cross section of 'rubbing mode' and (c) 'cutting mode'.

According to Bowden and Tabor's theory [125], the laterally pushing force in 'rubbing mode' (as shown in Figure 4.7b) F^{rub} was obtained for the pyramidal probe having inclined face in contact with the material during scratching by Sedriks and Mulhearn, [126]

$$F^{\text{rub}} = \tau_{\text{y}} \cdot A^{\text{rub}} \cos\alpha + H \cdot A^{\text{rub}} \sin\alpha , \tag{4.1}$$

where τ_{y} is the shear strength of the scratched material, H is the indentation hardness, α is the attack angle, and A^{rub} is the actual contact area between the substrate material and the inclined face of the probe. In the model using the cube-corner probe, we have

$$A^{\text{rub}} = \frac{c \cdot D_{\text{p}}^{\ 2}}{\sin^2 \alpha} , \tag{4.2}$$

where c =2 based on Sedriks and Mulhearn's analysis [126, 127]. Combination of Eq. (4.1) and (4.2) gives rise to

$$F^{\text{rub}} = \tau_{\text{y}} \cdot \frac{2D_{\text{p}}^2}{\sin^2 \alpha} \cdot \cos\alpha + H \cdot \frac{2D_{\text{p}}^2}{\sin^2 \alpha} \cdot \sin\alpha . \tag{4.3}$$

For 'cutting mode', Atkins *et al.* established a model (as shown in Figure 4.7c) [127] , based on which the laterally driving force F^{cut} can be given by

$$F^{\text{cut}} = \tau_{\text{y}} \cdot \gamma \cdot A^{\text{cut}} + \gamma_{\text{s}} \cdot A^{\text{new}} , \tag{4.4}$$

where γ_{s} is the surface energy and γ is the shear strain of the debris peeled off. The shear strain γ is associated with the inclined angle ϕ of shear plane and attack angle α

through [127]

$$\gamma = \sin\alpha / \sin(\alpha - \phi)\sin\phi . \tag{4.5}$$

In Eq. (4.5), the inclined angle is determined to be $\phi = \frac{\alpha}{2}$ based on the assumption that the debris happens along the direction requiring the least energy or minimum γ. The cutting plane is the cross-section of the groove, which is normal to the scratch direction, and the area of the cutting plane can be expressed as

$$A^{\text{cut}} = D_{\text{p}}^{\,2} \Big/ \sin\alpha . \tag{4.6}$$

The area of the new created surface per unit scratching distance can be approximated by

$$A^{\text{new}} \approx 4D_{\text{p}} \cdot \sqrt{1+\sin^2\alpha} \Big/ \sin\alpha . \tag{4.7}$$

So the expression of the laterally driving force for 'cutting mode', F^{cut}, can be written as

$$F^{\text{cut}} = \tau_{\text{y}} \cdot \frac{2D_{\text{p}}^{\,2}}{1-\cos\alpha} + \gamma_{\text{s}} \cdot \frac{4D_{\text{p}}\sqrt{1+\sin^2\alpha}}{\sin\alpha} . \tag{4.8}$$

From the energy point of view, material under scratching tends to assume failure mode requiring less energy or more energetically preferable. For a constant-speed scratching on a generic solid surface, the energy required for unit scratching distance equals the laterally driving force *F* applied on the probe,

$$F^{\text{rub}} = \tau_{\text{y}} \cdot \frac{2D_{\text{p}}^{\ 2}}{\sin^2 \alpha} \cdot \cos\alpha + H \cdot \frac{2D_{\text{p}}^{\ 2}}{\sin^2 \alpha} \cdot \sin\alpha, \tag{4.3}$$

$$F^{\text{cut}} = \tau_{\text{y}} \cdot \frac{2D_{\text{p}}^{\ 2}}{1-\cos\alpha} + \gamma_{\text{s}} \cdot \frac{4D_{\text{p}}\sqrt{1+\sin^2\alpha}}{\sin\alpha}, \tag{4.8}$$

for 'rubbing mode' and 'cutting mode' failure, respectively. In Eq. (4.3) and (4.8), τ_{y}, H and γ_{s} are the shear strength, hardness and surface energy of the scratched material respectively; α is the attack angle and D_{p} is the penetration depth. Although Eq. (4.3) and (4.8) were developed for isotropic solids [125, 126], we assume they also apply to anisotropic materials as long as the mechanical properties (H, τ_{y} and γ_{s}) are taken as the effective values obtained from the surfaces under scratching. The failure mode under scratching is determined by the competition between F^{rub} and F^{cut}. If $F^{\text{rub}} < F^{\text{cut}}$, 'rubbing mode' happens; otherwise, 'cutting mode' takes place. At the critical attack angle, α_{c}, we have $F^{\text{rub}} = F^{\text{cut}}$, which implies

$$\frac{H}{\tau_{\text{y}}} = \frac{\sin\alpha_{\text{c}}}{1-\cos\alpha_{\text{c}}} + \frac{2\gamma_{\text{s}}}{\tau_{\text{y}} \cdot D_{\text{p}}}\sqrt{1+\sin^2\alpha_{\text{c}}} - \cot\alpha_{\text{c}}, \tag{4.9}$$

Eq. (4.9) implicitly defines the critical attack angle, α_{c}, as a function of two dimensionless parameters $\frac{\gamma_{\text{s}}}{\tau_{\text{y}} D_{\text{p}}}$ and $\frac{H}{\tau_{\text{y}}}$.

MD simulations were carried out to determine the mechanical properties of HAp using the same force field as in the scratching simulation.

Determination of shear strength τ_y. To estimate the shear strengths of the HAp between (001) planes, (010) planes, (110) planes, and $(1\bar{1}0)$ planes along the [100] direction, [100] direction, $[1\bar{1}0]$ direction and [110] direction, respectively, two-dimensional shear simulations were carried out. As shown in Figure 4.8a, the height of each sample is roughly 4 nm. In the simulations, shear strain was applied by changing the tilting angle β of sample at the strain rate of $10^{10}s^{-1}$. The shear stress-strain curves are shown in Figure 4.8 (b-e), from which the shear strengths (the peak stresses on the curves), for (001), (010), (110), and $(1\bar{1}0)$ are obtained (Table 4.1).

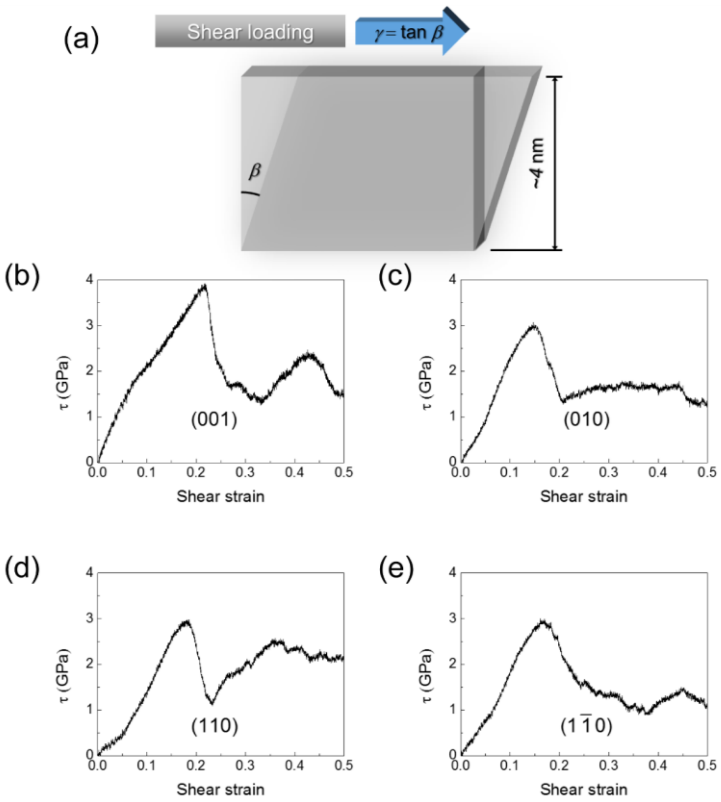

Figure 4.8. Simple shear simulations. (a) Schematics of the simulations model for shear tests. (b-e) Stress–strain curves of the shear tests.

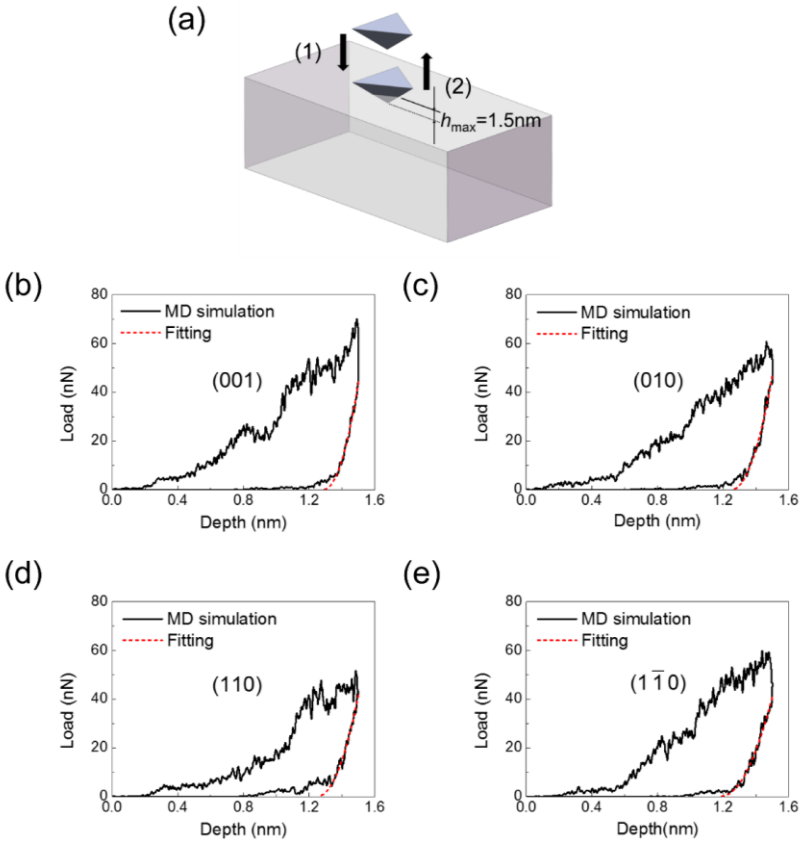

Figure 4.9. Nanoindentation simulations used to predict the mechanical properties of HAp on different orientations. (a) Schematics of the simulations model for indentation tests which are implemented through two consecutive steps: (1) the rigid probe engages with the HAp single crystal with indentation depth h =1.5 nm; (2) the probe is withdrawn from the HAp sample. (b-e) Load-depth curves of the indentation simulation obtained on different surfaces, from which the mechanical properties of the related surface can be deduced.

Determination of hardness *H*. To determine the hardness of HAp crystal on the (001), (010), (110) and (1$\bar{1}$0) surfaces, virtual nanoindentation tests were carried out using MD simulation. In each set of the simulations, the HAp sample has more than 60 unit cells in all three dimensions to eliminate edge effect, and the atoms at the bottom surface are fixed in all dimensions. As shown in Figure 4.9a**,** a cube-corner indenter

was applied with the maximum indentation depth h_{max} = 1.5 nm. The load-depth curves are shown in Figure 4.9 (b-e), where dashed lines represent the fitting curves of the unloading portions to be used to determine the hardness H and the reduced modulus E_r using Oliver-Pharr (O-P) model [121]. The calculated results are shown in Table 4.1, which is in consistence with those measured by experiments [128, 129].

Determination of surface energy γ_s. Surface energy of HAp refers to the energy associated with the creation of new surface of unit area. It can be obtained by calculating the change of total potential energy as the HAp is split into two pieces (the schematics of the simulation procedures is shown in Figure 4.10). That is, surface energy $\gamma_s = (E_f - E_i)/A$, where E_f and E_i refer to the total potential energies of the system after and before the fracture, and A stands for the area of newly created surfaces which equals double of the fractured surface area. The calculated surface energies for (001), (010), (110), and $(1\bar{1}0)$ planes are listed in Table 4.1, which agree with the values reported in literature [130-132].

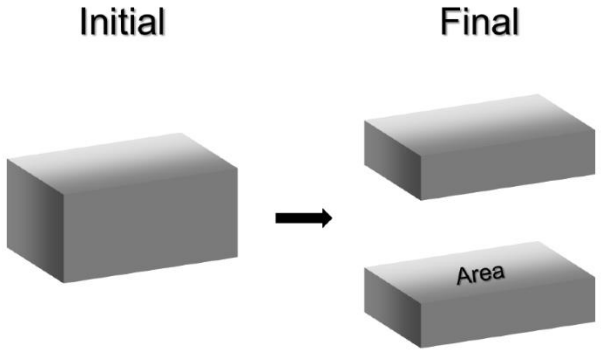

Figure 4.10. Schematics of the simulations model for determination of surface energy.

Table 4.1. The mechanical properties of HAp calculated from (001), (010), (110), and $(1\bar{1}0)$ planes in comparison with the values reported in literature.

Planes	τ_y (GPa)	H (GPa)	E_r (GPa)	γ_s (J/m^2)
(001)	3.92	8.84 (7.06[167, 168])	160.9 (142.92[167, 168])	1.32 (1.345[169],1.692[170],1.043[129])
(010)	3.08	8.38 (6.41[167, 168])	151.2 (137.98[167, 168])	1.20 (1.692[170],1.709[129])
(110)	2.92	8.51	127.4	1.33 (1.692[170])
$(1\bar{1}0)$	3.02	8.18	103.8	1.34 (1.692[170])

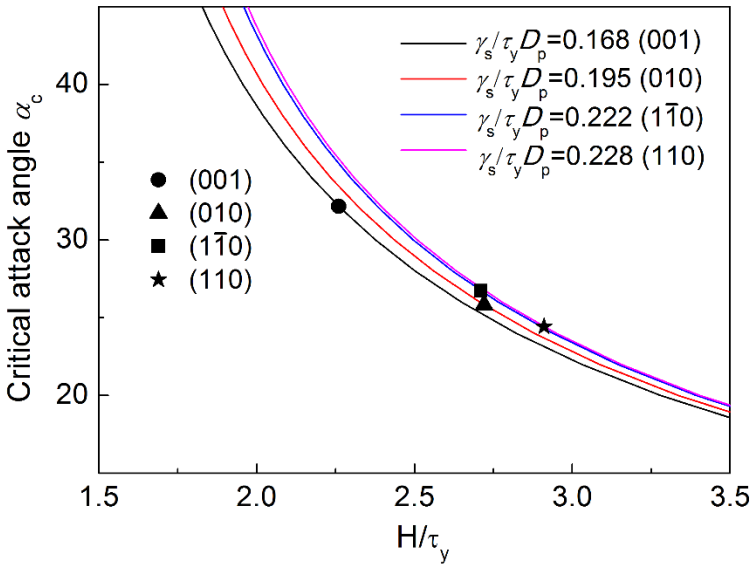

Figure 4.11. Dependence of α_c on H/τ_y for given $\gamma_s/\tau_y D_p$.

Taking penetration depth D_p = 2 nm, the critical attack angle for surfaces of (001), (010), (110), and $(1\bar{1}0)$ of single crystal HAp can be determined graphically based on their respective effective H, τ_y and γ_s (Table 4.2) calculated by MD simulation. As shown by Figure 4.11, $\alpha_c \approx 25^\circ$ for (010), (110) and $(1\bar{1}0)$, while $\alpha_c \approx 33^\circ$ for (001), agreeing well with the MD simulation results shown in Figure 4.6d. The

relatively higher α_c for (001), according to Figure 4.11, is mainly due to its relatively lower ratio of H/τ_y.

It should be pointed out that the MD simulation as well as above theoretical analysis implies that 'rubbing mode' failure can also be produced on the surfaces other than OS, which has not been observed in the earlier scratching experiment with Berkovich probe. I therefore repeated the scratching tests using a blunt conical probe so as to achieve a much smaller attack angle. As expected, 'rubbing mode' failure was observed not only on OS but also on LS.

Table 4.2. The values of H/τ_y and $\gamma_s/\tau_y D_p$ calculated from the (001), (010), (110), and (1$\bar{1}$0) planes of single crystal HAp. D_p is taken as 2 nm.

Planes	H/τ_y	$\gamma_s/\tau_y D_p$
(001)	2.26	0.168
(010)	2.72	0.195
(110)	2.91	0.228
(1$\bar{1}$0)	2.71	0.222

4.5 Summary

In summary, inspired by the outstanding wear resistance exhibited by the OS of black carp teeth, a comparative XRD analysis were carried out on its enameloid and the *c*-axis preferential orientation of the building HAp crystallites near the OS was uncovered. MD simulation of scratching on single crystal HAp demonstrated that the (001) surface exhibits better wear resistance compared to other surfaces. Therefore,

the dependence of the outstanding wear resistance of black carp teeth on the *c*-axis preferential orientation of HAp was confirmed. To further reveal the mechanics accounting for the orientation-dependent wear resistance of HAp crystal, theoretical analysis was performed. It was revealed that scratching on the (001) surface of HAp tends to cause plastic deformation ('rubbing mode' failure) rather than removal of materials ('cutting mode' failure) because for (001) surface 'rubbing mode' failure is more preferable in energy than 'cutting mode' failure when the attack angle α is smaller than a critical value α_c. Similar dependence of mechanical properties on materials' structure and texture have also been reported in the other natural materials such as bones [132-134], human teeth [84, 85], teeth of sea urchin [135], and bamboo [136]. The finding of the work shows great promise of applying preferential orientation of crystals to increase the wear resistance of materials.

Chapter 5. Superior anti-fouling performance of the morphology of mangrove leaves

Marine biofouling refers to the accumulation of bio-fouler on submerged surfaces in ocean [71, 137-139]. It not only affects the appearance of the surfaces but also induces a lot of substantial impairments to marine industry. Traditional methods to treating marine biofouling mainly utilized paints incorporated with inorganic and organometallic biocides (*e.g.*, copper compounds and tributyltin (TBT) compounds) [140]. However, many biocides have severe negative impacts on environment. To lower and avoid the negative impact, organic biocides with lower toxicity were used [141]. Developing anti-fouling methods with less environmental impact is invariably in need.

In nature, many organisms have evolved surfaces with excellent anti-fouling performance. Inspired by these natural anti-fouling surfaces [142, 143], researchers have devoted themselves to the development of biomimetic chemical antifoulants such as enzymes [144] and metabolites isolated from marine microorganisms [145]. In this chapter, mangrove tree of *Sonneratia apetala* (see Figure 5.1a) attracted our attention for its unique leaves. As an intertidal plant, *S. apetala* is subject to marine fouling. Interestingly, the leaves of *S. apetala*, compared to its twigs and barks, are almost immune to biofouling. Proposed mechanisms accounting for such excellent anti-

fouling property include low surface wettability, antifoulant of oleanolic acid and post-settlement detachment. However, these may not be the most dominant mechanism because leaves of other mangrove species also share these mechanisms but exhibit much worse anti-fouling performance [146].

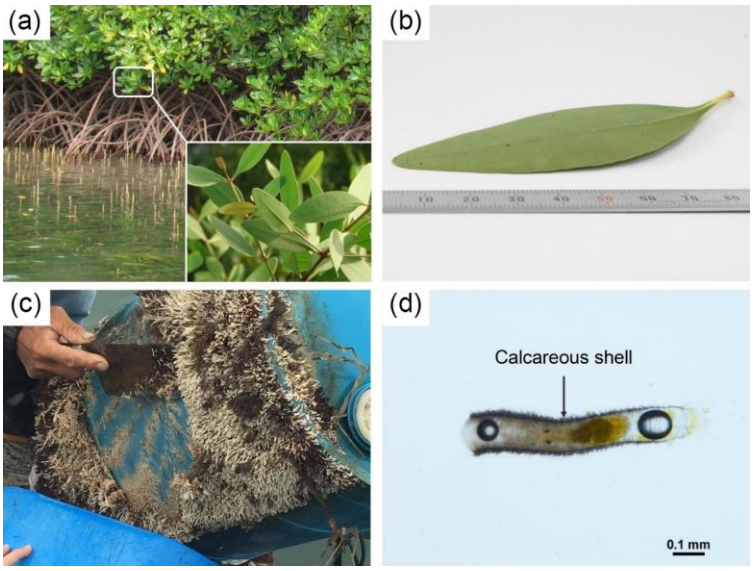

Figure 5.1. The anti-fouling leaves of *S. apetala* and bio-fouler tubeworm *H. elegans*. (a) *S. apetala* living in intertidal zone. (b) a leaf of *S. apetala*. (c) adult tubeworms *H. elegans* accumulated on a plastic bucket. (d) a larva of *H. elegans* with calcareous shell attached on a glass slide.

Here, we propose surface morphology as the dominant mechanism for the extraordinary anti-fouling performance of *S. apetala* leaves. To verify this hypothesis, a polymeric replica that duplicates the surface morphology of a *S. apetala* leaf was firstly prepared [147-149]. The anti-fouling performance of the replica is verified by attachment test with tubeworm larvae [150, 151]. To gain deeper insights into the effects of surface morphology on anti-fouling performance, theoretical modeling is

built, giving rise to guidelines for achieving better anti-fouling performance through morphology optimization. Finally, a synthesized biomimetic surface with ridge-like morphology is tested, showing comparable anti-fouling performance to that of the *S. apetala* leaves.

5.1 Superior anti-fouling performance of *Sonneratia apetala* leaves

To investigate the effect of surface morphology on anti-fouling performance and meanwhile mask other possible factors such as biocides from the leave, PDMS replicas of *S. apetala* leaves are prepared by a molding process as illustrated by Figure 5.2a (see Chapter 3. Research methods for detailed description). Figure 5.2b-g show the surface morphology of a PDMS replica in comparison to that of the *S. apetala* leaf. Obviously, the PDMS replica faithfully duplicates the ridge-like morphology of the leaf. The height and thickness of the ridges are around 5 μm and 1 μm while the inter-ridge spacing is around 5 μm. Moreover, flat PDMS surfaces are also prepared as the control group for anti-fouling performance test.

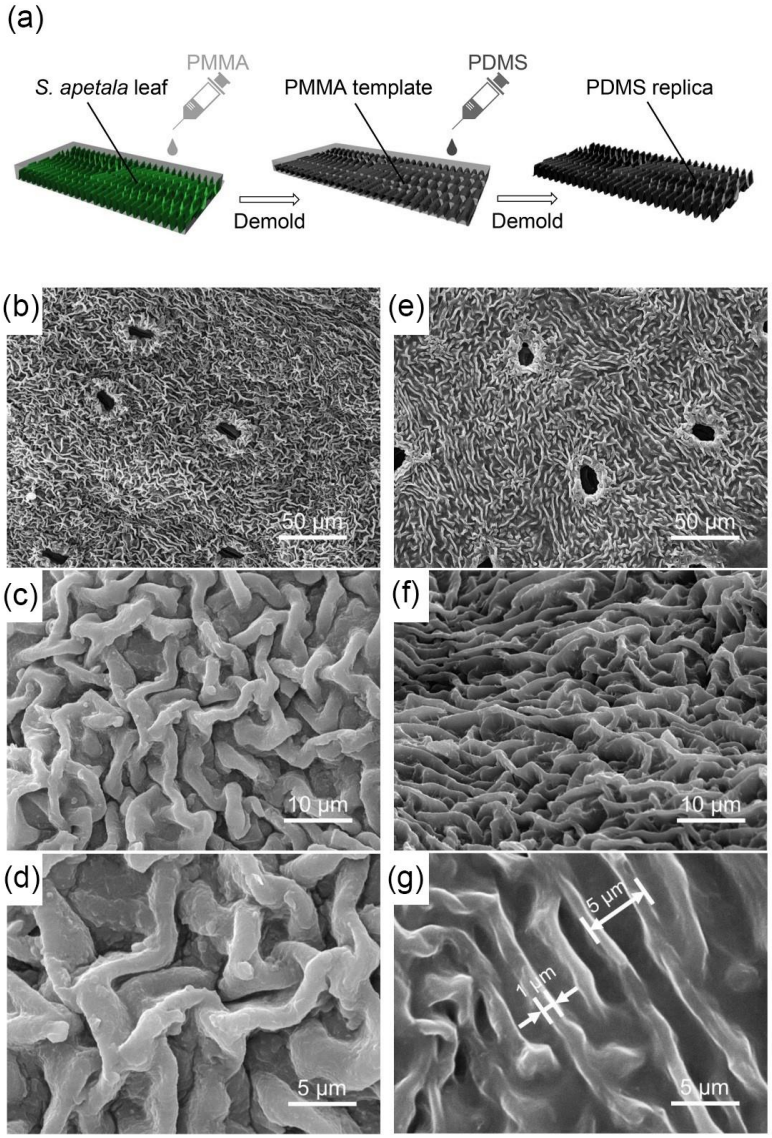

Figure 5.2. (a) The molding process for preparing PDMS replica of *S. apetala* leaves. (b-d) SEM images of a leaf surface of *S. apetala* morphology compared to (e-g) those of its replica morphology.

To evaluate the anti-fouling performance of the PDMS replicas of the *S. apetala* leaves, settlement tests of tubeworms are carried out with flat PDMS samples and glass slides used as the control group (see Chapter 3. Research methods for details). Figure 5.3 shows the numbers of settled tubeworms on different surfaces after 24 h and 48 h immersion.

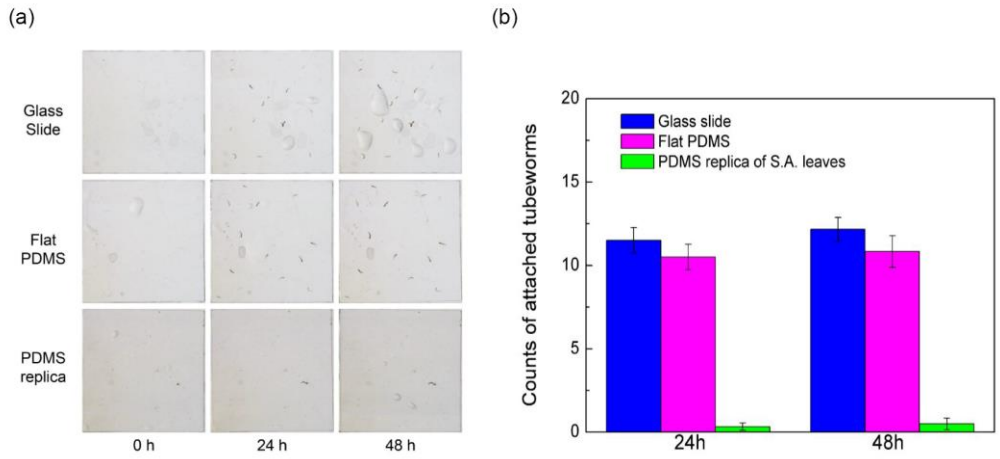

Figure 5.3. Anti-fouling performance evaluation. (a) Attachment of tubeworm larvae on glass slide, flat PDMS surface and PDMS replica of a *S. apetala* leaf after 0 h, 24 h and 48 h immersion. (b) Means ±SE (n = 6) of total counts of tubeworms attached on these surfaces after 24 h and 48 h.

It can be seen that little change happens in the number of attached tubeworm larvae during the period from 24 h to 48 h, implying that the settlement of larvae mainly takes place during the first 24 h. The number of tubeworms attached on the PDMS replicas after 24 h immersion is less than 5% of those on the flat PDMS surfaces and glass slides. Moreover, the difference in the numbers of attached tubeworms between the flat PDMS surfaces and glass slides is not significant, implying that surface morphology rather than material properties, such as chemistry and hardness, plays the dominant role in determining the settlement of tubeworms. This finding evokes an earlier similar study on the attachment of various fouling species on surfaces with microgrooves of different sizes [75]. It was found that the settlement of tubeworms on a textured surface is sensitive to the characteristic length scale of the texture. For a

given texture, there is an optimal characteristic length that can prohibit the settlement of tubeworms to the best extent. Questions are raised, for the ridge-like surface morphology of *S. apetala* leaves, does the settlement of the larvae depend on its characteristic sizes? Are there any optimal characteristic lengths leading to better anti-fouling performance? To answer these questions, theoretical modeling is built to investigate the adhesion between a tubeworm and a surface with ridge-like morphology.

5.2 Theoretical modeling of anti-fouling mechanism

The effect of surface morphology on biofouling has long been recognized and studied [74, 75, 152-154]. To shed light on the size dependence of the anti-fouling performance of the ridge-like morphology, a quantitative model with physical basis, rigorous formulation and prediction competence is built.

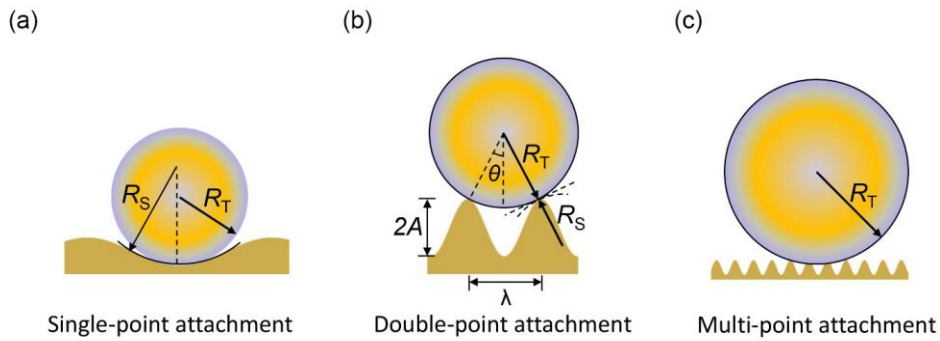

Figure 5.4. Schematics of three possible attachment configurations of a tubeworm attached on substrate with wavy profile: (a) single-point attachment, (b) double-point attachment and (c) multi-point attachment.

For a tubeworm larva, I assume that the success rate of attachment on a textured surface depends on the maximum adhesion force that can be achieved between them. To quantify the adhesive force between a tubeworm and a textured surface shown in Figure 5.2b, a mechanics model is established. Given the cylindrical shape of tubeworms and the ridge-like surface morphology of the *S. apetala* leaves, here I consider an adhesive contact problem between a 2D (plane strain) cylinder and a substrate with wavy profile (see Figure 5.4). Even though the fouling attachment involves complex chemical and biological processes, this simplified model is believed capable of capturing the mechanical essentials of fouling attachment.

Prior to solving the posed problem, it is worthwhile to introduce a useful result concerning the adhesion between an elastic cylinder and a flat substrate. Earlier studies indicated that the pull-off force between a cylinder (plane strain) and a flat substrate, which refers to the force required to separate them, is given by [155]

$$F_{\mathrm{pf}}^{\mathrm{Flat}} = 3\left(\frac{\pi E^{*} W^{2} R_{\mathrm{T}}}{16}\right)^{1/3}, \tag{5.1}$$

with $E^{*} = 1/\left[\left(1-\nu_{\mathrm{T}}^{2}\right)/E_{\mathrm{T}} + \left(1-\nu_{\mathrm{S}}^{2}\right)/E_{\mathrm{S}}\right]$, where E_{T}, E_{S}, ν_{T}, ν_{S} denote the elastic moduli and Poisson's ratios of the cylinder and the substrate respectively, R_{T} stands for the cross-sectional radius of the cylinder, and W represents the adhesion energy between the cylinder and substrate.

For a substrate with wavy profile, I assume that the profile is periodic and can be described by a trigonometric function $y = -A\cos\left(\frac{2\pi x}{\lambda}\right)$, where λ and A denote the wavelength and amplitude, two characteristic length scales of the profile, respectively. There are three distinct attachment configurations, depending on the characteristic length scales of the profile, as shown in Figure 5.4a-c. If the wavelength of the profile λ is much larger than the tubeworm's radius R_T, the tubeworm rest at the trough of the groove, as shown in Figure 5.4a. This configuration is called as single-point attachment. For profile with smaller λ, the tubeworm has to straddle over a groove between two adjacent ridges, forming a configuration called double-point attachment (see Figure 5.4b). If λ is much smaller than the size of the tubeworm, more than two contact points will form between the tubeworm and the substrate, giving rise to a multi-point attachment configuration, as shown in figure Figure 5.4c.

Pull-off force of single-point attachment configuration

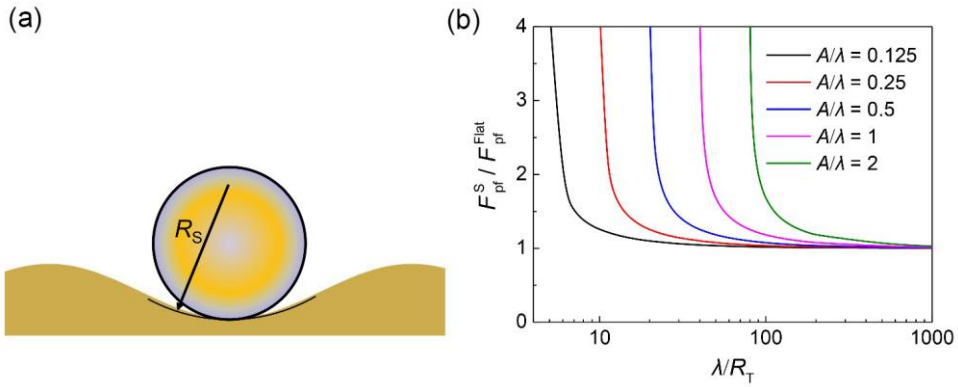

Figure 5.5. (a) Schematic of single-point attachment configuration. (b) Variation of the pull-off

force with λ/R_T for single-point attachment configuration with various A/λ .

For single-point attachment configuration, the cylinder rests on the trough region, as shown in Figure 5.5a, there is only one contact point between the cylinder and the substrate. Earlier studies indicated that the pull-off force to separate two cylindrical bodies is given by [155]

$$F_{pf}^{S} = 3\left(\frac{\pi E^{*} W^{2} R}{16}\right)^{1/3}, \tag{5.2}$$

where $R = \frac{R_S R_T}{R_S + R_T}$, $E^{*} = 1\Big/\left[\left(1-\nu_T^2\right)\Big/E_T + \left(1-\nu_S^2\right)\Big/E_S\right]$ and W is the work of adhesion. Combination of Eq. (5.1) and (5.2) gives rise to

$$F_{pf}^{S} = \left(\frac{R_S}{R_S + R_T}\right)^{1/3} F_{pf}^{Flat}. \tag{5.3}$$

Here, R_T and R_S stand for the radius of curvature of the tubeworm and substrate at the contact point respectively. For a profile defined by function $y = -A\cos\left(\frac{2\pi x}{\lambda}\right)$, the radius of curvature at the trough R_S can be calculated by $R_S = -\frac{\left(1+y'(0)^2\right)^{3/2}}{y''(0)}$, where $y'(0)$ and $y''(0)$ stand for the first and second derivatives of function y(x) at x=0. Thus, R_S is given by

$$R_S = -\frac{\lambda^2}{4\pi^2 A}. \tag{5.4}$$

By inserting equation Eq. (5.4) into (5.3), the normalized pull-off force for single-point attachment configuration, F_{pf}^{S}/F_{pf}^{Flat}, can be given as a function of λ/R_T for a given A/λ. The dependence of F_{pf}^{S}/F_{pf}^{Flat} on λ/R_T for different A/λ is shown in Figure 5.5b. From Eq. (5.3) and Figure 5.5b, it can be noticed that F_{pf}^{S} goes to infinity when $R_S = -R_T$. Such unrealistic singularity of the predicted pull-off force is essentially attributed to the conventional parabolic approximation for circular profiles in contact mechanics [155], because when $R_S = -R_T$, this result actually describes the pull-off force between a concave surface and a conformal solid with exactly the same parabolic-shaped profile. To overcome this dilemma, we have to estimate an upper limit for F_{pf}^{S}.

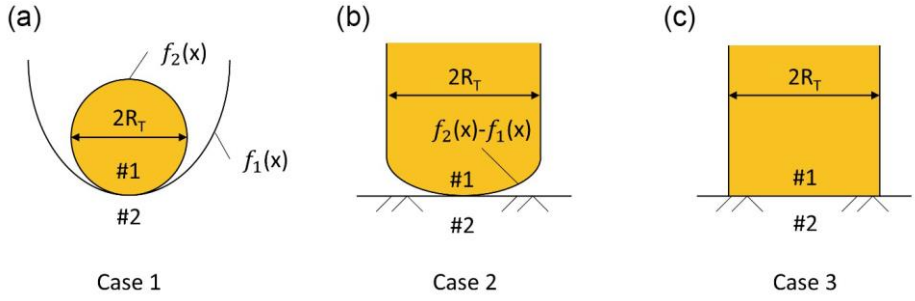

Figure 5.6. (a) Contact between two solids with profile functions $f_1(x)$ and $f_2(x)$. (b) Contact between a solid with profile function $f_2(x) - f_1(x)$ and a flat substrate. (c) Contact between a solid a solid with flat profile and a flat substrate.

For adhesive contact case between two solid materials with profile functions $f_1(x)$ and $f_2(x)$ (see Figure 5.6a), it can be demonstrated in contact mechanics that the pull-off

force in-between is equal to that of an equivalent case in which one material has profile function $f_2(x)-f_1(x)$ while the other is totally flat (see Figure 5.6b). Meanwhile, it can be demonstrated that such pull-off force reaches its maximum when the profile is flat (see Figure 5.6c), namely $f_2(x)-f_1(x)=0$. This cap value is given by

$$F_{\mathrm{pf}}^{\mathrm{Cap}}=\sqrt{2\pi E^{*}WR_{\mathrm{T}}}\,, \tag{5.5}$$

which can be further expressed in terms of $F_{\mathrm{pf}}^{\mathrm{Flat}}$ as

$$F_{\mathrm{pf}}^{\mathrm{Cap}}=1.19\left(\frac{\pi E^{*}R_{\mathrm{T}}}{W}\right)^{1/6}F_{\mathrm{pf}}^{\mathrm{Flat}}\,. \tag{5.6}$$

Pull-off force of double-point attachment configuration

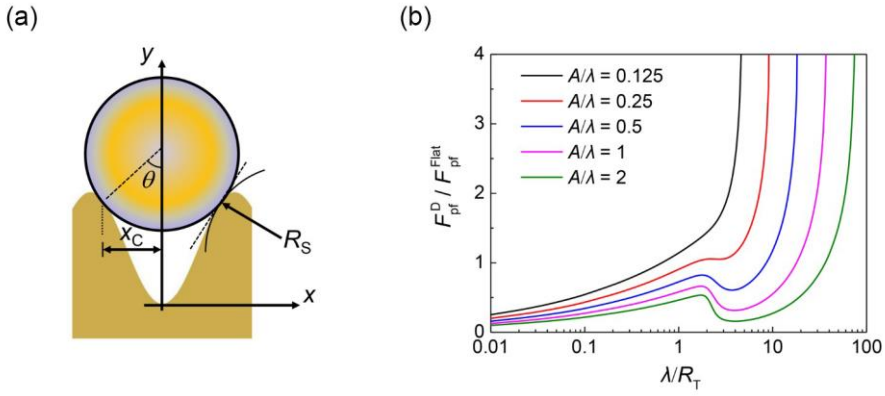

Figure 5.7. (a) Schematic of double-point attachment configuration. (b) Variation of the pull-off force with λ/R_{T} for double-point attachment configuration with various A/λ.

For double-point attachment configuration, the cylinder straddles over a groove between two adjacent ridges. The pull-off force equals the resultant force of the adhesion on both contact points

$$F_{\mathrm{pf}}^{\mathrm{D}} = 2\cos\theta \cdot F_{\mathrm{pf}}^{\mathrm{ridge}}, \tag{5.7}$$

where $F_{\mathrm{pf}}^{\mathrm{ridge}}$ is the pull-off force on one ridge, and θ is the contact angle designated in Figure 5.7a.

For the adhesion with a single ridge, the pull-off force can be written as

$$F_{\mathrm{pf}}^{\mathrm{ridge}} = \left(\frac{R_{\mathrm{S}}}{R_{\mathrm{S}} + R_{\mathrm{T}}} \right)^{1/3} F_{\mathrm{pf}}^{\mathrm{Flat}}, \tag{5.8}$$

where R_{S} is the curvature radius at the contact point of the substrate.

Combining Eq. (5.7) and (5.8), $F_{\mathrm{pf}}^{\mathrm{D}}$ can be rewritten as,

$$F_{\mathrm{pf}}^{\mathrm{D}} = 2\cos\theta \cdot \left(\frac{R_{\mathrm{S}}}{R_{\mathrm{S}} + R_{\mathrm{T}}} \right)^{1/3} F_{\mathrm{pf}}^{\mathrm{Flat}}, \tag{5.9}$$

The radius of curvature at the contact point R_{S} can be calculated from the profile function $y(x)$ through

$$R_{\mathrm{S}} = -\frac{\left(1 + y'^{2}\right)^{3/2}}{y''}, \tag{5.10}$$

where the first and second derivatives of the profile function are given by $y' = A \cdot (2\pi/\lambda) \cdot \sin(2\pi x_{\mathrm{C}}/\lambda)$ and $y'' = A \cdot (2\pi/\lambda)^2 \cdot \cos(2\pi x_{\mathrm{C}}/\lambda)$, respectively. In above expressions, x_{C} represents the coordinate of the contact point in the x direction (see Figure 5.7a), which can be determined from following geometrical relationship

$$\frac{x_{\mathrm{C}}}{\sqrt{R_{\mathrm{T}}^{\,2} - x_{\mathrm{C}}^{\,2}}} = 2\pi \cdot \left(\frac{A}{\lambda} \right) \cdot \sin\left(\frac{2\pi x_{\mathrm{C}}}{\lambda} \right), \tag{5.11}$$

Therefore, for given A/λ, it can be seen from Eq. (5.11) that normalized coordinate x_C / R_T is a function of λ/R_T.

As to the contact angel θ, basic geometric relationship implies that

$$\cos\theta = \sqrt{1-\left(x_C/R_T\right)^2}, \tag{5.12}$$

Eq. (5.12) indicates that for given A/λ, $\cos\theta$ is a function of λ/R_T. Therefore, F_{pf}^{D}/F_{pf}^{Flat} according to Eq. (5.9) should be a function of λ/R_T for given A/λ. Figure 5.7b shows the variation of F_{pf}^{D}/F_{pf}^{Flat} with λ/R_T for different A/λ. As λ/R_T increases, F_{pf}^{D} will approach to F_{pf}^{S} which has singularity when $R_T = -R_S$ or $\lambda/R_T = 4\pi^2 A/\lambda$. This singularity problem has been well addressed above by introducing a reasonable cap for the pull-off force when $R_S = -R_T$.

Pull-off force of multi-point attachment configuration

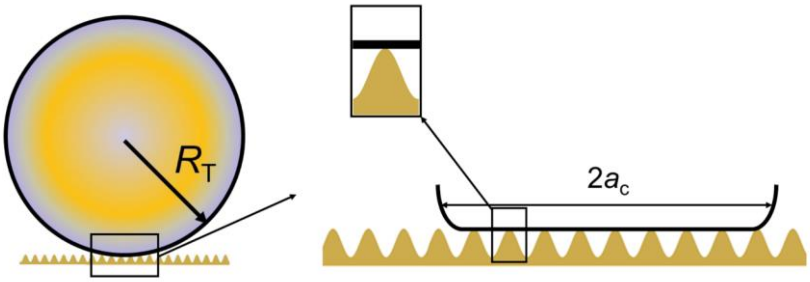

Figure 5.8. Schematic of multi-point attachment configuration.

With the decrease of the λ, more than two ridges will contact the cylinder, as shown in Figure 5.8. To simplify the problem, the contact at each ridge is assumed identical. Thus, for this multi-point attachment configuration, the pull-off force F_{pf}^{M} can be

roughly estimated as

$$F_{\mathrm{pf}}^{\mathrm{M}} = N \cdot F_{\mathrm{pf}}^{\mathrm{ridge}}, \tag{5.13}$$

where N is the number of the ridges in contact with the cylinder, and $F_{\mathrm{pf}}^{\mathrm{ridge}}$ is the pull-off force contributed by one ridge. The number of the ridges N can be estimated from the expression

$$N = \frac{2a_{\mathrm{c}}}{\lambda}, \tag{5.14}$$

where $2a_{\mathrm{c}}$ is the nominal contact width between the cylinder and the substrate at the pull-off moment, as shown in Figure 5.8, which can be given by

$$2a_{\mathrm{c}} = 2 \cdot \left(\frac{2W_{\mathrm{equ}} {R_{\mathrm{T}}}^2}{\pi E^*} \right)^{1/3}, \tag{5.15}$$

where W_{equ} is the equivalent adhesion energy between the cylinder and wavy substrate given by

$$W_{\mathrm{equ}} = \frac{2a_{\mathrm{each}}}{\lambda} \cdot W = \left(\frac{W^4 \lambda}{\pi^5 E^{*} A^2} \right)^{1/3}, \tag{5.16}$$

Meanwhile, the pull-off force contributed by one ridge is given by

$$F_{\mathrm{pf}}^{\mathrm{ridge}} = \left(\frac{\lambda^2}{4\pi^2 A R_{\mathrm{T}}} \right)^{1/3} F_{\mathrm{pf}}^{\mathrm{Flat}}, \tag{5.17}$$

By combining Eq. (5.13) - (5.17), it can be estimated that

$$F_{\mathrm{pf}}^{\mathrm{M}} = \left(\frac{2}{\pi}\right)^{10/9} \left(\frac{W}{2\pi E^{*} R_{T}}\right)^{4/9} \left(\frac{\lambda}{A}\right)^{5/9} \left(\frac{\lambda}{R_{T}}\right)^{-7/9} \cdot F_{\mathrm{pf}}^{\mathrm{Flat}}, \tag{5.18}$$

In the derivation of Eq. (5.18), the interaction between the adhesions on different ridges is neglected. To shed light on the coupling effect of adjacent adhesion points, coarse grain molecular dynamics (CGMD) simulations were carried out with LAMMPS package (see Chapter 3. Research methods for CGMD simulation details).

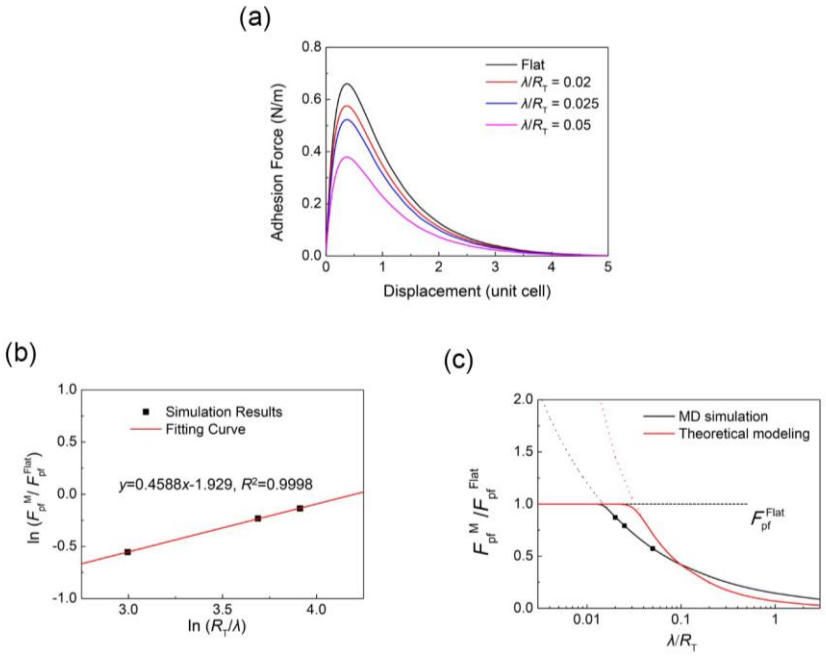

Figure 5.9. (a) The calculated dependence of the adhesion force on the displacement of the cylinder. (b) Calculated evolution of the normalized pull-off force with ln (R_{T}/λ). Here A/λ is taken as 0.5. (c) Comparison of calculated normalized pull-off force as a function λ/R_{T} with the theoretical prediction given by Eq. (5.18).

Figure 5.9a shows the evolution of the calculated adhesion force as the cylinder recedes from the substrate. Clearly, the pull-off force, which refers to the maximum adhesion force, depends on λ/R_{T}. By fitting the calculated data points (see Figure

5.9b), such dependence is found to follow the trend depicted by function of $\ln\left(F_{\mathrm{pf}}^{\mathrm{M}} / F_{\mathrm{pf}}^{\mathrm{Flat}}\right) = 0.4588 \cdot \ln\left(R_T / \lambda\right) - 1.929$, which implies

$$F_{\mathrm{pf}}^{\mathrm{M}} = 0.1453 \cdot \left(\frac{\lambda}{R_{\mathrm{T}}}\right)^{-0.4588} F_{\mathrm{pf}}^{\mathrm{Flat}}, \tag{5.19}$$

Nevertheless, both Eq. (5.18) and (5.19) indicate that $F_{\mathrm{pf}}^{\mathrm{M}}$ will go to infinity as λ approaches zero. This trend is clearly contradictory to the fact that $F_{\mathrm{pf}}^{\mathrm{M}}$ should asymptotically approach to $F_{\mathrm{pf}}^{\mathrm{Flat}}$ as λ / R_{T} approaches zero. Therefore, it should be the applicable condition of Eq. (5.18) and (5.19) that $F_{\mathrm{pf}}^{\mathrm{M}} \le F_{\mathrm{pf}}^{\mathrm{Flat}}$ or $F_{\mathrm{pf}}^{\mathrm{M}} / F_{\mathrm{pf}}^{\mathrm{Flat}} \le 1$. Figure 5.9c plots the Eq. (5.19) in comparison with Eq. (5.18). Both curves exhibit the similar trends as λ / R_{T} increases, implying that Eq. (5.18) gives a reasonable estimation to the pull-off force even though the coupling effect is neglected.

For simplicity, $A = 0.5\lambda$ for the moment is assumed firstly. Eq. (5.3), (5.8) and (5.18) comprise the whole picture of the variation of pull-off force with the characteristic length scale of surface profile, λ, as depicted by Figure 5.10a. It can be found that the pull-off force between a tubeworm larva and a rough surface could be either higher or lower than that on a flat surface, depending on the characteristic length scale of surface roughness. For a surface with sinusoidal profile as assumed, the maximum pull-off force occurs when the wave length λ is around 10 times of the tubeworm's diameter. The magnitude of the maximum pull-off force is proportional to $\left(W / \pi E^{*} R_{\mathrm{T}}\right)^{1/6}$. The minimum pull-off force, which takes place when $\lambda / R_{\mathrm{T}} = 0.1$ is

less than 45% of F_{pf}^{Flat}, implying the best anti-fouling performance of a profile with $\lambda = 0.1\ R_T$.

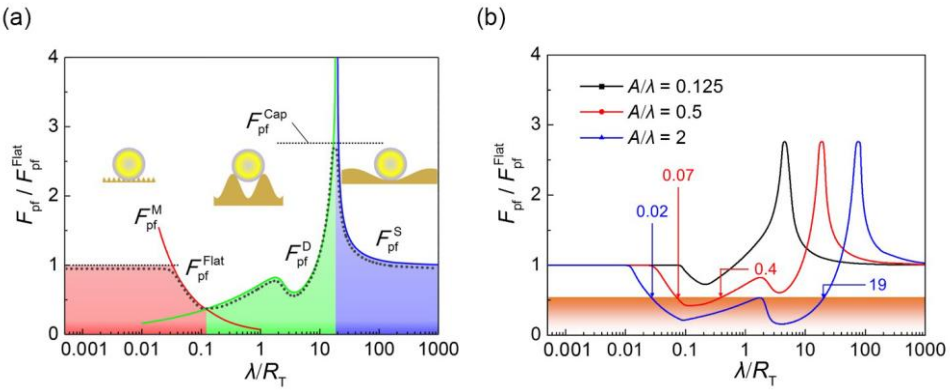

Figure 5.10. (a) Variation of the normalized pull-off force with λ/R_T for $A/\lambda = 0.5$ for three possible configurations of an elastic cylinder in adhesive contact with a wavy substrate.. (b) Effect of A/λ on pull-off force for $A/\lambda = 0.125$-2.

The analysis carried out so far is for a given ratio of $A/\lambda = 0.5$. To investigate the effects of profile amplitude A on the pull-off force, similar analysis is performed by taking $A/\lambda = 0.125$ and 2.0 respectively. Figure 5.10b compares the variations of the pull-off force as a function of λ/R_T for these three cases. When $A/\lambda = 0.125$, there is only a small range of λ/R_T giving pull-off force less than F_{pf}^{Flat} with minimum value around $0.7\ F_{pf}^{Flat}$. With increase of A/λ, the range of λ/R_T that gives rise to relatively lower pull-off force expands. When $A/\lambda = 0.5$, the range of λ/R_T in which the pull-off force is less than $0.5\ F_{pf}^{Flat}$ is 0.07-0.4. Such range extends to 0.02-19 when $A/\lambda = 2$. Considering the diversity of tubeworms in size, above results imply that high ridges can tackle the fouling of tubeworms of different sizes better. For *S. apetala* leaves and

their PDMS replicas, the inter-ridge spacing is around 5 μm which is around 10% of the radius of a tubeworm larva (~50 μm). In the light of Figure 5.10a-b, such ratio of λ/R_T should give rise to a lower pull-off force and therefore better anti-fouling performance as confirmed by the attachment tests above. Additionally, Figure 5.10a-b also imply practical guidelines for the design of anti-fouling surface with ridge-like morphology. That is, high ridges, and proper inter-ridge spacing should be adopted.

5.3 Bioinspired synthetic anti-fouling surface

The theoretical modeling indicates that high ridges with appropriate inter-ridge spacing are crucial for better anti-fouling performance. To verify this guideline and overcome the size limitation of replica of the natural anti-fouling surfaces, a synthetic surface with ridge-like morphology is prepared by water bath method with graphite paper in aqueous solution containing Nickel and Cobalt nitrates (see Figure 5.11a and Chapter 3. Research methods for details). Figure 5.11b shows the SEM images of the obtained surface which is covered with nanoflakes vertically situated on the underlying graphite substrate, giving rise to ridge-like morphology similar to that of the *S. apetala* leaves. The nanoflakes, which are identified as $NiCo_2O_4$, are around tens of nanometers in thickness and a few couple of microns in lateral dimensions. The inter-ridge spacing ranges from serval hundred nanometers to serval microns. The ratios of λ/R_T and A/λ are estimated to be in the ranges of 0.01-0.1 and 2-20 respectively which,

according to SEM images, implies great anti-fouling potential. Anti-fouling evaluation is also carried out for such synthetic ridge-like surfaces. The numbers of the attached tubeworms after 24 h and 48 h immersion are less than 10% of those on the glass slides and flat PDMS surfaces, as shown in Figure 5.11c. Such outstanding anti-fouling performance is comparable to that of the PDMS replica of the *S. apetala* leaves.

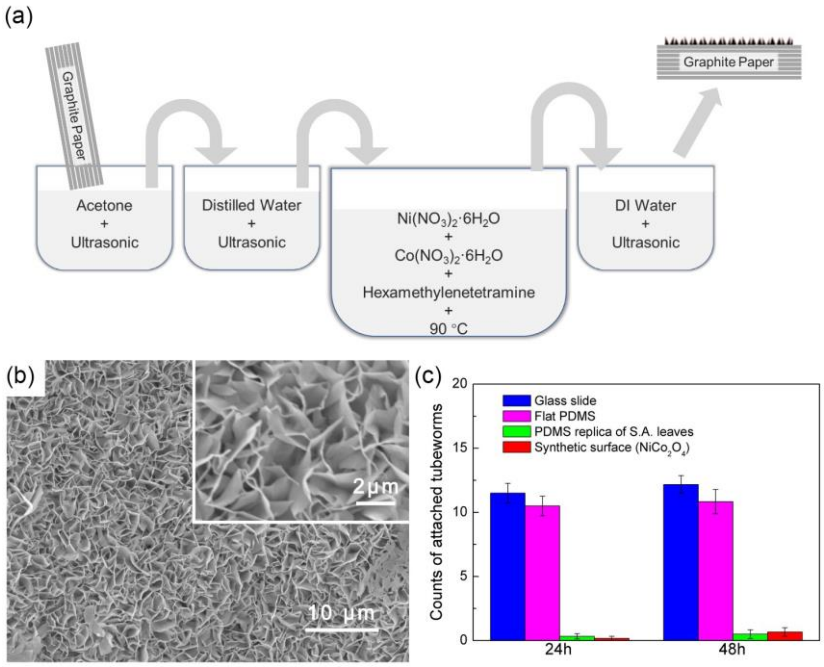

Figure 5.11. (a) Schematic of the synthesis process of anti-fouling surface. (b) SEM images of a synthetic surface with ridge-like morphology. Scale bar in the figure and inset are 10 and 2 μm respectively (c) Means ±SE (n = 6) of the total counts of tubeworms attached on the synthetic surfaces with ridge-like morphology.

5.4 Summary

Inspired by the excellent anti-fouling performance of the *S. apetala* leaves, in this chapter, the effect of surface morphology on anti-fouling performance was

investigated. It was demonstrated that the excellent anti-fouling performance of the *S. apetala* leaves can be attributed to their ridge-like surface morphology. Theoretical modeling further indicated that high ridge and proper inter-ridge spacing would reduce the attachment probability of bio-foulers and therefore facilitate anti-fouling. According to this guidance, a biomimetic surface with ridge-like morphology was synthesized. The attachment tests reconfirmed the feasibility of using ridge-like surface morphology to control biofouling. Our present study mainly focused on the effect of surface morphology. For given surface morphology, the pull-off force between the fouler and substrate also depends on the other factors such as the mechanical properties and adhesion energy of the substrate. The quantitative effects of these factors on the anti-fouling performance are still unclear and expected for in-depth investigations. Moreover, in the current study tubeworms larvae were applied to test the anti-fouling performance, so the applicability of the current ridge-like morphology to the other fouling species remains unclear and deserves further study.

Chapter 6. Bioinspired graphene-based structures with controlled fracture

In various natural materials such as nacre, bones, and teeth, consisting of brittle mineral platelets embedded in a soft, ductile organic matrix. Although the mineral constituents (*e.g.*, calcium carbonates and HAp) are brittle, the high strength and toughness of the material is ensured by using various toughening mechanisms. In facture mechanics area, much research on the crack-inclusion interaction has been conducted since the early 1960s. And among various toughening mechanisms found in biological systems, the inclusion is most common and simplest one. Similar with brittle mineral constituents in natural materials, graphene has low fracture toughness 16 J/m^2. Such low fracture toughness of graphene is unfavorable for its applications though graphene has the novel physical and mechanical properties.

To promote potential applications of graphene, especially the shielding materials, numerous studies have been carried out to advance our understanding of the strength, toughness, and fracture behavior of graphene-based materials with experimental characterization, theoretical analyses and numerical simulations. Experiments have been conducted to investigate the mechanical behaviors of multilayer graphene (thickness from 10 to 100 nm) under hypervelocity impact of spherical projectile [156]. The penetration energy of multilayer graphene is 10 times higher than that of the steel

sheets. As a powerful tool in studying the materials properties of nanomaterial, molecular dynamics (MD) simulations can be used to study the fracture behavior of the graphene-based materials. With this knowledge, several works have been focused on the topic based on molecular dynamics (MD) simulations to study fracture behavior of graphene-based materials under high-speed impact. By utilizing ReaxFF potential, the defects effect on penetration energy of graphene has been investigated [157]. It was found that the density of vacancies affects the penetration energy of graphene under impact. Obviously, crack-like defects are inevitable in materials, and materials with higher toughness will be more robust when there are preexisting cracks. In this respect, the fact that graphene has very high strength, but low toughness makes people disappointing. For protective shield applications, it will be necessary to enhance the toughness of graphene-based materials by adapting some optimal designs. Therefore, in this work, effect of inclusion on the mode I fracture of the graphene-based material were studied firstly. Then, efforts will be put on the fracture behavior of the graphene-based membrane under impact loading, by investigating the effect of the inclusion density, the inclusion modulus and impact crack shape.

6.1 Mode-I fracture in graphene-based material with inclusion

Flaws are inevitable in materials, and materials with higher toughness will be more robust when there are pre-existing cracks. The reality that graphene has low toughness

brings lot difficulties for its large-scale applications. Thus, it is very essential to explore approaches to enhance the toughness of graphene-based materials simultaneously take advantage of its ultrahigh strength. Nanostructures can be designed to enhance the toughness of materials and structure. For example, wrinkling induced by a controlled distribution of topological defects such as disclinations and dislocations can be utilized to control the structures of 3D graphene, which will increase the toughness [158]. A question arises: Is it possible to enhance the toughness of graphene-based materials by using simpler nanostructures, such as inclusions or pre-existing holes. Therefore, in this work, I will first study the effect of inclusion on the mode I fracture of the graphene-based material.

The fracture behavior of graphene-based materials with inclusion under the tensile loading is obtained by conducting a series of MD simulations with LAMMPS package [87]. The planar dimensions of the graphene-based with inclusion samples performed in the simulations were 30 nm × 30 nm, and the length of the crack was set as 1.5 nm to exclude the crack length effect of the simulation results. Figure 6.1 shows simulation samples with a circular inclusion in the center. Both graphene and graphene-like inclusion have a same bond structure with bond lengths of 1.42 Å, and the graphene-like inclusion was modeled by setting the corresponding parameters of the potential. The graphene-like inclusion was bonded to the graphene and all the bonded interactions were described by the AIREBO potential. The range of the elastic modulus

of graphene-like inclusion E_I is from 0.125-8 times that of graphene E_G. The crack was generated by deleting carbon atoms.

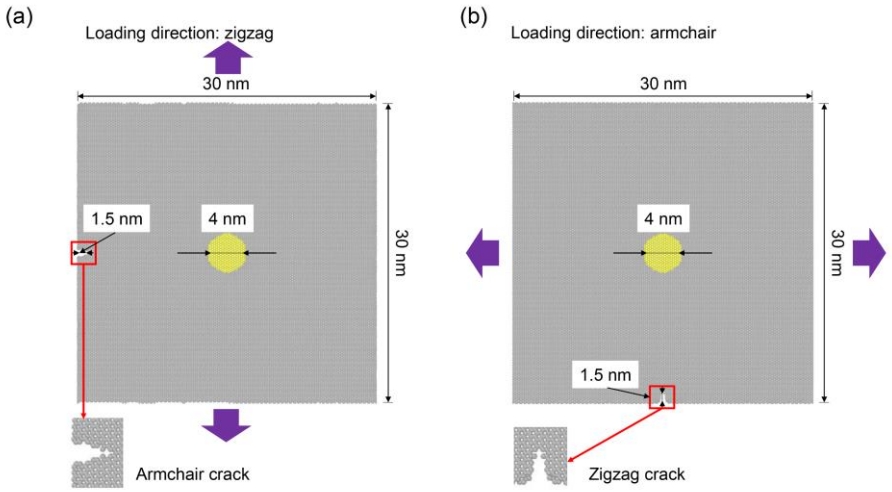

Figure 6.1. MD simulation models: Samples of graphene containing a preexisting crack and a circular inclusion. (a) and (b) show the models with armchair and zigzag crack-tips, respectively. The loading direction is indicated as the violet arrows.

Energy minimization of the samples was conducted by using the conjugate gradient algorithm at the initial stage of all MD simulations. Then, the samples were relaxed at the equilibrium configuration for 20 ps with a time step of 0.5 fs. All the simulations were conducted by using the isothermal–isobaric (NPT) ensemble. The temperature was kept at 1 K by using Nośe-Hoover thermostat. After the samples reached equilibrium state, the samples were subjected to uniaxial tensile loading at a strain rate of 0.5 fs^{-1}.

Figure 6.2 shows the stress-strain curves of graphene-based materials with single inclusion under the tensile loading along the zigzag and the armchair directions. It can

be found that the strains of graphene-based materials at fracture point under the tensile loading along armchair and zigzag directions are almost same. It can be noticed that the fracture stress of graphene-based with inclusion materials is depend on the E_I. When the E_I are smaller than the E_G (see dash-line in Figure 6.2), the inclusion sustains comparatively much lower strain leading to a lower fracture stress of the whole sample. In contrast, all the samples with the inclusion with higher elastic modulus have almost identical fracture stress to the pure graphene under uniaxial-tensile loading (see solid-line in Figure 6.2).

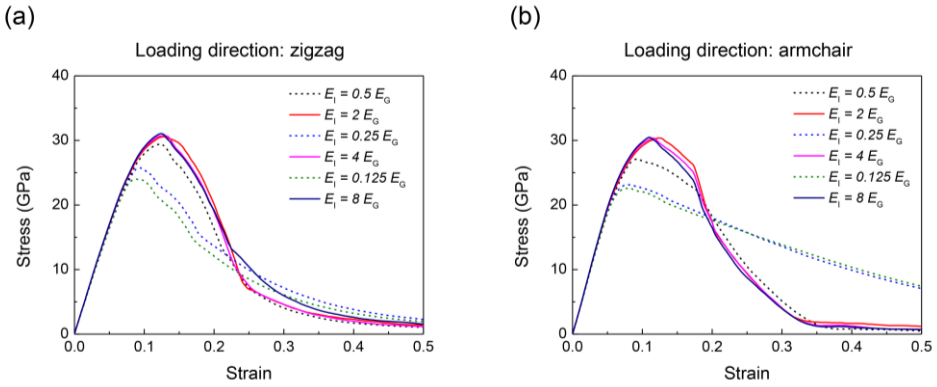

Figure 6.2. Uniaxial tension stress-strain of graphene-based with inclusion materials when loaded along zigzag and armchair directions.

In order to investigate the effect of the inclusions on the strain field at the crack-tip. The volumetric strain distribution contour of the zigzag crack-tip cases at strain ε_{xx} of 10% is shown in Figure 6.3. The strain field comparison between a softer and a harder inclusion clearly depicts that E_I has a great influence on the strain field ahead of crack-tip. Depending on the relative elastic modulus of the inclusion with respect to the

graphene, the inclusion can give rise to an increase of the crack-tip strain field (guiding effect) for a softer inclusion or a decrease of the crack-tip strain field (shielding effect) for a harder inclusion.

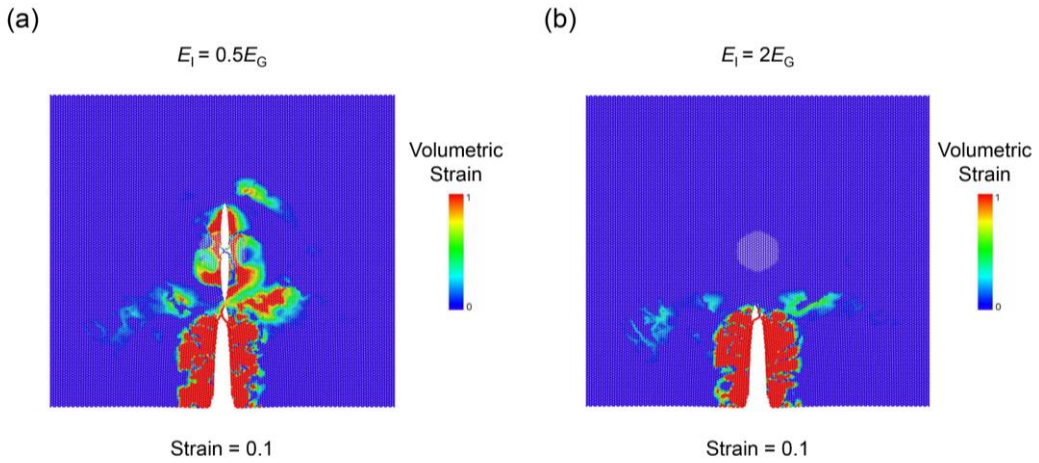

Figure 6.3. The volumetric strain contour of the zigzag crack-tip cases at strain ε_{xx} of 10% in the presence of one inclusion (a) with $E_I = 0.5E_G$ and (b) $E_I = 2E_G$, respectively.

6.2 Dynamical impact fracture in graphene

The fracture behavior of graphene under impact is obtained by conducting a series of MD simulations with LAMMPS package[87]. A spherical rigid projectile is used to impact the graphene. In the impact simulation, the graphene is fixed in the lateral directions, as shown in Figure 6.4. The projectile with the initial velocity V equal to 500 m/s is placed in the center of the graphene sample. To exclude the influence of thermal fluctuations, the initial system temperature was set as 1 K. As setting in above uniaxial-tensile simulations, the cut-off distance of C-C bond was chosen as 2.0 Å to capture the bond breaking during impact. The interactions between atoms in projectile

and graphene were described by Morse potential [98].

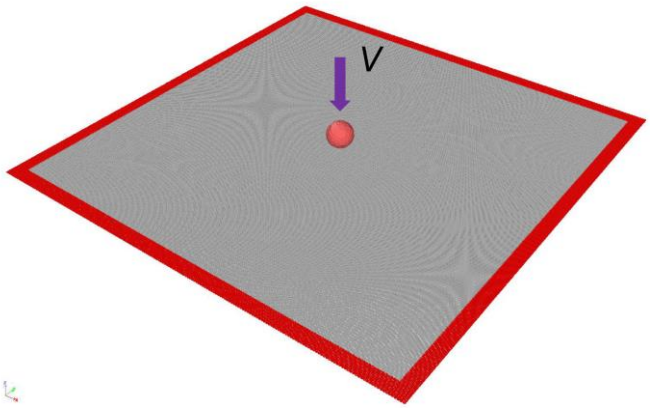

Figure 6.4. Schematic view of the impact simulation on the monolayer graphene. Graphene is fixed in the lateral directions at the edges, colored in red. The projectile impacts on the center of the graphene sample.

From Figure 6.5, the final stage of the crack propagation featured by a crack along the zigzag direction. Such zigzag direction crack phenomenon is same as that of uniaxial tensile simulation. Moreover, it can be found that the crack propagates preferentially along the zigzag direction, which is in line with previous studies [159].

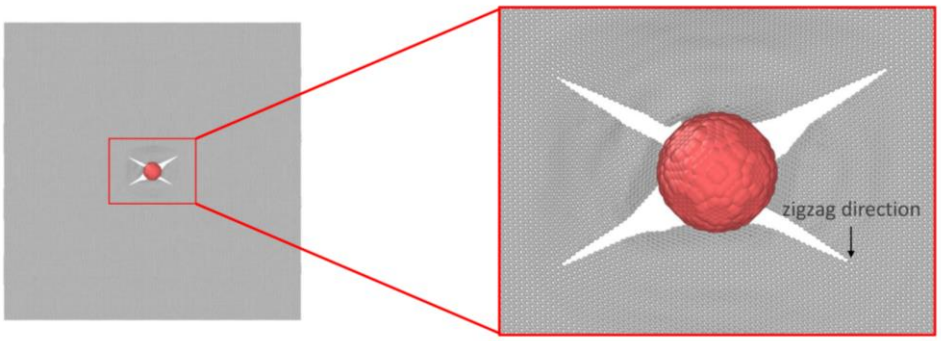

Figure 6.5. Atomic configurations of the graphene membrane showing the final failure shape induced by the projectile.

6.3 Dynamical impact fracture in graphene with inclusions

The fracture behavior of graphene-based materials under impact is obtained by conducting a series of MD simulations with LAMMPS package [87], as shown in Figure 6.6. Other than the inclusions, the simulations setting is same as that of the graphene under impact case. The range of the elastic modulus of graphene-like inclusions E_I is from 0.5-2 times that of graphene E_G.

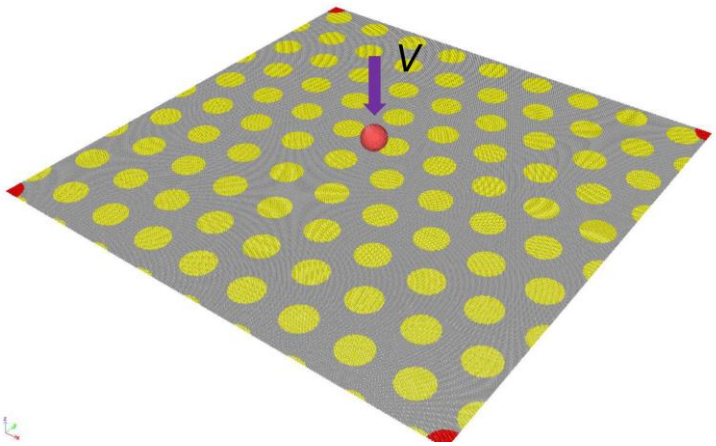

Figure 6.6. Schematic view of the impact simulation on the monolayer graphene-based material. A graphene-based material is fixed in the lateral directions at the corners, colored in red. The projectile is placed in the center of the graphene-based sample.

To investigate the effect of the inclusions on the anti-crack (shielding) performance, a series of MD simulations were conducted. In these simulations, inclusions were in the hexagon pattern, as shown in Figure 6.7. The distances between the adjacent inclusions was fixed at 10 nm, the radius of the inclusion was in the range from 2 nm to 4 nm.

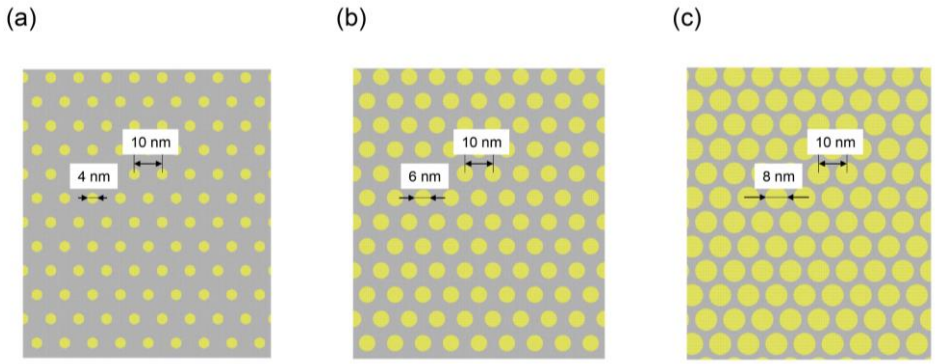

Figure 6.7. Inclusion pattern of the graphene-based material. Inclusions are in the hexagon pattern, colored in yellow. The distance between the adjacent inclusions is 10 nm, the diameter of the inclusion is in the range from 4 nm to 8 nm.

Figure 6.8-6.9 shows the number of breaking bonds in the graphene-based membrane as a function of time. As illustrated in Figure 6.8, the number of breaking bonds in all cases shows a similar trend with the decrease of the E_I. The number of breaking bonds in the cases with softer inclusions (E_I = 0.5 E_G) shows increasing trend with the decrease of the R_I, while the number of breaking bonds in the cases with harder inclusions (E_I = 2 E_G) shows increasing trend with the increase of the R_I, as shown in Figure 6.9. Similar results can be observed from the uniaxial tensile cases for Mode I fracture in Section 6.1. Depending on the relative elastic modulus of the inclusion with respect to the graphene, the inclusions can result in an increase of the crack length (guiding effect) for softer inclusions or a decrease of the crack length (shielding effect) for harder inclusions. To utilize the shielding effect of the inclusion, the harder inclusions should be placed in denser pattern (with larger R_I).

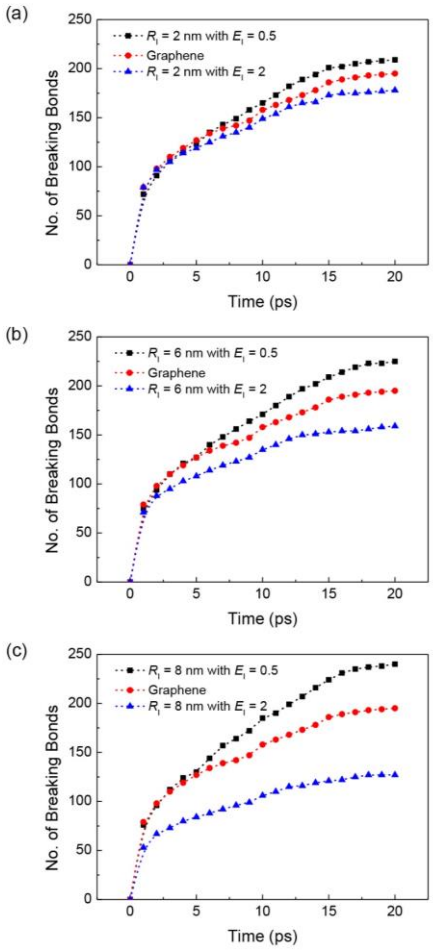

Figure 6.8. Number of breaking bonds in the membrane as a function of time for different samples. The radius of graphene-like inclusions R_I is, (a) 2 nm, (b) 3nm, (c) 4nm.

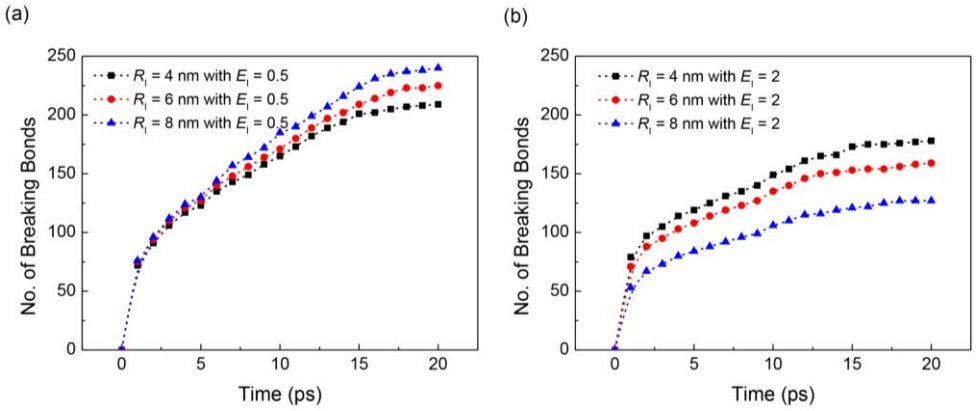

Figure 6.9. Number of breaking bonds in the membrane as a function of time for different samples. The elastic modulus of graphene-like inclusions E_I is, (a) 0.5 E_G, (b) 2 E_G.

6.4 Summary

In this chapter, the Mode I fracture in graphene-based material with a single inclusion and fracture behavior of graphene-based materials with inclusions troop under impact were investigated by MD simulations. Results show that the inclusions embedded in the graphene-based material can change crack path. Based on the simulation results, I propose several means to improve anti-crack performance by using the shielding effect of the inclusions in the graphene-based material: (1) choosing a harder inclusion, (2) increasing the radius of inclusion, R_I. Further simulations should be conducted on the control cases, including the different inclusion pattern, and theoretical modeling should be built to find out the mechanism for optimizing the shielding effect of the inclusions. Although the findings are derived based on graphene, it can be generalized to the other brittle 2D materials. This study should be of great importance for the design of the protective shield with ultralight material.

Chapter 7. Conclusions and future work

In this thesis, some typical mechanical behaviors in biological and related bioinspired application were investigated. Based on these results, guidelines for optimization of the designs of the anti-wear, anti-fouling and anti-crack materials are proposed. In this chapter, conclusions about the optimization strategies proposed will be presented, and an outlook of the future work will be delivered.

7.1 Conclusions

Biomechanics deals with mechanics concerned with biological systems. As one of the most rapidly growing fields of mechanics, it can help us understand how the natural systems work in mechanical phenomena as well as how bioinspired material and structures should be manufactured. Herein, by means of experiments, theoretical modeling and MD simulations, I revealed the mechanical mechanisms accounting for the novel mechanical properties of the natural materials and proposed several guidelines for applications in bioinspired materials. The typical conclusions are as following.

- Inspired by the outstanding wear resistance exhibited by the OS of black carp teeth, a comparative XRD analysis on its enameloid was carried out and the *c*-axis preferential orientation of the building HAp crystallites near the OS was uncovered. Subsequent MD simulation demonstrated that the (001)

surface of single crystal HAp exhibits better wear resistance compared to other surfaces. The theoretical analysis was performed to further reveal the mechanics accounting for the orientation-dependent wear resistance of HAp crystal. It was revealed that scratching on the (001) surface of HAp tends to cause plastic deformation ('rubbing mode' failure) rather than removal of materials ('cutting mode' failure) because for (001) surface 'rubbing mode' failure is more preferable in energy than 'cutting mode' failure when the attack angle α is smaller than a critical value α_c. The finding of the work shows great promise of applying preferential orientation of crystals to increase the wear resistance of materials.

- Inspired by the superior anti-fouling performance of the *S. apetala* leaves, the effect of surface morphology on anti-fouling performance was investigated. The excellent anti-fouling performance of the *S. apetala* leaves can be attributed to their ridge-like surface morphology. Theoretical modeling further indicated that high ridge and proper inter-ridge spacing would reduce the attachment probability of fouler and therefore facilitate anti-fouling. According to this guidance, a biomimetic surface with ridge-like morphology was synthesized and was reconfirmed with the ability to control biofouling. The applicability of the current ridge-like morphology to the other fouling species remains unclear and deserves further study. Our

present study mainly focused on the effect of surface morphology. More effects of surface properties will be investigated in the future.

- Inspired by the toughness mechanism of the inclusions in natural biomaterials, the Mode I fracture in graphene-based material with a single inclusion and fracture behavior of graphene-based materials with inclusions troop under impact was investigated by MD simulations. Results show that the inclusions structure embedded in the graphene-based material can change the crack path. Based on the simulations results, several means to improve anti-crack performance by using the shielding effect of the inclusions in the graphene-based material were proposed: (1) choosing a harder inclusion, (2) increasing the radius of inclusion, R_I.

Thus, above investigations not only uncover the mechanisms accounting for the prominent mechanical properties of the natural materials but provide practical strategies for the design of bioinspired materials and structures with superior mechanical properties that can be widely used in anti-wear, anti-fouling and anti-crack applications.

7.2 Outlook to the future research

The work in this thesis was focused on the mechanical behaviors of natural materials and optimal design of bioinspired materials from the mechanical perspective. The

future directions include the following aspects.

7.2.1 Wear behavior and dynamical impact fracture in multi-layer graphene-based structures

It has been widely reported that the novel mechanical properties of graphene have drawn significant interests and triggered a lot of potential applications (see Chapter 6.1). The conclusions obtained in Chapter 6 are coarse and qualitative. Further simulations should be conducted on the control cases, including the different inclusion pattern (geomatical parameters, *e.g.*, inclusion shape, inclusion array pattern, relative size of a single inclusion with respect to the projectile.) and the impact velocity of the projectile, and theoretical modeling should be built to find out the mechanism for optimizing the shielding effect of the inclusions. And experimentally verifications are needed. Thus, following the guidance of the previous simulation results, a definite and quantitative relationship that can reveal the mechanism will be built in the future.

As there are a lot of similarities between the surface protection during impact and wear. The wear behavior of the graphene-based material is planned to be addressed following the study of the dynamical impact. In the conclusion of Chapter 4, a similar anti-wear mechanism has also been reported in the other natural materials such as bones[132-134], human teeth[84, 160], teeth of sea urchin[135], and bamboo[136]. To apply the mechanism, the mechanical properties, that is, shear strength and indentation hardness,

of the graphene-based composite materials, can be tuned by material composition or structure. The results of this work can act as a guideline for the choice of the anti-wear coating based on the anti-wear mechanism learned from nature, which is believed to be of great help to the industry.

7.2.2 Design anti-fouling coating for the application in the field

In Chapter 5, the emphasis of present study was mainly the effect of surface morphology. From the theoretical modeling, for given surface morphology, the pull-off force to separate the fouler and substrate also depends on the other factors such as the mechanical properties such as elastics modulus and adhesion energy between them. The quantitative effects of these factors on the anti-fouling performance are expected for further investigations. Moreover, in the current study only tubeworms were used to evaluate the anti-fouling performance. The applicability of the current ridge-like morphology to other fouling species deserves further study, especially for the future application in field.

References

1. Ritchie, R.O., M.J. Buehler, and P. Hansma, Plasticity and toughness in bone. *Physics Today*, 2009. **62**(6): p. 41-47.

2. Tian, Y., et al., Adhesion and friction in gecko toe attachment and detachment. *Proc Natl Acad Sci U S A*, 2006. **103**(51): p. 19320-5.

3. Cheng, Y.T., et al., Effects of micro- and nano-structures on the self-cleaning behaviour of lotus leaves. *Nanotechnology*, 2006. **17**(5): p. 1359-62.

4. Lepore, E. and N. Pugno, Superhydrophobic Polystyrene by Direct Copy of a Lotus Leaf. *BioNanoScience*, 2011. **1**(4): p. 136-43.

5. Furstner, R., et al., Wetting and self-cleaning properties of artificial superhydrophobic surfaces. *Langmuir*, 2005. **21**(3): p. 956-61.

6. Bormashenko, E., et al., Wetting properties of the multiscaled nanostructured polymer and metallic superhydrophobic surfaces. *Langmuir*, 2006. **22**(24): p. 9982-5.

7. Hansen, W.R. and K. Autumn, Evidence for self-cleaning in gecko setae. *Proc Natl Acad Sci U S A*, 2005. **102**(2): p. 385-9.

8. Lee, K., et al., Self-assembly of amorphous calcium carbonate microlens arrays. *Nat Commun*, 2012. **3**: p. 725.

9. Yin, S., et al., Enhanced photocurrent generation of bio-inspired graphene/ZnO composite films. *Journal of Materials Chemistry A*, 2015. **3**(22): p. 12016-22.

10. Wang, J., et al., Bioinspired Hierarchical Alumina-Graphene Oxide-Poly(vinyl alcohol) Artificial Nacre with Optimized Strength and Toughness. *ACS Appl Mater Interfaces*, 2015. **7**(17): p. 9281-6.

11. Galloway, J.M., J.P. Bramble, and S.S. Staniland, Biomimetic synthesis of materials for technology. *Chemistry*, 2013. **19**(27): p. 8710-25.

12. Yang, S., et al., Synthesis of photoacid crosslinkable hydrogels for the fabrication of soft, biomimetic microlens arrays. *Journal of Materials Chemistry*, 2005. **15**(39): p. 4200.

13. Pokroy, B., et al., Fabrication of Bioinspired Actuated Nanostructures with Arbitrary Geometry and Stiffness. *Advanced Materials*, 2009. **21**(4): p. 463-+.

14. Li, Y., et al., Bioinspired silica surfaces with near-infrared improved transmittance and superhydrophobicity by colloidal lithography. *Langmuir*, 2010. **26**(12): p. 9842-7.

15. Wegst, U.G.K. and M.F. Ashby, The mechanical efficiency of natural materials. *Philosophical Magazine*, 2004. **84**(21): p. 2167-86.

16. Fratzl, P., Biomimetic materials research: what can we really learn from nature's structural materials? *J R Soc Interface*, 2007. **4**(15): p. 637-42.

17. Qin, Z., L. Kreplak, and M.J. Buehler, Hierarchical structure controls nanomechanical properties of vimentin intermediate filaments. *PLoS One*, 2009. **4**(10): p. e7294.

18. Nova, A., et al., Molecular and nanostructural mechanisms of deformation, strength and toughness of spider silk fibrils. *Nano Lett*, 2010. **10**(7): p. 2626-34.

19. Espinosa, H.D., et al., Tablet-level origin of toughening in abalone shells and translation to synthetic composite materials. *Nat Commun*, 2011. **2**: p. 173.

20. Autumn, K., et al., Frictional adhesion: A new angle on gecko attachment. *J Exp Biol*, 2006. **209**(Pt 18): p. 3569-79.

21. Pugno, N.M. and E. Lepore, Living Tokay Geckos Display Adhesion Times Following Weibull Statistics. *The Journal of Adhesion*, 2008. **84**(11): p. 947-60.

22. Wong, T.S., et al., Bioinspired self-repairing slippery surfaces with pressure-stable omniphobicity. *Nature*, 2011. **477**(7365): p. 443-7.

23. Rousseau, M., et al., Sheet nacre growth mechanism: a Voronoi model. *J Struct Biol*, 2005. **149**(2): p. 149-57.

24. Rousseau, M., et al., Dynamics of sheet nacre formation in bivalves. *J Struct Biol*, 2009. **165**(3): p. 190-5.

25. Jackson, A.P., J.F.V. Vincent, and R.M. Turner, A physical model of nacre. *Composites Science and Technology*, 1989. **36**(3): p. 255-66.

26. Tang, H., F. Barthelat, and H. Espinosa, An elasto-viscoplastic interface model for investigating the constitutive behavior of nacre. *Journal of the Mechanics and Physics of Solids*, 2007. **55**(7): p. 1410-38.

27. Jäger, I. and P. Fratzl, Mineralized Collagen Fibrils: A Mechanical Model with a Staggered Arrangement of Mineral Particles. *Biophys. J.*, 2000.

79(4): p. 1737-46.

28. Gao, H., et al., Materials become insensitive to flaws at nanoscale: lessons from nature. *Proc Natl Acad Sci U S A*, 2003. **100**(10): p. 5597-600.

29. Dugdale, D.S., Yielding of steel sheets containing slits. *Journal of the Mechanics and Physics of Solids*, 1960. **8**(2): p. 100-04.

30. Ji, B. and H. Gao, Mechanical properties of nanostructure of biological materials. *Journal of the Mechanics and Physics of Solids*, 2004. **52**(9): p. 1963-90.

31. Gao, H. and H. Yao, Shape insensitive optimal adhesion of nanoscale fibrillar structures. *Proc Natl Acad Sci U S A*, 2004. **101**(21): p. 7851-6.

32. Lee, H., B.P. Lee, and P.B. Messersmith, A reversible wet/dry adhesive inspired by mussels and geckos. *Nature*, 2007. **448**(7151): p. 338-U4.

33. Baum, M.J., L. Heepe, and S.N. Gorb, Friction behavior of a microstructured polymer surface inspired by snake skin. *Beilstein J Nanotechnol*, 2014. **5**: p. 83-97.

34. Neville, A., et al., Synovial joint lubrication-does nature teach more effective engineering lubrication strategies? *Proceedings of the Institution of Mechanical Engineers, Part C: Journal of Mechanical Engineering Science*, 2007. **221**(10): p. 1223-30.

35. Zum Gahr, K.-H., *Microstructure and wear of materials*. Vol. 10. 1987: Elsevier.

36. Amini, S. and A. Miserez, Wear and abrasion resistance selection maps of biological materials. *Acta Biomater.*, 2013. **9**(8): p. 7895-907.

37. Hsu, C.C., et al., Influence of 8DSS peptide on nano-mechanical behavior of human enamel. *J Dent Res*, 2011. **90**(1): p. 88-92.

38. Giannini, M., C.J. Soares, and R.M. de Carvalho, Ultimate tensile strength of tooth structures. *Dental Materials*, 2004. **20**(4): p. 322-29.

39. Cui, F.Z. and J. Ge, New observations of the hierarchical structure of human enamel, from nanoscale to microscale. *J Tissue Eng Regen Med*, 2007. **1**(3): p. 185-91.

40. Eimar, H., et al., Regulation of enamel hardness by its crystallographic dimensions. *Acta Biomater*, 2012. **8**(9): p. 3400-10.

41. Cevc, G., et al., The caries resistance of human teeth is determined

by the spatial arrangement of hydroxyapatite microcrystals in the enamel. *Nature*, 1980. **286**(5771): p. 425-26.

42. Ge, J., et al., Property variations in the prism and the organic sheath within enamel by nanoindentation. *Biomaterials*, 2005. **26**(16): p. 3333-9.

43. Anusavice, K.J., Standardizing failure, success, and survival decisions in clinical studies of ceramic and metal-ceramic fixed dental prostheses. *Dent Mater*, 2012. **28**(1): p. 102-11.

44. Bechtle, S., S.F. Ang, and G.A. Schneider, On the mechanical properties of hierarchically structured biological materials. *Biomaterials*, 2010. **31**(25): p. 6378-85.

45. Mattei, L., et al., Lubrication and wear modelling of artificial hip joints: A review. *Tribology International*, 2011. **44**(5): p. 532-49.

46. Coldea, A., M.V. Swain, and N. Thiel, Mechanical properties of polymer-infiltrated-ceramic-network materials. *Dent Mater*, 2013. **29**(4): p. 419-26.

47. Dirxen, C., U. Blunck, and S. Preissner, Clinical performance of a new biomimetic double network material. *Open Dent J*, 2013. **7**: p. 118-22.

48. Rechberger, M., et al., New tribological strategies for cutting tools following nature. *Tribology International*, 2013. **63**: p. 243-49.

49. Swain, G.W. and M.P. Schultz, The testing and evaluation of non-toxic antifouling coatings. *Biofouling*, 1996. **10**(1-3): p. 187-97.

50. Bers, A.V. and M. Wahl, The influence of natural surface microtopographies on fouling. *Biofouling*, 2004. **20**(1): p. 43-51.

51. Yebra, D.M., S. Kiil, and K. Dam-Johansen, Antifouling technology - past, present and future steps towards efficient and environmentally friendly antifouling coatings. *Prog. Org. Coat.*, 2004. **50**(2): p. 75-104.

52. Carman, M.L., et al., Engineered antifouling microtopographies-correlating wettability with cell attachment. *Biofouling*, 2006. **22**(1-2): p. 11-21.

53. Genzer, J. and K. Efimenko, Recent developments in superhydrophobic surfaces and their relevance to marine fouling: a review. *Biofouling*, 2006. **22**(5): p. 339-60.

54. Vrolijk, N.H., et al., Surface characterisation of two gorgonian coral species: Implications for a natural antifouling defence. *Biofouling*, 1990. **2**(1):

p. 39-54.

55. J., D., *Antifouling properties of the dogfish egg case and their possible application in developing nontoxic alternatives to antifouling paints*. 1999. 21–36.

56. Ball, P., Engineering Shark skin and other solutions. *Nature*, 1999. **400**(6744): p. 507-09.

57. Pu, X., G. Li, and H. Huang, Preparation, anti-biofouling and drag-reduction properties of a biomimetic shark skin surface. *Biol Open*, 2016. **5**(4): p. 389-96.

58. Bechert, D.W., M. Bruse, and W. Hage, Experiments with three-dimensional riblets as an idealized model of shark skin. *Experiments in Fluids*, 2000. **28**(5): p. 403-12.

59. Wahl, M., K. Kröger, and M. Lenz, Non‐toxic protection against epibiosis. *Biofouling*, 1998. **12**(1-3): p. 205-26.

60. Scardino, A., et al., Microtopography and antifouling properties of the shell surface of the bivalve molluscs Mytilus galloprovincialis and Pinctada imbricata. *Biofouling*, 2003. **19 Suppl**: p. 221-30.

61. Guenther, J., P.C. Southgate, and R. de Nys, The effect of age and shell size on accumulation of fouling organisms on the Akoya pearl oyster Pinctada fucata (Gould). *Aquaculture*, 2006. **253**(1-4): p. 366-73.

62. Anselme, K., et al., The interaction of cells and bacteria with surfaces structured at the nanometre scale. *Acta Biomater*, 2010. **6**(10): p. 3824-46.

63. Scardino, A.J., et al., The role of nano-roughness in antifouling. *Biofouling*, 2009. **25**(8): p. 757-67.

64. Efimenko, K., et al., Development and testing of hierarchically wrinkled coatings for marine antifouling. *ACS Appl Mater Interfaces*, 2009. **1**(5): p. 1031-40.

65. Erbil, H.Y., et al., Transformation of a simple plastic into a superhydrophobic surface. *Science*, 2003. **299**(5611): p. 1377-80.

66. Marmur, A., Super-hydrophobicity fundamentals: implications to biofouling prevention. *Biofouling*, 2006. **22**(1-2): p. 107-15.

67. Magin, C.M., S.P. Cooper, and A.B. Brennan, Non-toxic antifouling strategies. *Materials Today*, 2010. **13**(4): p. 36-44.

68. Zhang, H., R. Lamb, and J. Lewis, Engineering nanoscale roughness on hydrophobic surface-preliminary assessment of fouling behaviour. *Science and Technology of Advanced Materials*, 2005. **6**(3-4): p. 236-39.

69. Baum, C., et al., Average nanorough skin surface of the pilot whale (Globicephala melas, Delphinidae): considerations on the self-cleaning abilities based on nanoroughness. *Mar. Biol.*, 2002. **140**(3): p. 653-57.

70. Schumacher, J.F., et al., Engineered antifouling microtopographies-effect of feature size, geometry, and roughness on settlement of zoospores of the green alga Ulva. *Biofouling*, 2007. **23**(1-2): p. 55-62.

71. Schultz, M.P., Effects of coating roughness and biofouling on ship resistance and powering. *Biofouling*, 2007. **23**(5): p. 331-41.

72. Ranella, A., et al., Tuning cell adhesion by controlling the roughness and wettability of 3D micro/nano silicon structures. *Acta Biomater.*, 2010. **6**(7): p. 2711-20.

73. Aldred, N., et al., Attachment strength is a key factor in the selection of surfaces by barnacle cyprids (Balanus amphitrite) during settlement. *Biofouling*, 2010. **26**(3): p. 287-99.

74. Scardino, A.J., E. Harvey, and R. De Nys, Testing attachment point theory: diatom attachment on microtextured polyimide biomimics. *Biofouling*, 2006. **22**(1): p. 55-60.

75. Scardino, A.J., J. Guenther, and R. de Nys, Attachment point theory revisited: the fouling response to a microtextured matrix. *Biofouling*, 2008. **24**(1): p. 45-53.

76. Xia, Z., *Biomimetic principles and design of advanced engineering materials*. 2016. i-xii.

77. Espinosa, H.D., et al., Merger of structure and material in nacre and bone-Perspectives on de novo biomimetic materials. *Progress in Materials Science*, 2009. **54**(8): p. 1059-100.

78. Keten, S., et al., Nanoconfinement controls stiffness, strength and mechanical toughness of beta-sheet crystals in silk. *Nat Mater*, 2010. **9**(4): p. 359-67.

79. Shao, Z. and F. Vollrath, Surprising strength of silkworm silk. *Nature*, 2002. **418**(6899): p. 741.

80. Kakisawa, H. and T. Sumitomo, The toughening mechanism of nacre

and structural materials inspired by nacre. *Science and Technology of Advanced Materials*, 2011. **12**(6): p. 064710.

81. Mayer, G., Rigid biological systems as models for synthetic composites. *Science*, 2005. **310**(5751): p. 1144-7.

82. Beese, A.M., et al., Bio-inspired carbon nanotube-polymer composite yarns with hydrogen bond-mediated lateral interactions. *ACS Nano*, 2013. **7**(4): p. 3434-46.

83. Qing, P., et al., Effect of gamma irradiation on the wear behaviour of human tooth enamel. *Sci Rep*, 2015. **5**: p. 11568.

84. Zheng, S.Y., et al., Investigation on the microtribological behaviour of human tooth enamel by nanoscratch. *Wear*, 2011. **271**(9-10): p. 2290-96.

85. Jia, Y.-F. and F.-Z. Xuan, Anisotropic wear behavior of human enamel at the rod level in terms of nanoscratching. *Wear*, 2012. **290-291**: p. 124-32.

86. Verlet, L., Computer "experiments" on classical fluids. I. Thermodynamical properties of lennard-jones molecules. *Physical Review*, 1967. **159**(1): p. 98-103.

87. Plimpton, S., Fast Parallel Algorithms for Short-Range Molecular-Dynamics. *J. Comput. Phys.*, 1995. **117**(1): p. 1-19.

88. Humphrey, W., A. Dalke, and K. Schulten, VMD: visual molecular dynamics. *J. Mol. Graph.*, 1996. **14**(1): p. 33-38.

89. Stukowski, A., Visualization and analysis of atomistic simulation data with ovito-the open visualization tool. *Modell. Simul. Mater. Sci. Eng.*, 2010. **18**(1): p. 015012.

90. Qin, Z., et al., Thickness of hydroxyapatite nanocrystal controls mechanical properties of the collagen-hydroxyapatite interface. *Langmuir*, 2012. **28**(4): p. 1982-92.

91. Libonati, F., et al., Fracture mechanics of hydroxyapatite single crystals under geometric confinement. *J. Mech. Behav. Biomed. Mater.*, 2013. **20**: p. 184-91.

92. MacKerell, A.D., et al., All-atom empirical potential for molecular modeling and dynamics studies of proteins. *J. Phys. Chem. B*, 1998. **102**(18): p. 3586-616.

93. Stuart, S.J., A.B. Tutein, and J.A. Harrison, A reactive potential for

hydrocarbons with intermolecular interactions. *The Journal of Chemical Physics*, 2000. **112**(14): p. 6472.

94. Cranford, S.W. and M.J. Buehler, Mechanical properties of graphyne. *Carbon*, 2011. **49**(13): p. 4111-21.

95. Zhao, J., et al., The mechanical properties of three types of carbon allotropes. *Nanotechnology*, 2013. **24**(9): p. 095702.

96. O'Connor, T.C., J. Andzelm, and M.O. Robbins, AIREBO-M: A reactive model for hydrocarbons at extreme pressures. *J. Chem. Phys.*, 2015. **142**(2): p. 024903.

97. Brenner, D.W., et al., A second-generation reactive empirical bond order (REBO) potential energy expression for hydrocarbons. *J. Phys.-Condes. Matter*, 2002. **14**(4): p. 783-802.

98. Rountree, C.L., et al., Atomistic aspects of crack propagation in brittle materials: Multimillion atom molecular dynamics simulations. *Ann. Rev. Mater. Res.*, 2002. **32**: p. 377-400.

99. Guo, S.-J., et al., Modeling of interface cracking in copper–graphite composites by MD and CFE method. *Composites Part B: Engineering*, 2014. **58**: p. 586-92.

100. Meyers, M.A., et al., The cutting edge: sharp biological materials. *Jom*, 2008. **60**(3): p. 19-24.

101. Yao, H., et al., Protection mechanisms of the iron-plated armor of a deep-sea hydrothermal vent gastropod. *Proc. Natl. Acad. Sci. USA*, 2010. **107**(3): p. 987-92.

102. Xie, Z. and H. Yao, Crack deflection and flaw tolerance in "brick-and-mortar" structured composites. *Int. J. Appl. Mech.*, 2014. **6**(2): p. 1450017.

103. Yang, W., et al., Protective role of Arapaima gigas fish scales: structure and mechanical behavior. *Acta Biomater.*, 2014. **10**: p. 3599-614.

104. Bruet, B.J.F., et al., Materials design principles of ancient fish armour. *Nat. Mater.*, 2008. **7**: p. 748-56.

105. Podsiadlo, P., et al., Ultrastrong and stiff layered polymer nanocomposites. *Science*, 2007. **318**(5847): p. 80-83.

106. Munch, E., et al., Tough, Bio-Inspired Hybrid Materials. *Science*, 2008. **322**(5907): p. 1516-20.

107. Bonderer, L.J., A.R. Studart, and L.J. Gauckler, Bioinspired design and assembly of platelet reinforced polymer films. *Science*, 2008. **319**(5866): p. 1069-73.

108. Meyers, M.A., et al., Battle in the Amazon: Arapaima versus Piranha. *Adv. Eng. Mater.*, 2012. **14**(5): p. B279-B88.

109. Brandt, K., et al., A novel method for a multi-level hierarchical composite with brick-and-mortar structure. *Sci Rep*, 2013. **3**: p. 2322.

110. Xu, S., et al., Molecular dynamics simulations of nano-indentation and wear of the gamma Ti-Al alloy. *Comput. Mater. Sci.*, 2015. **110**: p. 247-53.

111. Sha, Z.D., et al., Large-scale molecular dynamics simulations of wear in diamond-like carbon at the nanoscale. *Appl. Phys. Lett.*, 2013. **103**(7): p. 073118.

112. Gotsmann, B. and M.A. Lantz, Atomistic wear in a single asperity sliding contact. *Phys. Rev. Lett.*, 2008. **101**(12): p. 125501.

113. Vargonen, M., et al., Molecular simulation of tip wear in a single asperity sliding contact. *Wear*, 2013. **307**(1-2): p. 150-54.

114. Hu, X.L. and A. Martini, Atomistic simulation of the effect of roughness on nanoscale wear. *Comput. Mater. Sci.*, 2015. **102**: p. 208-12.

115. Kim, H.J., S.S. Yoo, and D.E. Kim, Nano-scale wear: a review. *Int. J. Precis. Eng. Manuf.*, 2012. **13**(9): p. 1709-18.

116. Feldbauer, G., et al., Adhesion and material transfer between contacting Al and TiN surfaces from first principles. *Phys. Rev. B*, 2015. **91**(16): p. 165413.

117. Vahdat, V., et al., Atomic-scale wear of amorphous hydrogenated carbon during intermittent contact: a combined study using experiment, simulation, and theory. *ACS Nano*, 2014. **8**(7): p. 7027-40.

118. Astala, R. and M.J. Stottt, First-principles study of hydroxyapatite surfaces and water adsorption. *Phys. Rev. B*, 2008. **78**(7): p. 075427.

119. Johnson, K.L., The correlation of indentation experiments. *Journal of the Mechanics and Physics of Solids*, 1970. **18**(2): p. 115-26.

120. Yu, W.P. and J.P. Blanchard, An elastic-plastic indentation model and its solutions. *Journal of Materials Research*, 1996. **11**(9): p. 2358-67.

121. Oliver, W.C. and G.M. Pharr, An improved technique for

determining hardness and elastic modulus using load and displacement sensing indentation experiments. *J. Mater. Res.*, 1992. **7**(6): p. 1564-83.

122. Oliver, W.C. and G.M. Pharr, Measurement of hardness and elastic modulus by instrumented indentation: Advances in understanding and refinements to methodology. *Journal of Materials Research*, 2004. **19**(1): p. 3-20.

123. Bolshakov, A. and G.M. Pharr, Influences of pileup on the measurement of mechanical properties by load and depth sensing indentation techniques. *Journal of Materials Research*, 1998. **13**(4): p. 1049-58.

124. McElhaney, K.W., J.J. Vlassak, and W.D. Nix, Determination of indenter tip geometry and indentation contact area for depth-sensing indentation experiments. *Journal of Materials Research*, 1998. **13**(5): p. 1300-06.

125. Bowden, F.P. and D. Tabor, *The friction and lubrication of solids*. 1950, Oxford: Clarendon Press.

126. Sedriks, A. and T. Mulhearn, Mechanics of cutting and rubbing in simulated abrasive processes. *Wear*, 1963. **6**(6): p. 457-66.

127. Atkins, A.G. and J.H. Liu, Toughness and the transition between cutting and rubbing in abrasive contacts. *Wear*, 2007. **262**(1-2): p. 146-59.

128. Saber-Samandari, S. and K.A. Gross, Micromechanical properties of single crystal hydroxyapatite by nanoindentation. *Acta Biomater.*, 2009. **5**(6): p. 2206-12.

129. Zamiri, A. and S. De, Mechanical properties of hydroxyapatite single crystals from nanoindentation data. *Journal of the Mechanical Behavior of Biomedical Materials*, 2011. **4**(2): p. 146-52.

130. Chiatti, F., M. Corno, and P. Ugliengo, Stability of the dipolar (001) surface of hydroxyapatite. *J. Phys. Chem. C*, 2012. **116**(10): p. 6108-14.

131. Zhu, W.H. and P. Wu, Surface energetics of hydroxyapatite: a DFT study. *Chem. Phys. Lett.*, 2004. **396**(1-3): p. 38-42.

132. Corno, M., et al., Water adsorption on the stoichiometric (001) and (010) surfaces of hydroxyapatite: A periodic B3LYP study. *Langmuir*, 2009. **25**(4): p. 2188-98.

133. Corno, M., et al., Periodic B3LYP study of hydroxyapatite (001) surface modelled by thin layer slabs. *Eur. J. Mineral.*, 2007. **19**(5): p. 757-67.

134. Olszta, M.J., et al., Bone structure and formation: a new perspective. *Mater. Sci. Eng. R-Rep.*, 2007. **58**(3-5): p. 77-116.

135. Ma, Y., et al., Sea urchin tooth design: an "All-Calcite" polycrystalline reinforced fiber composite for grinding rocks. *Adv. Mater.*, 2008. **20**(8): p. 1555-59.

136. Chand, N., U.K. Dwivedi, and S.K. Acharya, Anisotropic abrasive wear behaviour of bamboo (Dentrocalamus strictus). *Wear*, 2007. **262**(9-10): p. 1031-37.

137. Callow, J.A. and M.E. Callow, Trends in the development of environmentally friendly fouling-resistant marine coatings. *Nature Communications*, 2011. **2**: p. 244.

138. Hall-Stoodley, L., J.W. Costerton, and P. Stoodley, Bacterial biofilms: From the natural environment to infectious diseases. *Nat. Rev. Microbiol.*, 2004. **2**(2): p. 95-108.

139. Clare, A.S., Marine natural product antifoulants: Status and potential. *Biofouling*, 1996. **9**(3): p. 211-29.

140. Rosenhahn, A., T. Ederth, and M.E. Pettitt, Advanced nanostructures for the control of biofouling: The fp6 eu integrated project ambio. *Biointerphases*, 2008. **3**(1): p. 1-5.

141. Voulvoulis, N., M.D. Scrimshaw, and J.N. Lester, Comparative environmental assessment of biocides used in antifouling paints. *Chemosphere*, 2002. **47**(7): p. 789-95.

142. Ralston, E. and G. Swain, Bioinspiration-the solution for biofouling control? *Bioinspir. Biomim.*, 2009. **4**(1): p. 015007.

143. Bixler, G.D. and B. Bhushan, Biofouling: lessons from nature. *Philos Trans A Math Phys Eng Sci*, 2012. **370**(1967): p. 2381-417.

144. Cordeiro, A.L. and C. Werner, Enzymes for Antifouling Strategies. *Journal of Adhesion Science and Technology*, 2011. **25**(17): p. 2317-44.

145. Dobretsov, S., H.-U. Dahms, and P.-Y. Qian, Inhibition of biofouling by marine microorganisms and their metabolites. *Biofouling*, 2006. **22**(1): p. 43-54.

146. Feng, D.Q., et al., Low barnacle fouling on leaves of the mangrove plant Sonneratia apetala and possible anti-barnacle defense strategies. *Marine Ecology Progress Series*, 2016. **544**: p. 169-82.

147. Ismail, A.E., et al., Interfacial structure and dynamics of siloxane systems: PDMS-Vapor and PDMS-Water. *Macromolecules*, 2009. **42**(8): p. 3186-94.

148. Efimenko, K., et al., Development and Testing of Hierarchically Wrinkled Coatings for Marine Antifouling. *ACS Appl. Mater. Interfaces*, 2009. **1**(5): p. 1031-40.

149. Banerjee, I., R.C. Pangule, and R.S. Kane, Antifouling Coatings: Recent Developments in the Design of Surfaces That Prevent Fouling by Proteins, Bacteria, and Marine Organisms. *Advanced Materials*, 2011. **23**(6): p. 690-718.

150. Shikuma, N.J., et al., Marine Tubeworm Metamorphosis Induced by Arrays of Bacterial Phage Tail-Like Structures. *Science*, 2014. **343**(6170): p. 529-33.

151. Hadfield, M.G., et al., Biofilm cue for larval settlement in Hydroides elegans (Polychaeta): is contact necessary? *Mar. Biol.*, 2014. **161**(11): p. 2577-87.

152. Decker, J.T., J.T. Sheats, and A.B. Brennan, Engineered Antifouling Microtopographies: Surface Pattern Effects on Cell Distribution. *Langmuir*, 2014. **30**(50): p. 15212-18.

153. Decker, J.T., et al., Engineered Antifouling Microtopographies: An Energetic Model That Predicts Cell Attachment. *Langmuir*, 2013. **29**(42): p. 13023-30.

154. Brzozowska, A.M., et al., Effect of Variations in Micropatterns and Surface Modulus on Marine Fouling of Engineering Polymers. *ACS Appl. Mater. Interfaces*, 2017. **9**(20): p. 17509-17.

155. Chaudhury, M.K., et al., Adhesive contact of cylindrical lens and a flat sheet. *J. Appl. Phys.*, 1996. **80**(1): p. 30-37.

156. Lee, J.H., et al., Dynamic mechanical behavior of multilayer graphene via supersonic projectile penetration. *Science*, 2014. **346**(6213): p. 1092-96.

157. Yoon, K., A. Ostadhossein, and A.C.T. van Duin, Atomistic-scale simulations of the chemomechanical behavior of graphene under nanoprojectile impact. *Carbon*, 2016. **99**: p. 58-64.

158. Zhang, T., X.Y. Li, and H.J. Gao, Defects controlled wrinkling and topological design in graphene. *Journal of the Mechanics and Physics of Solids*,

2014. **67**: p. 2-13.

159. Yin, H.Q., et al., Griffith Criterion for Brittle Fracture in Graphene. *Nano Lett.*, 2015. **15**(3): p. 1918-24.

160. Jia, Y.F. and F.Z. Xuan, Anisotropic wear behavior of human enamel at the rod level in terms of nanoscratching. *Wear*, 2012. **290**: p. 124-32.